Features of attosecond transient-absorption spectra
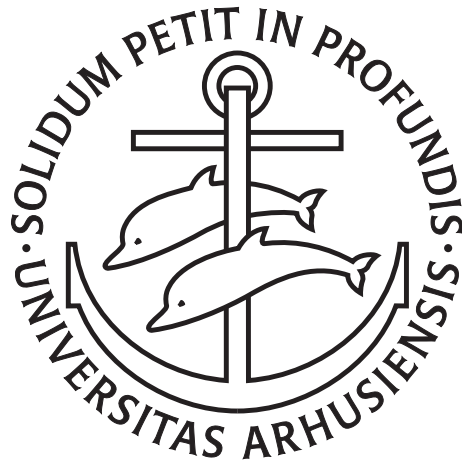
Jørgen Johansen Rørstad

PhD thesis
November 2018

Supervisor: Lars Bojer Madsen

Department of Physics and Astronomy
Aarhus University

"It's the writing that teaches you."
— Isaac Asimov

English summary

Electrons, with their tiny masses, zip around in atomic and molecular systems at breakneck speeds. In order to follow this movement on the natural timescale of the electrons, extremely short pulses of light must be employed. The capability of producing these pulses was realized at the turn of the millennium, marking the birth of attosecond science. Conceptualizing the briefness of an attosecond can be challenging, as the attosecond is to a millisecond what a hair's breadth is to the distance between the Earth and the Sun. The extreme temporal precision that can be accessed with these pulses has truly opened up the realm of electronic processes for exploration.

In this PhD thesis, we apply the method of attosecond transient-absorption spectroscopy (ATAS) in the study of electrons in atoms and molecules. In this modern technique, two pulses—coordinated with attosecond accuracy—propagate toward the system of interest, and the subsequent response of the system is recorded. The results are displayed in rich spectrograms, where each feature is a signature of a dynamical electronic process having occurred in the system; the interpretation of these features constitutes the main focus of this thesis. By implementing standard numerical methods in conjunction with models based on an assumption of adiabaticity, we gain a new perspective on some of the most ubiquitous features in ATAS. As we extend our study to polar molecules—largely unexplored in the context of ATAS—we see both a new feature in the spectrum, and well-known features appearing in unconventional settings.

Dansk resumé (Danish summary)

Med deres små masser farer elektroner rundt i atomare og molekylære systemer med halsbrækkende hastigheder. For at kunne følge denne bevægelse på elektronens naturlige tidsskala må man anvende ekstremt korte lyspulser. Det blev muligt at realisere disse pulse i starten af det nye årtusinde, og dette markerede fødslen af *attosecond science*. At konceptualisere hvor kort et attosekund er, kan være udfordrende, da et attosekund er for et millisekund som en hårsbredde er for distancen mellem solen og jorden. Den ekstreme tidspræcision man får adgang til med disse pulser, har virkelig åbnet op for udforskningen af elektroniske processer.

I denne PhD-afhandling benytter vi metoden *attosecond transient-absorption spectroscopy* (ATAS) til studiet af elektroner i atomer og molekyler. Denne moderne teknik benytter to pulser—koordineret med attosekunds nøjagtighed—som sendes ind mod systemet af interesse, og den efterfølgende respons bliver detekteret. Resultaterne bliver udforsket i indholdsrige spektrogrammer, hvor hvert element er en signatur af en dynamisk process, der er foregået i systemet. Tolkningen af disse elementer udgør hovedfokuset i denne afhandling. Ved at implementere gængse numeriske metoder sammen med modeller baseret på en antagelse om adiabatisitet, får vi et nyt perspektiv på nogle af de mest velkendte elementer i ATAS. Når vi udvider studiet til polære molekyler, som er stort set uudforskede indenfor ATAS, ser vi både et nyt element og tidligere studerede elementer i ukonventionelle sammenhænge.

Preface

This dissertation encompasses the work I have done during my PhD studies at the Department of Physics and Astronomy, Aarhus University, Denmark, from December 2015 to November 2018. These studies were carried out under the supervision of Professor Lars Bojer Madsen.

Notation

Atomic units ($m_e = e = \hbar = 4\pi\epsilon_0 = 1$) are used throughout the thesis, unless stated otherwise. log refers to the natural logarithm. In certain location, where appropriate, explicit indication of dependencies in expressions is omitted, for the sake of brevity.

Acknowledgments

I have been fortunate to meet a lot of wonderful people during my three years of PhD studies, and I owe a debt of gratitude to all those who have helped me—directly or indirectly—in the making of this thesis.

   The first person I would like to acknowledge is my brilliant supervisor Lars Bojer Madsen. Through the last three years Lars has been unfailingly supportive, accessible, and helpful, and I have always felt that he has had my best interest at heart. I would also like to thank all the members of the Bojer group, past and present, for interesting group meetings and discussions—both the technical, and the less serious ones. Thanks to Grete Flarup for always being ready to help me out, and for spreading joy to the 6th floor. And thanks to Jens E. Bækhøj, Lun Yue, and Nikolaj S. W. Ravn for the excellent collaborations we have had.

   Many people have contributed to my happiness here in Denmark, through discussions, games, parties, or just by generally being great people. These people include Jens B. and Jens Svensmark (the Jenses), Felix

Motzoi, Eliška Greplova, Kamanasish Debnath, Izhak Cohen, Albert B. Cases, Philip D. Blocher, Kenneth C. K. Hansen, Nikolaj, Jinglei Zhang, Alexander H. Kiilerich, Pier P. Poier, and Constant A. Schouder—thanks to all of you!

The support of my friends and family has been invaluable to me. Thanks to my parents (and stepparents!) for their neverending support and encouragement, for being interested in my work, and for helping me to get to where I am today. And thanks, of course, to my friends from Ålesund and HG; I can always count on you for a great time whenever we meet.

To conclude the most important section of my thesis (in terms of readership), I would like to thank my most important supporter, Katérina Verteletsky. Thank you so much for all the loving support you have given me over these last years.

List of Publications

[1]   J. J. Rørstad, J. E. Bækhøj, and L. B. Madsen, Analytic modeling
      of structures in attosecond transient-absorption spectra, Physical
      Review A **96**, 013430 (2017).

[2]   J. J. Rørstad, N. S. W. Ravn, L. Yue, and L. B. Madsen, Attosecond
      transient-absorption spectroscopy of polar molecules, Phys. Rev. A
      98, 053401 (2018).

In addition to the work contained within this thesis, I have co-authored
the following paper

[3]   M. Chovancova, H. Agueny, J. J. Rørstad, and J. P. Hansen, Classical
      and quantum-mechanical scaling of ionization from excited hydrogen
      atoms in single-cycle thz pulses, Phys. Rev. A **96**, 023423 (2017).

List of Abbreviations

as	attosecond
ATAS	Attosecond transient-absorption specotroscopy
BO	Born-Oppenheimer
CEP	Carrier-envelope phase
FFT	Fast Fourier transform
fs	femtosecond
FWHM	Full width at half maximum
HHG	High harmonic generation
IR	Infrared
LIS	Light-induced structure
NIR	Near infrared
PEC	Potential energy curve
TDM	Transition dipole moment
TDSE	Time-dependent Schrödinger equation
TEO	Time evolution operator
UV	Ultraviolet
XUV	Extreme ultraviolet

Contents

Introduction

L ight has fascinated humans for millennia, with perhaps the oldest recorded studies on the subject found in the writings of the luminaries of ancient Greece. In more recent centuries, great strides were made in our knowledge of light by contemporaries Isaac Newton and Christiaan Huygens, who held seemingly contradictory views on the nature of light— Newton claiming light consisted of particles and Huygens subscribing to a wave theory of light. At the turn of the 18th century Thomas Young entered the fray, and ostensibly settled the matter convincingly with his double-slit experiment, where the wave nature of light was demonstrated by the wave interference phenomenon.

Another major breakthrough followed in the 1860s, with the publication of a seminal set of equations by James Clerk Maxwell; the equations that lie at the heart of classical electromagnetism. As the 20th century was approaching, in one of the first formal descriptions of light-matter interaction, Johann Jakob Balmer devised a formula which predicted the wavelengths of light emitted from a hydrogen gas. Why only light corresponding to a discrete set of wavelengths is emitted from such a gas was not fully understood until the concerted efforts of a number brilliant physicists had lead to the quantum theory, in the 1920s. Major developments that paved the way for this theory include the resolution of the ultraviolet catastrophe by Max Planck, by assuming that light could only be emitted or absorbed in discrete packets (now known as photons); the photoelectric effect, discovered by Albert Einstein; the Bohr model of the atom, proposed by Niels Bohr; and the development of the formalism of quantum mechanics, by Heisenberg, Born, Schrödinger, Dirac, and others.

1.1   Ultrafast Processes

One field which owes its current existence to our understanding and command of light, is the study of ultrafast processes. In the observation of any process, the time resolution with which we can resolve the process is fundamentally limited by our ability to generate light pulses of lengths on a similar scale to the process itself. In the macroscopic world, the failure of meeting this condition is experienced by the photographer whose picture is blurred, as her exposure time is slow compared to the movement of her subject. This limitation has spurred the development of light-sources capable of producing ever-shorter pulses of light, with the goal of understanding ultrafast processes such as molecular- and electronic motion, which occur on timescales ranging from picoseconds (10^{-12} s) down to attoseconds (10^{-18} s). With today's technology these regimes of time are accessible, owing to an awesome development in light generation that can be traced back to the revolutionary invention of the laser in the 1960s [4, 5].

Attosecond science is the field at the frontier of ultrafast dynamics [6–9]. It is in large part dedicated to the study of electron dynamics, which can take place over extremely short periods of time due to the small mass of the electron. The birth of this relatively young field was marked by the generation of the first attosecond-scale pulse in 2001 [10], which was made possible by the maturing of high harmonic generation (HHG) [11–14] technology. In HHG a nonlinear process takes place, in which intense light of a certain frequency is fixed upon a target (e.g. a gas), whereupon the target emits light with frequencies at multiples (harmonics) of the incoming laser pulse—typically reaching frequencies in the extreme ultraviolet (XUV) or soft X-ray [15] regimes. In the last 17 years the groundbreaking advances made in attosecond science include attosecond streaking [16, 17], used to characterize attosecond pulses; real time observation and control of electron dynamics [18–21]; timing of photoemission processes in atoms and molecules [22–26], which were shown to be—contrary to previous assumptions—non-instantaneous; and the real time observation of the emergence of a Fano resonance in He [27].

One of the more recent techniques to emerge within attosecond science is attosecond transient-absorption spectroscopy (ATAS) [28–30], which is based on a pump-probe technique. In the typical pump-probe type setup, two pulses are incident upon a target; one is designated the pump pulse and initiates dynamics in the target, whereas the other is designated the probe pulse and its interaction with the target is recorded and yields information about the dynamics of the system. In this scenario, time-resolution is

obtained by varying the delayed incidence of one pulse with respect to the other—this delay, denoted τ, can be precisely controlled, and a scan over a range of delays can provide the basis for a comprehensive account of the time-dependent dynamics of the interaction.

1.2   Attosecond Transient-absorption Spectroscopy

ATAS is a wholly optical method, in which an attosecond pulse acts in conjunction with a femtosecond pulse to induce dynamics in a target system. The resulting time-dependent dipole moment of the system gives rise to a generated field, which in turn interferes with the original incoming attosecond pulse. The interference signal which arises due to this interplay carries the imprint of the ultrafast dynamics of the system, and is recorded by a detector in a time-integrated manner. Repeating the process for a number of time delays in a given range, enables the creation of rich spectrograms, from which we can infer valuable insights into the electronic and nuclear dynamics of the system. In Chapters 3 and 4, a number of such spectra will form a considerable part of the basis for our analysis and discussion.

What we refer to in the previous paragraph as an attosecond pulse, is in ATAS typically an ultraviolet (UV) pulse with a broad spectral bandwidth, which is capable of populating a number of excited states via single-photon absorption. What we refer to as a femtosecond pulse typically has frequencies in the infrared (IR) regime, and thus consists of a narrower band of low-frequency components. The conceptual picture we often use for the IR pulse is as a dressing field, which mixes adjacent atomic or molecular states that have already been excited in the system by the UV pulse. Typically, the two pulses pulses can be more precisely categorized as lying in the XUV and near infrared (NIR) subregions of the spectrum, and we will use the more specific designations where appropriate. Unlike in the general pump-probe setup described previously, there is in ATAS some ambiguity concerning the pump- and probe labels, which we bypass by exclusively using UV/XUV or IR/NIR labels for the pulses.

Studies which involve ATAS have contributed significantly to our understanding of processes related to electronic and nuclear dynamics in systems of varying complexity [31, 32]. In atoms, ATAS has been applied in the investigation of autoionization processes and Rydberg states in Ar [33, 34] and He [35–37]; in the generation and control of wave packets in He [38, 39] and Kr [40]; in the observation of strong field driven dynamics

and ionization in Xe [41, 42]; and in the investigation of Auger processes in highly excited states of C [43] and Kr [44]. In addition to these, some studies rely on model systems consisting of a subset of atomic states from a given system, e.g., Rb [45–47].

In the last few years, molecules have also been scrutinized both experimentally and theoretically, with an emphasis on homonuclear diatomic molecules such as H_2 [48], N_2 [49, 50], and O_2 [51]; with studies conducted on the effect of nuclear dynamics on bound electrons [52], autoionizing effects [53], and on the effect of the presence of a conical intersection between the energy surfaces in diatomic system [54]. ATAS has also been applied to polyatomic molecules [55], semiconductors [56–59], dielectrics [60, 61], and to dense gases [62, 63], where in the latter propagation effects become a significant factor.

The spectrograms briefly described in the start of the present section are characterized by an assortment of spectral signatures which originate in physical electronic processes. We refer to these signatures here and throughout the thesis simply as *features*. These features comprise the basic information on which all analysis in ATAS is based, and they are heavily dependent on the nature and properties of the system and incoming laser fields. Some of the more ubiquitous features include oscillating fringes arising due to dressing of states by the IR pulse [64–66]; hyperbolic sidebands enveloping the absorption lines of the spectra—associated with perturbed free-induction decay [67–69]; light-induced structures (LIS) capturing the presence of virtual states acting as intermediaries in multiphoton processes, where population is transferred to dark states from the ground state [70, 71]; and modification, splitting, or distortion of absorption line shapes [72–75], e.g. categorized as Stark shifts [76, 77] or Autler-Townes splitting [78–80]. The varied and burgeoning collection of systems and processes analyzed with ATAS underscores the general versatility of the method.

These features, and their underlying processes, are the main focus of this thesis. One of the motivating factors behind this was the recognition that a more unambiguous description of the features could be a useful addition to the existing literature. In Ref. [1], we took a new approach in the study of the features, which was based on a three-level atomic system expressed in adiabatic basis states. From this ansatz we derived analytical expressions describing several of the most common features, which were used to understand both the origins of the features and exactly how the components of each feature depended on the properties of the system and the ultrafast pulses. In Ref. [2], we extended our studies

to polar molecules—a class of molecules largely unexplored by ATAS. The calculated spectra of these molecules exhibit both a new, previously unobserved, ladder structure, and LISs appearing at energies forbidden in nonpolar systems; we showed how these findings were directly related to the presence of a nonzero permanent dipole in the system.

1.3 Thesis Outline

In Chapter 2 an introduction to the theory behind ATAS is given. This is followed by descriptions of the main components that are required to generate an ATAS spectrum; in particular, the time-dependent dipole moment of atomic and molecular systems. The Hamiltonian of the respective systems are then defined, followed by a review of the numerical methods required to solve the time-dependent equations. We also consider the complex absorbing potential, which protects against unphysical reflections at the boundary of the simulation box, and show how to use imaginary time propagation to obtain the ground state of the system. Finally, we discuss the window function, which is used to manually induce dephasing into the system.

In Chapter 3 we describe our work on atomic ATAS, and we start by introducing some of the main features in the ATAS spectrogram, to prepare the reader for the deeper analysis that follows. We use the numerical methods of Chapter 2 to compare calculations where we have used two different numbers of basis states of He, in order to validate the use of three basis states in the adiabatic model that follows. This model is then constructed, and we proceed to build upon it in order to derive fully analytical expressions corresponding to each of the three features: the LISs, SBs and fringes. We then compare the spectra, with a focus on each individual feature, as they are calculated by each of our methods. At the end of Chapter 3, we consider some other common features of the ATAS spectrogram, which were not integrated into the adiabatic model.

Chapter 4 contains our work on molecular ATAS, and starts with comparing molecular to atomic ATAS, by outlining the new factors that must be taken into account, such as nuclear motion and orientation with respect to the field. Next, we present the system and field properties, where we have used the polar molecule LiF to exemplify the theory. We numerically calculate ATAS spectra with the methods of Chapter 2, compare spectra with and without the permanent dipoles that are inherent in LiF, and discuss the findings. We then go on to supplement the numerical calcu-

lations with an adiabatic model, which is based on similar assumptions to the model in Chapter 3, and derive expressions that allow us to better understand the features. Finally, we consider how the arrangement of the molecules with respect to the fields affect the ATAS spectra.

In Chapter 5 we present the main conclusions of the thesis, and suggest possible directions for further research.

Theory and Methodology

In this chapter we present the theory on which subsequent chapters are based, along with various methods we have employed. The material presented in the chapter is not, however, exhaustive with respect to what could be classified as theory, as we reserve parts of that for Chapters 3 and 4. Presenting certain parts of the theory in the specific context in which it is applied will be meaningful in terms of conveying our understanding of the relevant ATAS features.

The chapter starts in Section 2.1 with an introduction to the response function, which is the central equation in theoretical ATAS, expressing the spectroscopic response of a system subject to ultrafast pulses, as described in Chapter 1. A crucial component in the response function is the time-dependent dipole moment, which is the subject of Section 2.2, with subsections dedicated individually to atoms and molecules. In Section 2.3 we characterize the time-dependent Hamiltonians governing the atomic and molecular systems, and describe the electric fields used throughout the thesis. Then, in Section 2.4, we introduce several numerical concepts, including the implementation of the time propagation scheme, which involves the time-evolution operator and the split step method; the complex absorbing potential, which alleviates potential problems stemming from finite simulation boxes; and backwards imaginary time propagation, used to determine ground states. The chapter concludes with the presentation of the window function, in Section 2.5.

2.1   The Response Function

The essence of ATAS lies in the description of the interaction between an extremely short pulse, and the field created by the induced dipole moment in the target system upon which this pulse is incident. The present section gives a summarized version of the derivation of an expression referred to as the response function, which serves as a time-integrated representation of this interaction. Rigorous and comprehensive derivations of the response function can be found in Ref. [81], or in the thesis [82]. Given the availability of sources on this topic, we content ourselves with relaying the most important aspects of the derivation.

In Chapter 1 we described the typical ATAS setup, where two pulses are incident upon a target system. The arrival of these two pulses is separated by a delay τ with respect to the two temporal pulse centers. As a matter of convention, in the following—and throughout the thesis—the IR pulse center will be fixed at time $t_{c,\text{IR}} = 0$, with the UV pulse centered at time $t_{c,\text{UV}} = \tau$.

We also note that all fields employed in this thesis can be characterized as being of low- to moderate intensity, ranging from the order of $I \sim 10^7$ W/cm^2 to $I \sim 10^{12}$ W/cm^2. Despite this characterization, the intensities put the fields well within the scope of the typical semiclassical approximation, in which the fields are treated classically, and only the target system is given a full quantum mechanical treatment.

As described in Chapter 1, the signal acquired by the detector corresponds to a combination of the frequency-resolved fields—one from the incoming UV pulse and one generated by the system. We make the approximation that the fields are plane waves which propagate in the x-direction. Evaluating the signal, $S(\omega, \tau)$, in the asymptotic limit where x tends to infinity, we can express it as [83]

$$
\begin{aligned}
S(\omega, \tau) &= \left| \tilde{\boldsymbol{F}}_{\text{in}}(\omega, \tau) + \tilde{\boldsymbol{F}}_{\text{gen}}(\omega, \tau) \right|^2 \\
&= |\tilde{\boldsymbol{F}}_{\text{in}}(\omega, \tau)|^2 + 2\,\text{Re}\left[\tilde{\boldsymbol{F}}_{\text{in}}^*(\omega, \tau)\tilde{\boldsymbol{F}}_{\text{gen}}(\omega, \tau) \right] + |\tilde{\boldsymbol{F}}_{\text{gen}}(\omega, \tau)|^2,
\end{aligned}
\tag{2.1}
$$

where $\tilde{\boldsymbol{F}}_{\text{in}}(\omega, \tau)$ and $\tilde{\boldsymbol{F}}_{\text{gen}}(\omega, \tau)$ are the frequency-resolved incoming and generated fields, respectively. As mentioned, the τ variable represents the temporal delay between the centers of the incident UV and IR pulses, and ω is the angular frequency. The tilde denotes Fourier transformed quantities. In this thesis, we adhere to the following notation and convention for

Fourier transforms

$$\mathcal{F}\left[f(t)\right](\omega) = \tilde{f}(\omega) = \frac{1}{\sqrt{2\pi}} \int\limits_{-\infty}^{\infty} dt\, f(t) e^{-i\omega t}. \tag{2.2}$$

Equation (2.1) can be simplified by recognizing that the $|\tilde{\boldsymbol{F}}_{\text{in}}(\omega, \tau)|^2$ term cannot yield any information about the dynamics of the system, and noting that the $|\tilde{\boldsymbol{F}}_{\text{gen}}(\omega, \tau)|^2$ term will be comparatively small due to the relatively low amplitude of the generated field; we neglect both, and are left with

$$S(\omega, \tau) = 2\,\text{Re}\left[\tilde{\boldsymbol{F}}_{\text{in}}^*(\omega, \tau)\tilde{\boldsymbol{F}}_{\text{gen}}(\omega, \tau)\right], \tag{2.3}$$

which we refer to as the response function. Here and throughout the thesis we will assume that $\tilde{\boldsymbol{F}}_{\text{in}}$ is linearly polarized in the z-direction, and thus only the z-components of $\tilde{\boldsymbol{F}}_{\text{in}}$ and $\tilde{\boldsymbol{F}}_{\text{gen}}$ need to be considered. Consequently, we drop vector notation in the following, and scalar quantities should be understood to refer to z-components.

The next step is to relate $\tilde{F}_{\text{gen}}$ to an observable of the system, namely the dipole moment. We proceed by assuming that an approximate solution can be obtained by considering only a single atom or molecule—depending on the situation—as our target. This single-system assumptions allows us to circumvent the formidable computational task of accounting for propagation effects in a target medium [84], and has been shown to be valid for sufficiently dilute gases [70]. In an atomic or molecular gas the expectation value of the dipole moment, $\langle d(t, \tau) \rangle$, is related to the polarization of the system, $P(t, \tau)$, through

$$P(t, \tau) = \rho \langle d(t, \tau) \rangle, \tag{2.4}$$

where ρ is the density of the gas, which we here arbitrarily set equal to unity. Note that in this thesis we use a lowercase d when referring to the dipole moment of an atomic system, and an uppercase D to refer to the dipole moment of a molecular system. In general though, the theory presented in this chapter applies to both systems, unless the context indicates otherwise. Assuming that the target is a thin sheet of gas, which complies with our single-system assumption, and in light of the other assumptions made, the Maxwell wave equation for the generated field reads

$$\left(\frac{\partial^2}{\partial x^2} - \frac{1}{c^2}\frac{\partial^2}{\partial t^2}\right) F_{\text{gen}}(x, t, \tau) = \frac{4\pi}{c^2}\frac{\partial^2}{\partial t^2}P(t, \tau)\delta(x), \tag{2.5}$$

with $c \approx 137$ the speed of light and $\delta(x)$ the Dirac delta function. From Eqs. (2.5) and (2.4) we can obtain an expression for the generated field F_{gen} (see Refs. [81] and [82]), which in the frequency domain can be expressed as

$$\tilde{F}_{\text{gen}}(\omega, \tau) = -i\frac{2\pi\omega\rho}{c}\tilde{d}(\omega, \tau),\qquad(2.6)$$

with [see Eq. (2.2)] $\tilde{d}(\omega, \tau) = \frac{1}{2\pi}\int_{-\infty}^{\infty} dt \, \langle d(t, \tau)\rangle \exp\left(-i\omega t\right)$. Inserting Eq. (2.6) into Eq. (2.3), we get the following expression for the response function

$$S(\omega, \tau) = \frac{4\pi\omega\rho}{c}\text{Im}\left[\tilde{F}_{\text{in}}^{*}(\omega, \tau)\tilde{d}(\omega, \tau)\right].\qquad(2.7)$$

Through the derivation of Eq. (2.7) we have effectively reduced the task of determining the ATA spectrum of a given system under the influence of an UV and IR pulse to the calculation of the expectation value of the dipole moment of the system. The spectra obtained through this response function constitute a central part of this thesis, and will be exhibited, interpreted, and discussed in detail in the following chapters. We note that in Eq. (2.7), positive values correspond to emission of light by the target system, whereas negative values correspond to absorption of light. Several equivalent forms of the response function exist in the literature, and for an overview of these we refer the reader to Refs. [52] and [82].

2.2 The Time-dependent Dipole Moment

Having shown, in the previous section, that the task of obtaining the response function [Eq. (2.7)] for a given system amounts to obtaining the frequency-resolved dipole moment of the system, we now consider this observable in more detail. In the present thesis we consider both atoms [see Chapter 3] and diatomic molecules of various kinds [see Chapter 4]. There are considerable differences in terms of complexity between theoretical derivations for the two classes of systems, with the molecular case being significantly more complex. Here, as in the following chapters, we take the practical approach of treating the two systems separately.

2.2.1 Atomic Dipole Moment

The expectation value of the time-dependent dipole moment for an atom is

$$\langle d\rangle \equiv \langle\Psi(t)|\hat{d}|\Psi(t)\rangle = \int\limits_{-\infty}^{\infty} d\mathbf{r}\, \Psi^{*}(t, \mathbf{r})\, \hat{d}\, \Psi(t, \mathbf{r})\qquad(2.8)$$

where $\Psi(t, \mathbf{r})$ is the full atomic wave function, and $\hat{d}$ is the dipole moment operator—with operators denoted by hats—defined by [85]

$$\hat{d} = -\sum_{j=1}^{N_e} \boldsymbol{r}_j, \tag{2.9}$$

with $\boldsymbol{r}_j$ referring to the coordinates of the j'th electron with respect to the nucleus, and with N_e electrons in the atom. In Eq. (2.8) we have used $\langle \cdot | \cdot \rangle$ to denote integration over $\mathbf{r}$.

We express the quantum state of the system, $\Psi(t, \mathbf{r})$, as a linear combination of the stationary eigenstates $\psi_k(\mathbf{r})$ ($k = 1, 2, \ldots, N$) of the unperturbed atomic Hamiltonian H_0:

$$\Psi(t, \mathbf{r}) = \sum_{k=1}^{N} c_k(t) \psi_k(\mathbf{r}) e^{-iE_k t} \tag{2.10}$$

with c_k the complex amplitudes, and E_k the energies, of the eigenstates. To put it in other terms, the eigenstates $\psi_k(\boldsymbol{r})$ and -energies E_k satisfy the time-independent Schrödinger equation,

$$H_0 \psi_k(\boldsymbol{r}) = E_k \psi_k(\boldsymbol{r}). \tag{2.11}$$

For the purposes of this thesis, it is sufficient in Eq. (2.10) to include only a finite number, N, of field-free bound states [65]. This is valid since the atomic dynamics we consider in the following are rooted in the lowest-lying states of the relevant atoms, which are located within a range of energies relatively far from the continuum.

In light of Eqs. (2.8) and (2.10), we can express the atomic time-dependent dipole moment as

$$\langle d \rangle = \sum_{k,l=1}^{N} c_k^*(t) c_l(t) e^{-i(E_l - E_k)t} d_{kl}, \tag{2.12}$$

where we have introduced the transition dipole moment (TDM)

$$d_{kl} = \langle \psi_k | \hat{d} | \psi_l \rangle. \tag{2.13}$$

2.2.2 Molecular Dipole Moment

In the atomic system, we have chosen as the origin the center of the nucleus—in molecules the choice is less obvious. One of the simplifying

aspects of the molecular systems we consider, is that they are exclusively diatomic. Starting out in the laboratory frame of reference, the total dipole moment operator for diatomic molecules can be written as

$$\hat{D} = Z_1\mathbf{R}_1 + Z_2\mathbf{R}_2 - \sum_{j=1}^{N_e} \mathbf{r}'_j \tag{2.14}$$

where $\mathbf{R}_1$ and $\mathbf{R}_2$ are the coordinates of the two nuclei, with corresponding nuclear charges Z_1 and Z_2; $\mathbf{r}'_j$ is the coordinate of the j'th electron, and N_e the number of electrons in the molecule.

In this thesis we are interested in the internal degrees of freedom of our system, and in such cases using relative coordinates can simplify calculations. We introduce the coordinates

$$\mathbf{R} = \mathbf{R}_2 - \mathbf{R}_1 \tag{2.15}$$

$$\mathbf{r}_{\mathrm{CM}} = \frac{M_1\mathbf{R}_1 + M_2\mathbf{R}_2 + \sum_{j=1}^{N_e} \mathbf{r}'_j}{M_1 + M_2 + N_e} \tag{2.16}$$

$$\mathbf{r}_j = \mathbf{r}'_j - \frac{M_1\mathbf{R}_1 + M_2\mathbf{R}_2}{M_1 + M_2}, \tag{2.17}$$

where M_1 and M_2 are the nuclei masses, $\mathbf{r}_{\mathrm{CM}}$ the center of mass coordinates of the system, and $\mathbf{r}_j$ the electron coordinates relative to the center of mass of the nuclei.

With the coordinates from Eqs. (2.15)-(2.17), it can be shown that the dipole moment can be expressed as

$$\hat{D} = (Z_1 + Z_2 - N_e)\mathbf{r}_{\mathrm{CM}} + \alpha\mathbf{R} - \beta\sum_{j=1}^{N_e} \mathbf{r}_j, \tag{2.18}$$

where we have defined the constants

$$\alpha = \frac{M_1 Z_2 - M_2 Z_1}{M_1 + M_2}, \tag{2.19}$$

$$\beta = 1 + \frac{Z_1 + Z_2 - N_e}{M_1 + M_2}. \tag{2.20}$$

Another aspect of the specific molecular systems we consider here that can lead to a simplification of calculations, is that their total charge is zero—i.e. we don't consider ionic systems such as H_2^+. In Eqs. (2.18) and (2.20) the $Z_1 + Z_2 - N_e$ factors can be recognized as the total charge, and

thus set to zero. Finally then, the appropriate molecular dipole moment operator for our purposes is

$$\hat{D} = \alpha\mathbf{R} - \sum_{j=1}^{N_e} \mathbf{r}_j. \tag{2.21}$$

In order to establish an expression for the expectation value of the dipole moment, our next step is to obtain an expression for the quantum state of the diatomic molecule. Similarly to the atomic case, we wish to use a set of basis states in which we can expand the full wave function [85]. In the following we consider only the vibrational motion of the nuclei, neglecting the much slower rotational motion. If we define an electronic Hamiltonian as

$$H_e = T_e + V, \tag{2.22}$$

where T_e is the kinetic energy operator for the electrons, and V represents the total potential energy of the system due to the coulomb interactions, then electronic basis states, $\phi_k(\mathbf{r}_1, \mathbf{r}_2, \ldots; R)$, can be obtained as the eigenfunctions of H_e at fixed R:

$$H_e\phi_k(\mathbf{r}_1, \mathbf{r}_2, \ldots; R) = E_k(R)\phi_k(\mathbf{r}_1, \mathbf{r}_2, \ldots; R), \tag{2.23}$$

where the energies $E_k(R)$ depend only on the magnitude of the internuclear separation, R. The neglecting of the nuclear kinetic energy operator constitutes part of the Born–Oppenheimer (BO) approximation, and the adiabatic curves traced out by $E_k(R)$ ($k = 1, 2, \ldots, N$) as R is varied incrementally in small steps, will be referred to as either BO curves or simply as potential energy curves (PECs). We again consider only a finite manifold of N electronic states, following the same reasoning as in the atomic case (see Section 2.2.1).

The molecular wave function can now be expressed in terms the basis functions ϕ_k, as

$$\Phi(t, \mathbf{r}_1, \mathbf{r}_2, \ldots; R) = \sum_{k=1}^{N} \chi_k(t, R)\phi_k(\mathbf{r}_1, \mathbf{r}_2, \ldots; R) \tag{2.24}$$

where we have introduced the nuclear wave functions $\chi_k(t, R)$ as expansions coefficients. We can now express the expectation value for the dipole moment as

$$\langle D \rangle_{\boldsymbol{r},R} \equiv \langle \Phi | \hat{D} | \Phi \rangle_{\boldsymbol{r},R} = \sum_{k,l=1}^{N} \int_0^\infty dR \, \chi_k^*(t, R) \, D_{kl} \, \chi_l(t, R) \tag{2.25}$$

where

$$D_{kl} = \langle \phi_k | \hat{D} | \phi_l \rangle_{\boldsymbol{r},R} \tag{2.26}$$

are the molecular transition dipole moments. We note that in Eq. (2.25), in contrast with the atomic case, integration over the continuum of internuclear distances, R, is necessary as well—we denote this explicitly by the subscript $\langle \cdot | \cdot \rangle_{\boldsymbol{r},R}$ where relevant.

2.3   Hamiltonians

In order to calculate the time-dependent atomic and molecular dipole moments, given in Eqs. (2.12) and (2.25), we require the time-dependent expansion coefficients c_k and χ_k, in addition to the transition dipole moments d_{kl} and D_{kl}. The transition dipole moments can be obtained through quantum chemistry packages such as DALTON [86] or Gaussian [87], or from sources in published literature. In this thesis we rely on the latter, with the specific sources given at the relevant locations in Chapters 3 and 4. What remains then, is to calculate the expansion coefficients, which is the subject of this section. We start by considering the field interaction, after which we (as in Section 2.2) treat the atomic and molecular cases separately.

2.3.1   Field Interaction

All fields used in this thesis are derived through the relation $F(t) = -\frac{\partial}{\partial t} A(t)$, where we have chosen to work in the Coulomb gauge and with no sources present. We also apply the dipole approximation, in which the field is constant over the spatial extent of the system under consideration; the approximation is valid as long as the wavelengths of the incoming pulses are large relative to the size of the system. A field $F(t)$ with no subscript label should be understood to represent the sum of the fields.

The vector potential used in this thesis is

$$A(t) = A_0 \exp\left[-\frac{(t - t_c)^2}{T^2/4} \right] \cos\left[\omega(t - t_c) + \varphi \right], \tag{2.27}$$

where we have $A_0 = F_0/\omega$, with F_0 the field amplitude, related to the intensity through $I = |F_0|^2$; t_c is the temporal center of the pulse; φ is the carrier-envelope phase (CEP); and $T = N_c T_c = N_c \frac{2\pi}{\omega}$ is the period of the pulse, with T_c the period of a single cycle and N_c the number of cycles. $T_{\text{FWHM}} = \sqrt{\log 2}\, T$ connects the full width at half maximum (FWHM)

with the period. Relevant field parameters are provided on a case-by-case basis throughout the thesis.

In the following sections we will define the Hamiltonians governing the dynamics of the two kinds of systems—atomic and molecular—under consideration. The field interactions enters into the Hamiltonian through the following term

$$V_L(t) = -F(t)\hat{d} = F(t)\sum_{j=1}^{N_e}\mathbf{r}_j, \tag{2.28}$$

for the atomic case, and the term

$$V_L(t) = -F(t)\hat{D} = -F(t)\left(\alpha\mathbf{R} - \sum_{j=1}^{N_e}\mathbf{r}_j\right), \tag{2.29}$$

for the molecular case. The Eqs. (2.28) and (2.29) can be obtained through a unitary transformation of the Hamiltonian—introduced in the ensuing sections—to the so-called length gauge, which leaves the time-independent terms unaltered.

For background details on gauge fixing, various unitary transformation of the Hamiltonian, and the dipole approximation beyond the cursory description offered in this section, we direct the reader to Refs. [82, 88–92].

2.3.2 The Time-dependent Atomic Hamiltonian

The full Hamiltonian we are working with for the atomic system can be expressed as

$$\begin{aligned} H_a(t) &= H_0 + H'(t) \\ &= H_0 - F(t)\hat{d} \end{aligned} \tag{2.30}$$

where H_0 is the time-independent part for which we defined eigenstates ψ_k, with corresponding energies E_k, in Section 2.2.1. After inserting the wave function from Eq. (2.10) into the time-dependent Schrödinger equation (TDSE),

$$i\frac{\partial}{\partial t}\Psi(t, \boldsymbol{r}) = H\Psi(t, \boldsymbol{r}), \tag{2.31}$$

with the Hamiltonian of Eq. (2.30), we can obtain

$$i\sum_{k=1}^{N}\dot{c}_k(t)\psi_k(\mathbf{r})e^{-iE_kt} = \sum_{k=1}^{N}c_k(t)H'(t)\psi_k(\mathbf{r})e^{-iE_kt}, \tag{2.32}$$

where the dot notation implies differentiation with respect to time. By exploiting the orthogonality of the eigenstates, we can obtain a set of coupled equations by taking the inner product of Eq. (2.32) with ψ_l, for $l = 1, 2, \ldots, N$. The l'th expansion coefficient can then be obtained by solving

$$i\dot{c}_l(t) = -F(t) \sum_{k=1}^{N} c_k(t) d_{kl} e^{i(E_l - E_k)t}. \tag{2.33}$$

2.3.3 The Time-dependent Molecular Hamiltonian

The terms entering into the molecular Hamiltonian include the following: the term corresponding to the interaction between the field and the molecule [see Eq. (2.29)]; the terms corresponding to the coulomb interaction between the charged particles of the system and the electronic kinetic energy, which added together constitute the electronic Hamiltonian [see Eq. (2.22)]; and finally the term corresponding to the kinetic energy of the nuclei, T_{nuc}. If we neglect a small term known as the mass polarization term, and separate out the center of mass motion, the molecular Hamiltonian reads

$$H_m(t) = H_e + T_{\text{nuc}} + V_L(t). \tag{2.34}$$

In the relative coordinates defined in Eqs. (2.15)-(2.17), the nuclear kinetic energy term is

$$T_{\text{nuc}} = -\frac{1}{2\mu} \frac{\partial^2}{\partial R^2}. \tag{2.35}$$

where we have defined the reduced mass $\mu = M_1 M_2 / (M_1 + M2)$.

To obtain the time-dependent nuclear wave functions χ_k, we insert the molecular wave function as expressed in Eq. (2.24) into the TDSE, with Hamiltonian (2.34), and by projecting onto χ_l ($l = 1, 2, \ldots, N$)—similarly to the atomic case in the previous section—we obtain a set of coupled equations. The equation for the l'th nuclear wave function is

$$
\begin{aligned}
i\dot{\chi}_l(R, t) = {}& \left(E_l(R) - \frac{1}{2\mu} \frac{\partial^2}{\partial R^2} \right) \chi_l(R, t) - \sum_{k=1}^{N} D_{kl} F(t) \chi_k(R, t) \\
& - \frac{1}{2\mu} \sum_{k=1}^{N} \left(2 \left\langle \phi_l \left| \frac{\partial \phi_k}{\partial R} \right. \right\rangle \frac{\partial}{\partial R} + \left\langle \phi_l \left| \frac{\partial^2 \phi_k}{\partial R^2} \right. \right\rangle \right) \chi_k(R, t),
\end{aligned} \tag{2.36}
$$

where the latter two terms, which contain derivatives of the electronic states ϕ_k with respect to R, are known as non-adiabatic terms. In a molecular system, the non-adiabatic terms can often be neglected, but are

important to include when considering dynamics of nuclear wave packets close to the avoided crossings between BO curves. In this thesis these terms are neglected entirely, but their significance and the possibilities of exploring systems where they cannot be neglected are briefly discussed in Chapters 4 and 5.

2.4 Numerical Implementation

Solving the set of coupled equations for the expansion coefficients of the atomic wave functions [see Eq. (2.33)] is—for the systems considered in this thesis—not very computationally demanding, and is readily accomplished using standard Runge–Kutta methods. The differential equations for the nuclear wave functions [see Eq. (2.36)], on the other hand, can be challenging to solve numerically. In this section we describe the methods that we employ to manage this task.

2.4.1 Time-evolution Operator

We start by introducing the time-evolution operator (TEO) [93], $\mathcal{U}(t_2, t_1)$, whose defining characteristic can be understood by demonstrating its action on the time-dependent state $\Psi(t_0)$:

$$\Psi(t) = \mathcal{U}(t, t_0)\Psi(t_0), \tag{2.37}$$

where we see that the action of the TEO on the state is to propagate it from its initial state at time t_0 to its state at time t.

For the valid application of the TEO in propagation of the state of our system, we require that it fulfills several physically significant conditions. In addition to satisfying the TDSE, we require the TEO to be unitary,

$$\mathcal{U}^\dagger(t_2, t_1)\mathcal{U}(t_2, t_1) = 1 \tag{2.38}$$

which ensures the conservation of probability. Furthermore, we require continuity,

$$\lim_{t_2 \to t_1} \mathcal{U}(t_2, t_1) = 1, \tag{2.39}$$

and equivalence between the time evolution from t_1 to t_3, and the same time evolution via an intermediate time t_2, i.e., t_1 to t_2 to t_3:

$$\mathcal{U}(t_3, t_1) = \mathcal{U}(t_3, t_2)\mathcal{U}(t_2, t_1). \tag{2.40}$$

For small time steps Δt, an approximate form of the TEO is

$$\mathcal{U}(t + \Delta t, t) \approx e^{-iH(t)\Delta t}. \tag{2.41}$$

In light of Eq. (2.40), the validity of the approximation can be guaranteed by dividing the time propagation from some initial time t_0 to a final time t_f into as many intermediate steps as necessary in order to fulfill the criterion of having a sufficiently small step size. For the calculations within this thesis, we have found that a value of $\Delta t = 0.02$ is adequate to ensure converged results.

2.4.2 The Split Operator Method

Calculating the matrix exponential in Eq. (2.41) is often computationally expensive. The Split Operator method [94–96] offers a way to lower this cost by shifting the main computational expense from calculating matrix exponentials to performing a series of fast Fourier transforms (FFTs) [97].

   If the time $t_f - t_0$ represents the full propagation time we want to realize, we can divide it into N intervals of size Δt, so that we have $t_f - t_0 = N\Delta t$. Assuming for descriptive purposes that we are considering a wave packet moving in one dimension and interacting with an electric field, the TEO can then be expressed as

$$\mathcal{U}(t_f, t_0) = e^{-iH(x,p,t_f-\Delta t)\Delta t} e^{-iH(x,p,t_f-2\Delta t)\Delta t} \cdots \\ \times\, e^{-iH(x,p,t_0+\Delta t)\Delta t} e^{-iH(x,p,t_0)\Delta t}, \tag{2.42}$$

where the corresponding Hamiltonian can be separated into terms each depending either on the position x and momentum p

$$H(x, p, t) = g(x, t) + h(p, t). \tag{2.43}$$

Take any one of the exponential factors from from Eq. (2.42), representing a propagation over time Δt, e.g. from t_0 to $t_0 + \Delta$; this factor be written as

$$\begin{aligned} e^{-iH(x,p,t_0)\Delta t} &= e^{-i[g(x,t_0)+h(p,t_0)]\Delta t} \\ &= e^{-ih(p,t_0)\frac{\Delta t}{2}} e^{-ig(x,t_0)\Delta t} e^{-ih(p,t_0)\frac{\Delta t}{2}} + \mathcal{O}(\Delta t^3), \tag{2.44} \\ &\approx e^{-ih(p,t_0)\frac{\Delta t}{2}} e^{-ig(x,t_0)\Delta t} e^{-ih(p,t_0)\frac{\Delta t}{2}}, \end{aligned}$$

where the error term $\mathcal{O}(\Delta t^3)$ stems from the fact that $g(x, t_0)$ and $h(p, t_0)$ are non-commuting. The Split Operator method makes use of the fact

that each of the factors in Eq. (2.44) are—or can be made to be—diagonal on either a spatial grid or a momentum grid. In between the application of each exponential then, a FFT is performed to transform the state to the representation in which the operator will be diagonal—thus avoiding the relatively taxing evaluation of matrix exponentials.

For general details about how to implement the method, such as how to define the grids relative to each other, efficient representation of the wave function for the FFT, numerical representation of operators, and the scaling of various computational costs we direct the reader to Refs. [82, 98]. For a specific implementation of Split Step operator for the system governed by the Hamiltonian of Eq. (2.34), we recommend Ref. [91].

2.4.3   Complex Absorbing Potential

Numerical representation of physical systems typically entail discretization and truncation of continuous components, by using finite basis sets, discrete grids, and finite box sizes. A pertinent example of the latter is the internuclear distance, R, between diatomic molecules considered in this thesis, which must be truncated at some maximum distance R_{max}. Unphysical effects, such as reflection, can arise as wave packets collide with the box boundary at R_{max}. To counteract this effect, we introduce a complex absorbing potential (CAP) [99], which comes into effect as the wave packet propagates into the region between some internuclear distance R_{CAP}, and the boundary R_{max}. The role of the CAP is to extinguish the components of the wave function that are approaching R_{max}. Thus, any components within the range of the CAP, i.e., at $R > R_{\mathrm{CAP}}$, must be negligible in terms of their impact on the observables we are considering—in our case this can be achieved by selecting a sufficiently large R_{CAP}.

The CAP is introduced as an addition to the Hamiltonian $H(t)$, so that

$$H(t) \rightarrow H(t) - iV_{\mathrm{CAP}}, \tag{2.45}$$

where we have chosen the specific form

$$V_{\mathrm{CAP}} = \begin{cases} \eta(R - R_{\mathrm{cap}})^p, & \text{if } R > R_{\mathrm{CAP}}, \\ 0, & \text{otherwise.} \end{cases} \tag{2.46}$$

The values for the parameters in Eq. (2.46) used in this thesis are $\eta = 0.001$, $R_{\mathrm{CAP}} = 20$, and $p = 2$. The efficiency of the CAP is for our purposes not very sensitive with respect to these parameters, and so their precise value

is of limited importance. Note that there exist several forms of the CAP, see for example Ref. [91].

The action of the CAP can be seen by making the substitution of Eq. (2.45) in the equation for the form of the TEO, Eq. (2.41), upon which we obtain

$$
\begin{aligned}
\mathcal{U}(t + \Delta t), t) &\approx e^{-i[H(t) - iV_{\mathrm{CAP}}]\Delta t} \\
&= e^{-iH(t)\Delta t} e^{-V_{\mathrm{CAP}}\Delta t},
\end{aligned}
\tag{2.47}
$$

where the effect of the factor $e^{-V_{\mathrm{CAP}}\Delta t}$ clearly is suppressive where V_{CAP} is nonzero, i.e., for $R_{\mathrm{CAP}} > R$.

2.4.4   Imaginary Time Propagation

Common to all systems considered in this thesis is that they start out in the ground state; obtaining the ground state wave function, however, is not a trivial task. A numerical method known as imaginary time propagation can be used for this purpose. Given a field-free time-independent Hamiltonian H_0, and the substitution $\Delta t \to -i\Delta t'$, the TEO can be written as [see Eq. (2.41)]

$$
\mathcal{U}(-i\Delta t') = e^{-H_0 \Delta t'},
\tag{2.48}
$$

where H_0 corresponds to a system which can be expressed in terms of the eigenstates of H_0, and where the ground state per definition has the lowest energy. The TEO of Eq. (2.48) suppresses the components of the wave function, but at rate depending on the energy of the component, with lower energy resulting in a slower rate of decay.

The ground state then, can be obtained by initiating the system in some state with population in each of the eigenstates, applying the propagator from Eq. (2.48), renormalizing the wave function, and repeating until the system has converged, i.e., when only one state has any appreciable population remaining in it.

2.5   The Window Function

In certain situations we require the time-dependent dipole moment to dephase over a given time period, an effect which is not necessarily automatically included in our theoretical model. In this thesis we will encounter two ways in which this can occur. The first is related to experimental conditions, where colliding particles and spontaneous emission can lead to dephasing, and the finite resolution of the detector can broaden emission or

absorption lines. The second occurs as we apply a certain approximation to our model, introducing weaknesses that we must artificially mitigate—we elaborate on this in Chapter 4.

To include dephasing in our model, we introduce the window function, $W(t - t_w)$, [32, 52] which is a function that smoothly tends to zero over a period of time, starting at some time t_w. It is defined as

$$W(t - t_w) = \begin{cases} 1 & (t < t_w) \\ \exp\left[-\dfrac{(t - t_w)^2}{T_w^2/4}\right] & (t_w \leq t), \end{cases} \tag{2.49}$$

where the FWHM of the Gaussian corresponding to the exponential function is connected to T_w via the relation $T_{\text{FWHM}} = \sqrt{\log 2}\, T_w$. The window function can mimic the effects of experimental circumstances, or alleviate effects of certain approximations, by multiplying it with the calculated time-dependent dipole moment.

In this thesis we are focusing on certain features arising in ATAS. It is important to point out that the effect of the window function on these features is well understood, and the values of the parameters in Eq. (2.49) are carefully chosen so as to minimize its effect on them—something we discuss in more detail in the following chapters. In the most common application of the window function, the parts of the time-dependent dipole moment that are directly responsible for the ATAS features we consider are mostly unaffected, and only subsequent oscillations—which otherwise in principle could continue ad infinitum—are dampened, affecting mainly the width of the ordinary absorption lines.

Atoms

This chapter is devoted to the exploration of the features appearing in the atomic ATAS spectrum. The contents of this chapter overlap with that of Ref. [1], of which I am the first author. My contribution to this research was major in all areas, i.e., deriving of expressions, numerical calculations and interpretation of data, construction of figures, and preparation of manuscript. Note that several of the figures in this chapter are reproduced directly—with permissions—from Ref. [1].

The chapter starts out in Section 3.1 with an introduction to the system with which we will exemplify our theory, the parameters of the XUV and IR fields, and a brief description of the features that are the main focus of the rest of the chapter. Then, in Section 3.2, we consider the results obtained through the numerical calculations of Chapter 2, and verify that a three-level model will yield correct results in a specific energy range, by comparing it with a 20-level model. In Section 3.3 we construct the adiabatic three-level model, which assumes that the system adapts instantly to the influence of the IR pulse. Then, in Section 3.4 we derive analytical expressions which describe the three features we are interested in, based on the adiabatic model. In Section 3.5, we compare the ATAS spectra calculated by each of the models—numerical, adiabatic model, analytical—and consider the three features individually. Finally, in Section 3.6, we briefly introduce two other important features appearing in ATAS spectra.

3.1 Atomic ATAS Spectrograms

In this section we give a brief introduction to the main spectroscopic features considered in this chapter, as a primer for the following in-depth analytical work. Figure 3.1 shows an ATAS spectrogram of helium, where the relevant features are highlighted. These features are some of the most recognizable in ATAS, and can appear both in atomic and in molecular spectra; they do not, however, constitute a complete list of ATAS features. The model we use to examine these features is based on an adiabatic approximation, and therefore it cannot represent certain features stemming from resonant processes, such as Autler-Townes splitting [73, 78–80, 100] and electromagnetically-induced transparency (EIT) [101, 102]. We give a relatively concise description of Autler-Townes splitting at the end of the chapter, in Section 3.6.

3.1.1 Field Parameters and System

The features can only be understood in the context of the atomic or molecular system in which they arise, and the parameters of the incoming fields. In most of this chapter we use three levels of the helium atom as our model system. These states are the ground state $|1s^2\rangle$, the dark state $|1s2s\rangle$, and the bright state $|1s2p\rangle$, where the bright state—as opposed to the dark state—is accessible via a dipole allowed transition from the ground state. The transition dipole moments [see Eq. (2.13)] are: $d_{12} = 0.729$ between the ground state and the bright state, and $d_{23} = -5.051$ between the bright state and dark state. The energies of the system are $E_1 = E(1s^2) \equiv 0$, $E_2 = (1s2p) = 21.23$ eV, and $E_3 = E(1s2s) = 20.62$ eV. The parameters for the field are: $\lambda_{\text{IR}} = 3200$ nm (corresponding to $\omega_{\text{IR}} = 0.39$ eV), $\lambda_{\text{XUV}} = 50$ nm (corresponding to $\omega_{\text{XUV}} = 24.80$ eV), $I_{\text{IR}} = 6 \times 10^{10}$ W/cm^2, $I_{\text{XUV}} = 5 \times 10^7$ W/cm^2, $T_{\text{IR}} = 32.02$ fs ($N_{c,\text{IR}} = 3$), and $T_{\text{XUV}} = 330$ as ($N_{c,\text{XUV}} = 2$). The CEP φ is set to zero for both fields throughout the chapter. The atom density is arbitrarily set to $\rho = 1$ [see Eq. (2.7)]. The FWHM of the Gaussian corresponding to our window function (see Section 2.5) is chosen to be large enough that the features of interest are unaffected, which amounts to $T_{\text{FWHM}}/2 = 100$ fs. In this chapter the starting point of the window function coincides with the incidence of the XUV pulse, i.e., $t_w = \tau$.

The energies of the levels of the system, and the parameters of the XUV and IR fields, have important implications for the dynamics of the interaction. The low intensities enable the use of various approximations
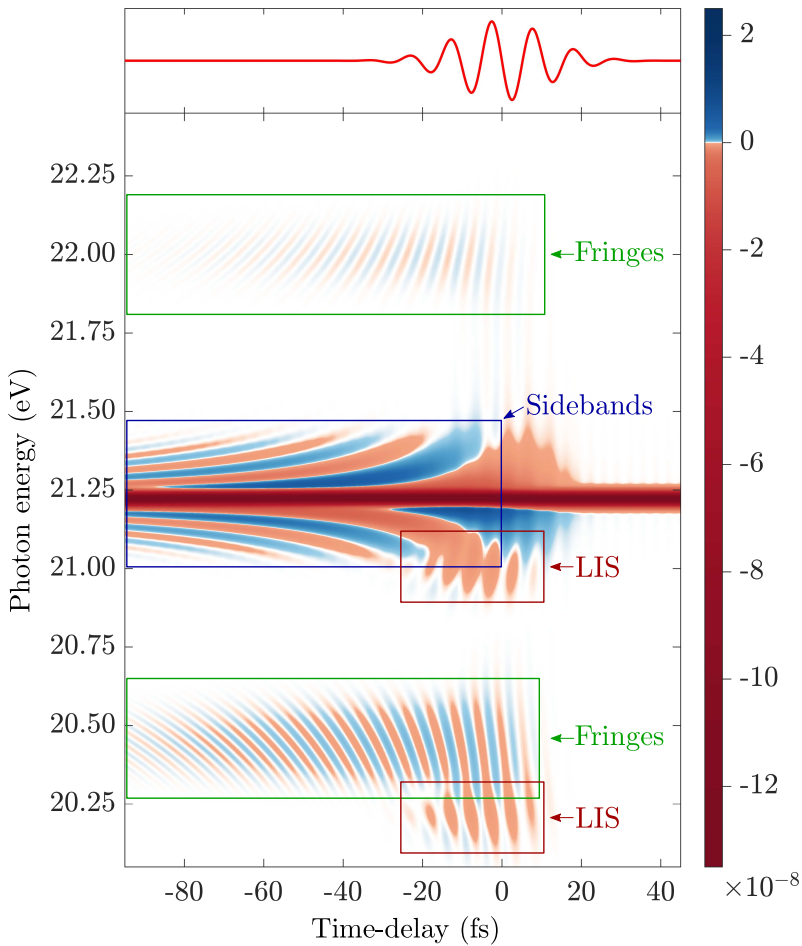
Figure 3.1: Attosecond transient absorption spectrum $\tilde{S}(\omega, \tau)$ [Eq. (2.7)], as calculated by the model developed in Section 3.3, exemplified by He. The three relevant features are accentuated by colored boxes: oscillating fringes (green) centered around energies $E(1s2p) + 2\omega_{\mathrm{IR}} = 22.01$ eV and $E(1s2p) - 2\omega_{\mathrm{IR}} = 20.45$ eV; light-induced structures (red) centered around energies $E(1s2s) + \omega_{\mathrm{IR}} = 21.01$ eV and $E(1s2s) - \omega_{\mathrm{IR}} = 20.23$ eV; and hyperbolic sidebands (blue) centered around main absorption line at energy $E(1s2p) = 21.22$ eV. Relevant parameters are given in Section 3.1.1. An illustration of the infrared pulse, centered at $\tau = 0$ fs, is shown in the top panel. The color scale to the right displays the signal strength in arbitrary units. Reproduced with permissions from Phys. Rev. A **96**, 013430 (2017) [1]. Copyright 2017 American Physical Society.

in Sections 3.3 and 3.4. Furthermore, given the relatively large energy gap between the ground state and excited states, only the XUV pulse can populate the excited states via single-photon absorption. The IR photon energy is significantly lower, and thus it can only populate the excited states via multiphoton absorption, which is completely suppressed for the present intensity. The conceptual role of the IR pulse here then, is to dress the excited states—which will be discussed in detail in the following sections.

3.1.2 Main Features

Oscillating Fringes

Oscillating fringes, which we refer to simply as fringes in the following, can be seen enclosed by green boxes in Fig. 3.1—centered at energies $E_{F+} = E(1s2p) + 2\omega_{IR} = 22.01$ eV and $E_{F-} = E(1s2p) - 2\omega_{IR} = 20.45$ eV. These fringes have been attributed to various form of interference [66, 103].

Hyperbolic Sidebands

In the blue box, we see hyperbolic sidebands (SBs) along the absorption line corresponding to the $|1s2p\rangle$ state, at $E(1s2p) = 21.23$ eV. The SBs are commonly considered a signature of perturbed free-induction decay [64, 67–69, 104], appearing as a consequence of the decay of the time-dependent dipole being interrupted with the incidence of the IR pulse.

Light-induced Structures

Finally, we have the light-induced structures (LISs) in red boxes, centered at energies $E_{LIS+} = E(1s2s) + \omega_{IR} = 21.01$ eV and $E_{LIS-} = E(1s2s) - \omega_{IR} = 20.23$ eV. The LISs are considered a signal of an intermediate state arising due to a two-photon in which one XUV photon is absorbed and one IR photon is either emitted or absorbed, resulting in a population transfer from the ground state to the dark state at $E(1s2s) = 20.62$ eV [70, 71].

3.2 Numerical Calculations

In this section we use the numerical methods of Section 2.3.2 to obtain helium ATAS spectra. The purpose of the numerical calculations is to provide a reference to which we can compare the results of our subsequent model calculations, and analytical expressions. The model we use to derive

these expressions is based on a three-level system, and by comparing numerically calculated spectra based on a set of either $N = 3$ or $N = 20$ basis states, we can show that there are no relevant differences between the two in the relevant energy range.

The numerical results in this section are obtained by: solving the set of coupled equations for the atomic expansions coefficients [Eq. (2.33)], using couplings and energies corresponding to the N lowest state of the helium atom, acquired from Ref. [105]; calculating the time-dependent dipole moment using these coefficients [Eq. (2.12)]; Fourier transforming according to Eq. (2.2) to obtain the frequency resolved dipole moment; inserting into Eq. (2.7) to get the response function; and repeating the process for a range of delays τ until the desired spectrogram is developed.

3.2.1 Basis Set Size Comparison

In order to serve as a valid reference for the model calculations, we require the numerical calculations to be based on the same three levels as the model. We do not include more than three levels in the model for two reasons: all the features we are interested in can be generated in a system with three levels, and including more levels drastically increase the complexity of the model. In the numerical calculations, on the other hand, including more levels is relatively straightforward. This enables us to test the validity of calculations based on three levels by directly comparing them with calculations based on a greater number of levels.

Figure 3.2 consists of calculations with $N = 20$ basis states, in panel (a), and $N = 3$ basis states, in panel (b). In order to claim that the calculations based on three levels are valid, we must have agreement between the two spectra in the energy range extending from ~ 20 eV to ~ 22.4 eV—a range encompassing all features corresponding to the $|1s2s\rangle$ and $|1s2p\rangle$ states. The only visible discrepancy lies at approximately 22.2 eV in panel (a), where the fringes corresponding to the $|1s2p\rangle$ state at energy $E(1s2p)+2\omega_{\mathrm{IR}}$ are obscured by the fringes corresponding to the $|1s3p\rangle$ state at energy $E(1s3p)-2\omega_{\mathrm{IR}}$. As the $|1s3p\rangle$ state is excluded from the calculations [panel (b)], its corresponding fringes vanish, and the fringes related to the $|1s2p\rangle$ state are uncovered. Consequently, the features of interest are accurately represented in the numerical three-level calculation, and the numerical spectra can be used as references for the analytical model in the ensuing section. We note, however, that in an experiment it would not be possible to achieve an unobscured view of the fringes at energy ~ 22.01 eV, as the $|1s3p\rangle$ state cannot be neglected. Other measures—such as increasing the
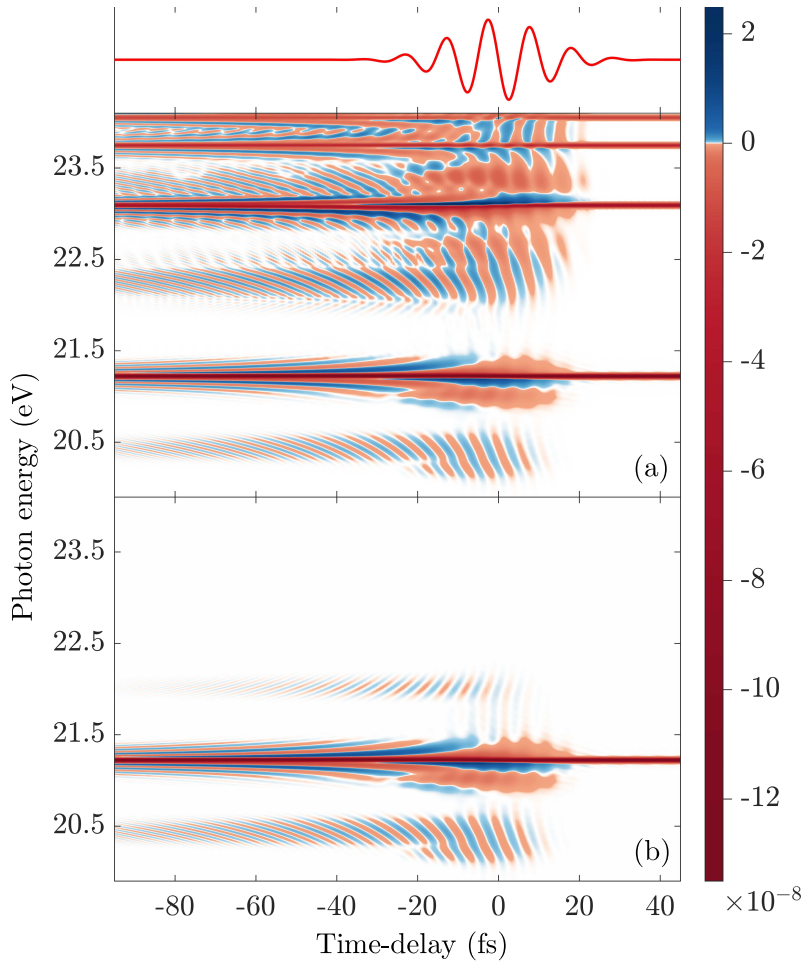
Figure 3.2: Attosecond transient absorption spectrum $\tilde{S}(\omega, \tau)$ [Eq. (2.7)], as calculated by the numerical methods developed in Chapter 2. The results obtained using a basis set consisting of the $N = 20$ lowest states of He are shown in panel (a), with the results obtained using a basis set of the $N = 3$ lowest states shown in panel (b). The three lowest levels consist of the ground state, fixed at energy $E(1s^2) = 0$, a bright state at energy $E(1s2p) = 21.23$ eV, and a dark state at energy $E(1s2s) = 20.62$ eV. Relevant parameters are given in Section 3.1.1. An illustration of the infrared pulse, centered at $\tau = 0$ fs, is shown in the top panel. The color scale to the right displays the signal strength in arbitrary units. Reproduced with permissions from Phys. Rev. A **96**, 013430 (2017) [1]. Copyright 2017 American Physical Society.

wavelength of the IR pulse—could instead be taken, in order to isolate the relevant fringes.

3.3 Adiabatic Three-level Model

We now turn to developing the adiabatic three-level model, which forms the basis of the derivation of analytical expression for each of the features described in Section 3.1.2. One of the reasons for developing a model from which we can obtain spectra—when we also have the capability of calculating these spectra numerically—lies in the insights that can be gathered directly from the expressions of the model. With an analytical expression in hand, it is possible to explicitly link characteristics of the system, and parameters of the fields used, to the features appearing in the spectrograms.

In Chapter 2 we identified the dipole moment of the system as a crucial component in ATAS. The process of obtaining an expression for the dipole moment in the adiabatic model starts with expressing our three-level system in terms of adiabatic states. We then apply perturbation theory with respect to the brief XUV pulse, followed by a number of approximations, all made with the purpose of acquiring an expression for the time-dependent dipole moment which can be subjected to an analytic Fourier transform. As we shall see, the dipole moment can be split into several terms, each representing one of the features of interest. The fully analytical response functions for the individual features are finally obtained through Eq. (2.7).

3.3.1 Adiabatic System

As mentioned, a fundamental assumption of the model is that the system responds adiabatically with respect to the relatively slowly varying IR field. Under such an assumption, it is often desirable to express our system in terms of adiabatic states $|\psi_{ka}(t)\rangle$, defined by

$$\left[H_0 - F_{\text{IR}}(t)\hat{d}\right]|\psi_{ka}(t)\rangle = E_{ka}(t)|\psi_{ka}(t)\rangle. \tag{3.1}$$

The implication of Eq. (3.1) is that the adiabatic states $|\psi_{ka}(t)\rangle$ are the instantaneous eigenstates of the Hamiltonian—excluding the XUV field—of our system, with the eigenenergies $E_{ka}(t)$. The wave function of our system

can then be expressed as

$$|\Psi_a(t)\rangle = a_1(t)|\psi_1\rangle + a_2(t)|\psi_{2a}\rangle\, e^{-i\int_\tau^t dt'\, E_{2a}(t')} + a_3(t)|\psi_{3a}\rangle\, e^{-i\int_\tau^t dt'\, E_{3a}(t')},$$

(3.2)

where $a_k(t)$ are the complex amplitudes of the adiabatic states, and $\exp\left(-i\int_\tau^t dt'\, E_{ka}\right)$ are the phase-factors for the time-dependent adiabatic energies. In Eq. (3.2) we have made the assumption that the ground state—unlike the excited states—does not change appreciably under the influence of the IR pulse. The excited states lie relatively adjacent to each other, as compared with the ground state, and this proximity is of crucial importance to the modification of the states, which will be shown in the following. Note that in Eq. (3.1) we have suppressed certain dependencies in the notation for brevity, and we will do so in the ensuing sections when appropriate.

3.3.2 Adiabatic States and -Energies

The full Hamiltonian of the system, can be represented in matrix form in a basis of the field free states $|\psi_k\rangle$ ($k = 1, 2, 3$), as

$$\underline{\underline{H}} = \begin{bmatrix} 0 & -d_{12}F_{\mathrm{XUV}}(t,\tau) & 0 \\ -d_{12}F_{\mathrm{XUV}}(t,\tau) & E_2 & -d_{23}F_{\mathrm{IR}}(t) \\ 0 & -d_{23}F_{\mathrm{IR}}(t) & E_3 \end{bmatrix},$$

(3.3)

which shows the coupling between the ground state $|\psi_1\rangle$ and the bright state $|\psi_2\rangle$, due to the XUV pulse; and the coupling between the bright state $|\psi_2\rangle$ and the dark state $|\psi_3\rangle$ due to the IR pulse.

We can reduce the matrix in Eq. (3.3), by noting that after the incidence of the XUV pulse at time $t = \tau$, we effectively have a two-level system consisting of the two excited states (see Section 3.1.1). The reduced Hamiltonian is then

$$\underline{\underline{H_2}} = \begin{bmatrix} E_2 & -d_{23}F_{\mathrm{IR}}(t) \\ -d_{23}F_{\mathrm{IR}}(t) & E_3 \end{bmatrix},$$

(3.4)

from which the states $|\psi_{ka}(t)\rangle$ and the associated energies $E_{ka}(t)$ can be obtained, as the instantaneous eigenstates and -energies. The energies are

$$E_{2a}(t) \approx E_2 + \frac{d_{23}^2 F_{\mathrm{IR}}^2(t)}{E_2 - E_3},$$

(3.5)

$$E_{3a}(t) \approx E_3 - \frac{d_{23}^2 F_{\mathrm{IR}}^2(t)}{E_2 - E_3},$$

(3.6)

where we have carried out a Taylor expansion in the IR field about $F_{\text{IR}}(t) = 0$, and neglected terms of order $\mathcal{O}(F_{\text{IR}}^3)$, due to the low intensity of the IR field. The normalized eigenstates of the matrix in Eq. (3.4) are

$$
\begin{aligned}
|\psi_{2a}(t)\rangle = {} & \frac{d_{23}F_{\text{IR}}(t)}{\sqrt{d_{23}^2 F_{\text{IR}}^2(t) + [E_{2a}(t) - E_2]^2}} |\psi_2\rangle \\
& + \frac{E_{2a}(t) - E_2}{\sqrt{d_{23}^2 F_{\text{IR}}^2(t) + [E_{2a}(t) - E_2]^2}} |\psi_3\rangle,
\end{aligned}
\tag{3.7}
$$

and

$$
\begin{aligned}
|\psi_{3a}(t)\rangle = {} & \frac{E_{3a}(t) - E_3}{\sqrt{d_{23}^2 F_{\text{IR}}^2(t) + [E_{3a}(t) - E_3]^2}} |\psi_2\rangle \\
& + \frac{d_{23}F_{\text{IR}}(t)}{\sqrt{d_{23}^2 F_{\text{IR}}^2(t) + [E_{3a}(t) - E_3]^2}} |\psi_3\rangle,
\end{aligned}
\tag{3.8}
$$

which reduce to their corresponding field-free states in the limit where $F_{\text{IR}}(t) \to 0$.

3.3.3 Complex Adiabatic Amplitudes

To obtain the coefficients $a_2(t)$ and $a_3(t)$, we start by inserting $|\Psi_a\rangle$ from Eq. (3.2), with the full Hamiltonian

$$
H = H_0 - F_{\text{IR}}(t)\hat{d} - F_{\text{XUV}}(t, \tau)\hat{d},
\tag{3.9}
$$

into the TDSE. By applying the relation of Eq. (3.1), and projecting onto each of the adiabatic states $|\psi_{2a}\rangle$ and $|\psi_{3a}\rangle$, we obtain expressions for $\dot{a}_2(t)$ and $\dot{a}_3(t)$—with dot notation implying differentiation with respect to time. Note that we have $\langle\psi_{ja}|\psi_{ka}\rangle = \delta_{kj}$, which follows from the matrix of Eq. (3.4) being real, symmetric, and with distinct eigenvalues. The next step is to treat the system perturbatively with respect to the XUV pulse. An unperturbed system would be expected to remain in the ground state indefinitely, and so we designate the zeroth order coefficients as $a_1^{(0)}(t) = 1$, $a_2^{(0)}(t) = 0$, and $a_3^{(0)}(t) = 0$ (superscripts denoting the order of approximation). To obtain the first order coefficients, we insert the zeroth order coefficients into the equations for $\dot{a}_2(t)$ and $\dot{a}_3(t)$ [106], which yields

$$
\dot{a}_2^{(1)}(t) = iF_{\text{XUV}}(t, \tau)\langle\psi_{2a}|\hat{d}|\psi_1\rangle\, e^{i\int_\tau^t dt' E_{2a}(t')},
\tag{3.10}
$$

$$
\dot{a}_3^{(1)}(t) = iF_{\text{XUV}}(t, \tau)\langle\psi_{3a}|\hat{d}|\psi_1\rangle\, e^{i\int_\tau^t dt' E_{3a}(t')}.
\tag{3.11}
$$

The change in the ground state coefficient is negligible relative to its magnitude throughout the interaction, and so we set $a_1(t) = 1$.

3.3.4 Dipole Moment

Finally, we calculate the dipole moment $\langle d \rangle_a = \langle \Psi_a | \hat{d} | \Psi_a \rangle$. Given the low intensity of the XUV pulse, the magnitude of the complex amplitudes [Eqs. (3.10) and (3.11)] will remain small at all times t—allowing us to reasonably neglect any second order product of the amplitudes in the expression for the dipole moment. To leading other in these coefficients then, we have

$$
\begin{aligned}
\langle d \rangle_a = {} & a_2 \langle \psi_1 | \hat{d} | \psi_{2a} \rangle \, e^{-i \int_\tau^t dt' E_{2a}(t')} + a_3 \langle \psi_1 | \hat{d} | \psi_{3a} \rangle \, e^{-i \int_\tau^t dt' E_{3a}(t')} \\
& + a_2^* \langle \psi_1 | \hat{d} | \psi_{2a} \rangle \, e^{i \int_\tau^t dt' E_{2a}(t')} + a_3^* \langle \psi_1 | \hat{d} | \psi_{3a} \rangle \, e^{i \int_\tau^t dt' E_{3a}(t')}.
\end{aligned}
\tag{3.12}
$$

Equation (3.12) can be simplified further by recalling that it will be subject to a Fourier transform, in which exponentials $e^{\pm ibt}$ (with b a real positive number) corresponds to either a shift to positive frequencies (+) or a shift to negative frequencies (-), depending on the sign in the exponent [see Eq. (A.4)]. Only the positive frequencies are relevant, and so we neglect the terms corresponding to shifts to negative frequencies, which yields

$$
\langle d \rangle_a = a_2^* \langle \psi_1 | \hat{d} | \psi_{2a} \rangle \, e^{i \int_\tau^t dt' E_{2a}(t')} + a_3^* \langle \psi_1 | \hat{d} | \psi_{3a} \rangle \, e^{i \int_\tau^t dt' E_{3a}(t')}.
\tag{3.13}
$$

What remains is to determine the explicit forms of the coupling terms $\langle \psi_1 | \hat{d} | \psi_{2a} \rangle$ and $\langle \psi_1 | \hat{d} | \psi_{3a} \rangle$. Given that we have $d_{13} = 0$, we need only consider the first term in each of the Equations (3.7) and (3.8). As before, we perform a Taylor expansion of these terms in the IR field about $F_{\mathrm{IR}}(t) = 0$ and neglect terms of third order or higher, resulting in the following expressions

$$
\langle \psi_1 | \hat{d} | \psi_{2a} \rangle = d_{12} \left[1 - \frac{d_{23}^2 F_{\mathrm{IR}}^2(t)}{2(E_2 - E_3)^2} \right],
\tag{3.14}
$$

$$
\langle \psi_1 | \hat{d} | \psi_{3a} \rangle = -\frac{d_{12} d_{23} F_{\mathrm{IR}}(t)}{E_2 - E_3}.
\tag{3.15}
$$

At this point we have the complete model for the adiabatic three-level system. Equations (3.10) and (3.11) are solved numerically [note that $\langle \psi_1 | \hat{d} | \psi_{ka} \rangle = \langle \psi_{ka} | \hat{d} | \psi_1 \rangle$ $(k = 2, 3)$], and inserted into Eq. (3.13) to obtain the time-dependent dipole moment of the system, which must be multiplied

by the window function [see Section 2.49] to account for dephasing. The Fourier transforms of $F_{\mathrm{XUV}}(t, \tau)$ and the product $W(t - \tau) \langle d \rangle_a$ are then carried out numerically, and the response function $S(\omega, \tau)$ is obtained through Eq. (2.7). We refer to this as the full adiabatic model when comparing spectra in Section 3.5.

3.4 Closed Analytical Forms

With the adiabatic model of the previous section as the foundation, we now proceed with the derivation of analytical expressions representing each of the features described in Section 3.1.2. A common assumption in interactions with ultrashort pulses is that they can approximated by a constant times the Dirac delta function [32, 40, 72, 107]. We carry out this replacement for the XUV pulse, so that

$$F_{\mathrm{XUV}}(t, \tau) \to \gamma \delta(t - \tau), \tag{3.16}$$

where the constant γ is determined by comparison with the maximum intensity of the $|1s2p\rangle$ absorption line in a spectra from numerical calculations. For the present parameters, we have $\gamma = 1.61 \times 10^{-4}$. With the substitution from Eq. (3.16), solving Eqs. (3.10) and (3.11) is trivial, and we get

$$a_2^{(1)}(t) = \int_{\tau_-}^{t} dt' \dot{a}_2^{(1)}(t') = i\gamma\theta(t - \tau)d_{12}\left[1 - \frac{d_{23}^2 F_{\mathrm{IR}}^2(\tau)}{2(E_2 - E_3)^2}\right], \tag{3.17}$$

$$a_3^{(1)}(t) = \int_{\tau_-}^{t} dt' \dot{a}_3^{(1)}(t') = -i\gamma\theta(t - \tau)\frac{d_{12}d_{23}F_{\mathrm{IR}}(\tau)}{E_2 - E_3}. \tag{3.18}$$

where the Heaviside step function $\theta(t - \tau)$ appears as a consequence of the integration over the delta function.

As will become clear shortly, the two terms of Eq. (3.13) give rise to distinct features, with the first term corresponding to the hyperbolic SBs and the fringes associated with the $E(1s2p)$ energy level; and the second term corresponding to the LISs, associated with the $E(1s2s)$ energy level (see Section 3.1.2 and Fig. 3.1). In the following derivation we treat the terms individually.

3.4.1 Sidebands and Fringes

Given Eqs. (3.14) and (3.17), the first term of Eq. (3.13) can be written as

$$
\langle d \rangle_{a1} = - i\gamma\theta(t-\tau)d_{12}^2 \left[1 - \frac{d_{23}^2 F_{\text{IR}}^2(\tau)}{2(E_2 - E_3)^2} \right]
$$

$$
\times\, e^{i \int_\tau^t dt' E_{2a}(t')} \left[1 - \frac{d_{23}^2 F_{\text{IR}}^2(t)}{2(E_2 - E_3)^2} \right] \tag{3.19}
$$

$$
\approx - i\gamma\theta(t-\tau)d_{12}^2 e^{i \int_\tau^t dt' E_{2a}(t')} \left\{ 1 - \frac{d_{23}^2 \left[F_{\text{IR}}^2(\tau) + F_{\text{IR}}^2(t) \right]}{2(E_2 - E_3)^2} \right\},
$$

where we have neglected a small $\mathcal{O}(F_{\text{IR}}^4)$ term. Focusing on the phase factor in Eq. (3.19), we recognize from Eq. (3.5) that it can be separated as

$$
\exp \left[i \int_\tau^t dt' E_{2a}(t') \right] = \exp\left[iE_2(t-\tau) \right] \exp\left[i\frac{d_{23}^2}{E_2 - E_3} \int_\tau^t dt' F_{\text{IR}}^2(t') \right]. \tag{3.20}
$$

The second exponential factor in Eq. (3.20) can be expanded in orders of the (small) exponent; to first order we have

$$
\exp\left[i\frac{d_{23}}{E_2 - E_3} \int_\tau^t dt' F_{\text{IR}}^2(t') \right] \approx 1 + i\frac{d_{23}^2}{E_2 - E_3} \int_\tau^t dt' F_{\text{IR}}^2(t'). \tag{3.21}
$$

Again neglecting a fourth order term in the IR field, we get

$$
\langle d \rangle_{a1} \approx - i\gamma\theta(t-\tau)d_{12}^2 e^{-iE_2\tau} e^{iE_2 t} \tag{3.22}
$$

$$
\times \left\{ 1 - \frac{d_{23}^2 \left[F_{\text{IR}}^2(\tau) + F_{\text{IR}}^2(t) \right]}{2(E_2 - E_3)^2} + i\frac{d_{23}^2}{E_2 - E_3} \int_\tau^t dt' F_{\text{IR}}^2(t') \right\}.
$$

The changes in the time-dependent dipole moment that lead to the features we are interested in all occur *while* the IR field is interacting with the system; this important fact brings us to the next approximation. Outside of the case where we have a large negative delay τ, the window function $W(t-\tau)$, due to its relatively long period, does not significantly dampen the dipole moment while the IR pulse is active. Instead, it brings the dipole moment to zero after this interaction, when the dipole is ringing with a constant frequency $E(1s2p)$; the main effect of cutting off this oscillation is to change the linewidth of the absorption line at the energy $E(1s2p)$, with the speed with which the oscillation is cut off determining

the width—faster dephasing leading to a broader line. Analyzing the properties of this absorption line is not our objective, and therefore we can neglect the window function in the following.

A related observation can be made about Eq. (3.22), where some of the terms only carry time-dependence (not to be confused with τ-dependence) in the factor $e^{iE_2 t}$. These terms contribute exclusively to the absorption line feature, which—as mentioned above—is not our concern. Hence, we drop any term whose sole time-dependence lie in this factor.

Finally, we consider the Heaviside function. The current presence of $\theta(t - \tau)$ ensures that there is no population in the excited state before the incidence of the XUV pulse. Now we set $\theta(t - \tau) \to 1$, which, when coupled with the exclusion of the window function, ensures that there will be a nonzero population in the excited states at all times. Before these approximations, the IR field would be incapable of influencing the system prior to the arrival of the XUV pulse, which is the reason why, in the regime where the IR pulse precedes the XUV pulse, the ATAS spectrum exhibits a simple absorption spectrum (see Fig. 3.1, where $\tau \gtrsim 20$ fs). After these approximations, the ATAS spectrum is symmetric about $\tau = 0$, and the fringes will not be weaker at large negative τ.

Considering the various regimes of the delay τ, we can make several additional observations about effects of the new approximations. The change in the spectrum due to influence of the IR field at times $t < \tau$, an influence which in principle is made possible when we set $\theta(t-\tau) = 1$, is not significant at large negative delays, as the IR field would be zero regardless of the approximation. In the region where the negative τ approaches $\tau = 0$, the trailing part of the dipole moment (where $t > \tau$) dominates, and the change relative to when $\theta(t - \tau)$ was included is small. When $\tau = 0$ the leading part of the dipole moment (where $t > \tau$) equals the trailing part, and the effects of the approximation increase in significance. As we reach the regime of positive τ, the leading part of the dipole moment starts to dominate, and the spectrum will increasingly diverge from numerically calculated spectrum. The effects described here will be further elucidated through the direct comparison of several spectra, in Section 3.5.

With the changes we have described, the dipole moment can now be expressed as

$$\langle d \rangle_{a1} = \frac{\gamma d_{12}^2 d_{23}^2}{E_2 - E_3} e^{-iE_2\tau} e^{iE_2 t} \left[\int_\tau^t dt' F_{IR}^2(t') + i \frac{F_{IR}^2(t)}{2(E_2 - E_3)} \right], \qquad (3.23)$$

from which it is possible to obtain the analytical Fourier transform $\tilde{d}_{a1}(\omega, \tau)$; this transformation is relegated to Appendix A.1. Given the delta function

representation of the XUV field [Eq. (3.16)], obtaining its Fourier transform is straightforward, and we have

$$\tilde{F}_{\text{XUV}}(\omega, \tau) = \mathcal{F}[\gamma\delta(t - \tau)](\omega)$$
$$= \frac{1}{\sqrt{2\pi}} \int_{-\infty}^{\infty} dt\,\gamma\delta(t - \tau)e^{i\omega t} \tag{3.24}$$
$$= \frac{\gamma}{\sqrt{2\pi}}e^{i\omega\tau}.$$

From the expression for the Fourier transformed XUV pulse in Eq. (3.24); the expressions for the dipole moment in Eq. (3.23); Eqs. (A.2), (A.1), (A.16), and (A.10) from the Appendix; and the definition of the response function in Eq. (2.7), with $F_{\text{in}}^*(\omega, \tau) = F_{\text{XUV}}^*(\omega, \tau)$, we obtain the following closed analytical form representing the SBs and fringes:

$$\tilde{S}_{a1}(\omega, \tau) = \frac{\sqrt{\pi}\gamma^2\rho d_{12}^2 d_{23}^2 F_{0,\text{IR}}^2 T_{\text{IR}}}{4\sqrt{2}(E_2 - E_3)c} \left[\frac{1}{\omega - E_2} - \frac{1}{2(E_2 - E_3)} \right]$$
$$\times \omega \cos\left[\tau(E_2 - \omega)\right] \left\{ \exp\left[\frac{-T_{\text{IR}}^2(\omega - E_2 + 2\omega_{\text{IR}})^2}{32} \right] \right.$$
$$+ \exp\left[\frac{-T_{\text{IR}}^2(\omega - E_2 - 2\omega_{\text{IR}})^2}{32} \right] \tag{3.25}$$
$$\left. - 2\exp\left[\frac{-T_{\text{IR}}^2(\omega - E_2)^2}{32} \right] \right\},$$

where we note that the divergence at $\omega = E_2$, due to the $(\omega - E_2)^{-1}$ factor, can be eliminated by the substitution $E_2 \to E_2 - i\Gamma/2$, where Γ corresponds to a finite radiative lifetime of the energy level E_2. Given the fact that the SBs and fringes are described by Eq. (3.25), we can deduce both the physical origins of each of the features within the framework of the adiabatic model, and how they are directly characterized by the properties of the system and the fields.

We start by considering the three exponential terms inside the curly brackets. These exponentials determine the positions of the features, as they cause Gaussian modulation as a function of frequency ω about $\omega = E_2$ (SBs) and $\omega = E_2 \pm 2\omega_{\text{IR}}$ (fringes); we show in Appendix A.1 that the latter arise directly as a result of the carrier factor $\sin(\omega_{\text{IR}}t)$ of the field, while the former—single—exponential arises from the envelope factor. Given a field defined solely with an envelope then, the SBs would remain, and the fringes would disappear. We also note that the width of the features

are strongly dependent on the factor T_{IR}^2 in the exponent, implying that a longer IR pulse translates to narrower features—as would be expected from standard relations between lifetimes and line widths. Going further back, we see that expressions giving rise to the exponentials here, $F_{IR}^2(t)$ and $\int_\tau^t dt' F_{IR}^2(t')$ [see Eqs. (A.1) and (A.2)], originate in the phase factor $\exp\left[-i\int_\tau^t dt' E_{2a}(t')\right]$ and the coupling term $\langle\psi_1|\hat{d}|\psi_{2a}\rangle$, respectively [see the first term in Eq. (3.13)]; whereas the complex amplitude a_2^* plays a relatively minor role. Moreover, in light of the connection we have just made, the phase factor gives rise to the term $(\omega - E_2)^{-1}$, and the coupling term gives rise to the term $-[2(E_2 - E_3)]^{-1}$ in Eq. (3.25); these two terms interfere constructively for $\omega < E_2$, and destructively for $\omega > E_2$, which is why the upper fringes in Fig. 3.1 appear dim relative to lower fringes. We also note that for the SBs, which lie close to the energy E_2, the factor $(\omega - E_2)^{-1}$ will be significantly larger than the factor $-[2(E_2 - E_3)]^{-1}$; since the former stems from the phase factor $\exp\left[-i\int_\tau^t dt' E_{2a}(t')\right]$, we can infer that the SBs are more attributable to the phase factor than to the coupling term $\langle\psi_1|\hat{d}|\psi_{2a}\rangle$.

An important observation is that the SBs and fringes emerge from the same term, which is associated with the adiabatic state originating in the field free $|1s2p\rangle$ bright state. When interpreting these features through Eq. (3.25), it is clear that they share all characteristics except their location in the spectrum (in terms of frequency), which affects their appearance due to factors depending on frequency. For example, the hyperbolic line shapes [32] of both the SBs and fringes (see Fig. 3.1) are manifestations of the same factor, $\cos[\tau(E_2 - \omega)]$, which is an interference term emerging from the combination of the factor $e^{-iE_2\tau}$ stemming from the E_{2a} phase factor in Eq. (3.13) and the XUV field factor $\tilde{F}_{XUV}(\omega, \tau)$ [see Eq. (3.24)]. The significant implication of this is that the present formalism leads to a unified description of the two ATAS features, which previously have been attributed to two distinct processes—the SBs considered as a signature of perturbed free-induction decay [67, 68], and the fringes ascribed to the dressing of the quantum state by an IR pulse [64–66].

Lastly, having dealt with all parts of the expression in Eq. (3.25) responsible for qualitative aspects of the features, we can consider the factors that determine the signal strength of the two features in the spectrum. The factors γ^2 and $F_{0,IR}^2$ demonstrate the relationship between the intensities of the fields and the signal; T_{IR} implies a proportional increase in signal strength with increasing IR pulse length; the factor $(E_2 - E_3)^{-1}$ signifies a stronger signal with smaller separation between the

energies of excited states; and the factors d_{12}^2 and d_{23}^2 show the role of the TDMs, and in particular that their signs do not make a difference in the spectra. For a discussion on the role of the sign of the a TDM in ATAS, see Ref. [82].

3.4.2 Light-induced Structures

Returning to Eq. (3.13), and now the second term, we seek to describe the final feature highlighted in Fig. 3.1—the LISs. In view of Eqs. (3.18) and (3.15), we have the dipole moment

$$\langle d \rangle_{a2} = -i\theta(t-\tau)\frac{\gamma d_{12}^2 d_{23}^2}{(E_2 - E_3)^2} F_{\text{IR}}(\tau) F_{\text{IR}}(t) e^{i \int_\tau^t dt' E_{3a}(t')}. \qquad (3.26)$$

In the previous section, we found that the adiabatic phases played an important role in the generation of the SBs and fringes. For the LISs the situation is different, as the field-dependent parts of phase factor in Eq. (3.26) will be neglected due to the following argument: the equation is already of second order in the IR field, and with the separation and expansion of the phase factor to first order—equivalent to Eqs. (3.20) and (3.21)—terms of order $\mathcal{O}(F_{0,\text{IR}}^2)$ and $\mathcal{O}(F_{0,\text{IR}}^4)$ remain, where the latter is small and we neglect it. Following the same reasoning as that given after Eq. (3.22), we set $\theta(t-\tau)$ equal to unity and exclude the window function $W(t-\tau)$, yielding

$$\langle d \rangle_{a2} = -i\frac{\gamma d_{12}^2 d_{23}^2}{(E_2 - E_3)^2} e^{-iE_3\tau} F_{\text{IR}}(\tau) e^{iE_3 t} F_{\text{IR}}(t), \qquad (3.27)$$

which can be analytically Fourier transformed (see Appendix A.2). By combining the frequency resolved XUV pulse of Eq. (3.24) and the Fourier transformed dipole moment $\tilde{d}_{a2}(\omega,\tau)$ from Eq. (A.18), the analytical response function [see Eq. (2.7)] representing the LISs is

$$\tilde{S}_{a2}(\omega,\tau) = \frac{\sqrt{\pi}\gamma^2 \rho d_{12}^2 d_{23}^2 F_{0,\text{IR}}^2 T_{\text{IR}}}{2\sqrt{2}(E_2 - E_3)^2 c} \omega \sin\left(\omega_{\text{IR}}\tau\right) \sin\left[\tau(E_3 - \omega)\right]$$

$$\times \exp\left(\frac{-4\tau^2}{T_{\text{IR}}^2}\right) \left\{ \exp\left[-\frac{T_{\text{IR}}^2(\omega - E_3 - \omega_{\text{IR}})^2}{16}\right] \right. \qquad (3.28)$$

$$\left. - \exp\left[-\frac{T_{\text{IR}}^2(\omega - E_3 + \omega_{\text{IR}})^2}{16}\right]\right\}.$$

Like we did for the SBs and fringes in the previous section, we now aim to better understand and describe the LISs via their corresponding analytical response function in Eq. (3.28).

Unlike the case for the other features, the locations of the LISs are restricted in the variable τ in addition to in frequency ω. The exponentials determining the extent of the LISs originate from two factors in the last term of Eq. (3.13). The exponentials inside the curly brackets of Eq. (3.28) stem from the $F_{\mathrm{IR}}(t)$ term in Eq. (3.27), which in turn comes from the coupling term $\langle \psi_1 | \hat{d} | \psi_{3a} \rangle$ [see Eq. (3.15)]. The exponential term $\exp\left(-4\tau^2/T_{\mathrm{IR}}^2\right)$, on the other hand, is the envelope of the field $F_{\mathrm{IR}}(\tau)$ in Eq. (3.27), which originates in the complex amplitude $a_3(t)$ [see Eq. (3.18)]. Comparing the cases of the features then, we see that for all three types of features the couplings terms [Eqs. (3.14) and (3.15)] are important, but the characteristics of the SBs and fringes rely on the adiabatic phase corresponding to the energy E_{2a} [Eq. (3.5)], and not on the adiabatic amplitude $a_2(t)$ [Eq. (3.17)]; whereas for the LISs it is opposite, with the adiabatic amplitude $a_3(t)$ [Eq. (3.18)] playing an important role, and with the adiabatic phase associated with the energy E_{3a} [Eq. (3.6)] wholly neglected [see text after Eq. (3.26). This reflects the prevailing physical understanding of the LISs [70], as a two-photon process in which one XUV photon is absorbed, and one IR photon either absorbed or emitted—simultaneously. This can only happen during temporal overlap of the two fields, which is implied directly by the factor $F_{\mathrm{IR}}(\tau)$ from Eq. (3.18). A pertinent contrast can be made with respect to the fringes, which are visible even at large negative delays τ, due to an initial excitation by the XUV pulse, followed by a dressing of the persisting population in the $|\psi_{2a}\rangle$ state by the IR pulse.

The overall signal strength of the LISs depends on the same quantities as the two other features [compare Eqs. (3.25) and (3.28)], with the exception of a factor $1/2(E_2 - E_3)$, indicating that the LISs are more sensitive to the energy difference between the two field free excited states than the SBs and fringes. Moreover, the LISs also have a hyperbolic line shape, with respect to the E_3 energy, stemming from the combination of the XUV term $\tilde{F}_{\mathrm{XUV}}^*(\omega, \tau)$ [Eq. (3.24)] and the phase factor $\exp\left(-iE_3\tau\right)$.

Finally, we note that the LISs are associated with the field free dark state, which can be understood both from the arguments made in the previous paragraphs, and from the fact that the term in Eq. (3.13) giving rise to the LISs corresponds to the $|1s2s\rangle$ state.

3.5 Comparison of Spectra

In this section we compare the spectra calculated by the various method we have described. First, the numerical calculations, described in Chapter 2. Second, the full adiabatic model, which requires the numerical solving of Eqs. (3.10) and (3.11), followed by insertion into Eq. (3.12) along with the coupling from Eqs. (3.14) and (3.15); and finally the numerical Fourier transforms to obtain $\tilde{d}(\omega, \tau)$ and $\tilde{F}_{\mathrm{XUV}}(\omega, \tau)$, which are then inserted into (2.7). Third, and last, the analytical expressions from Eqs. (3.25) and (3.28). We start by making a general comparison between the numerical spectrum and the full adiabatic model, followed by a comparison between all three methods for each individual feature: the SBs, the fringes, and the LISs. So far the features have been described superficially in Section 3.1.2, and more thoroughly through the lens of the analytical expressions in Eqs. (3.25) and (3.28); in this section we will describe them in more detail, based on their appearance in the various spectra.

We will exemplify our theory with helium, as explained in Section 3.1.1, where the appropriate TDMs and energies are given, as well as all parameters for the fields. The theory we have developed will be valid for other systems and parameters, as long as the approximations and assumptions we have made can be realized. To summarize these conditions: The fields must be weak, to justify the neglecting of certain higher order terms in the IR field, and the use of perturbation theory with respect to the XUV field; the XUV pulse must be short, to justify the delta-function approximation; and finally, the adiabatic approximation requires restrictions on the IR field, such as its frequency not being in resonance with the energy distance between the two excited levels, but we also require that the frequency is not high enough to induce significant population transfer to the excited states higher in the manifold of bound states, as these have been neglected in the three-level model.

3.5.1 Full Spectra

In Fig. 3.3 we compare the numerical calculations from Chapter 2, with $N = 3$ [panel (a)], to the calculations from the full adiabatic three-level model [panel (b)]. As in Fig. 3.1, we have highlighted the relevant features in the model calculations, which will be considered individually shortly. Generally, the adiabatic model yields a good reproduction of the numerical results. Specifically, the SBs surrounding the main absorption line at $E(1s2p) = 21.23$ eV, mainly for negative delays τ, are reproduced very

well. The fringes centered at energies $E_{F+} = 22.01$ eV and $E_{F-} = 20.45$ eV have identical qualitative features in both calculations, but appear slightly dimmer in the adiabatic model calculations. Finally, the LISs see some alterations between the two calculations, with the oscillation pattern being less pronounced for the upper LIS at $E_{LIS+} = 21.01$ eV in the numerical calculations, but more pronounced—and with both positive and negative values—in the numerical calculations for the lower LIS at $E_{LIS-} = 20.23$ eV; the oscillation frequencies, signal strength, and location of the features, however, are well reproduced.

3.5.2   Oscillating Fringes

The oscillating fringes, in the spectra derived from all three methods described at the start of this section, are shown in Fig. 3.4. Fringes above the dashed lines correspond to energies $E(1s2p) + 2\omega_{IR} = 22.01$ eV, and the fringes below the dashed lines correspond to energies $E(1s2p) - 2\omega_{IR} = 20.45$ eV—for each of the three panels. Other than their location in the spectra, the defining characteristics of the fringes include an oscillation with τ at twice the frequency of the IR pulse, the hyperbolic lineshape asymptotically tending towards the line at $E(1s2p) = 21.23$ eV, and the relative weakness of the E_{F+} fringes compared to the E_{F-} fringes— the latter due to the interference cause by the interaction between the adiabatic phases $\exp\left[i \int_{\tau}^{t} dt' E_{2a}(t')\right]$ and the coupling term $\langle \psi_1 | \hat{d} | \psi_{2a} \rangle$. These characteristics are often shared by spectroscopic features attributed to which-way interference [64, 108], where several distinct pathways sharing one state as a final destination cause interference in the spectrum. This can not be the case for the fringes here, which is demonstrated by their presence even at large negative delays. The IR pulse arrives well after the $|1s2p\rangle$ has been populated by the XUV pulse, at which point there are no two distinct processes involving the energy levels $E_{F\pm}$, only a single process involving the dressing of the $|1s2p\rangle$ population by two IR-photons.

Comparing the three spectra in Fig. 3.4, we start by noting the presence of a LIS in Fig. 3.4 (a), below the dotted line. Due to the nature of the numerical calculations, it is not possible to isolate specific features in the spectra, and so even if our focus here are the fringes, the LIS intrude. In the adiabatic model, on the other hand, the same LIS directly corresponds to the second term in Eq. (3.12), so by including only the first term an isolated view of the fringes can be obtained. In Fig. 3.4 (b) the spectrum as calculated by the full adiabatic model is shown, which corresponds very well to the numerical calculations in panel (a). In Fig. 3.4 (c) the
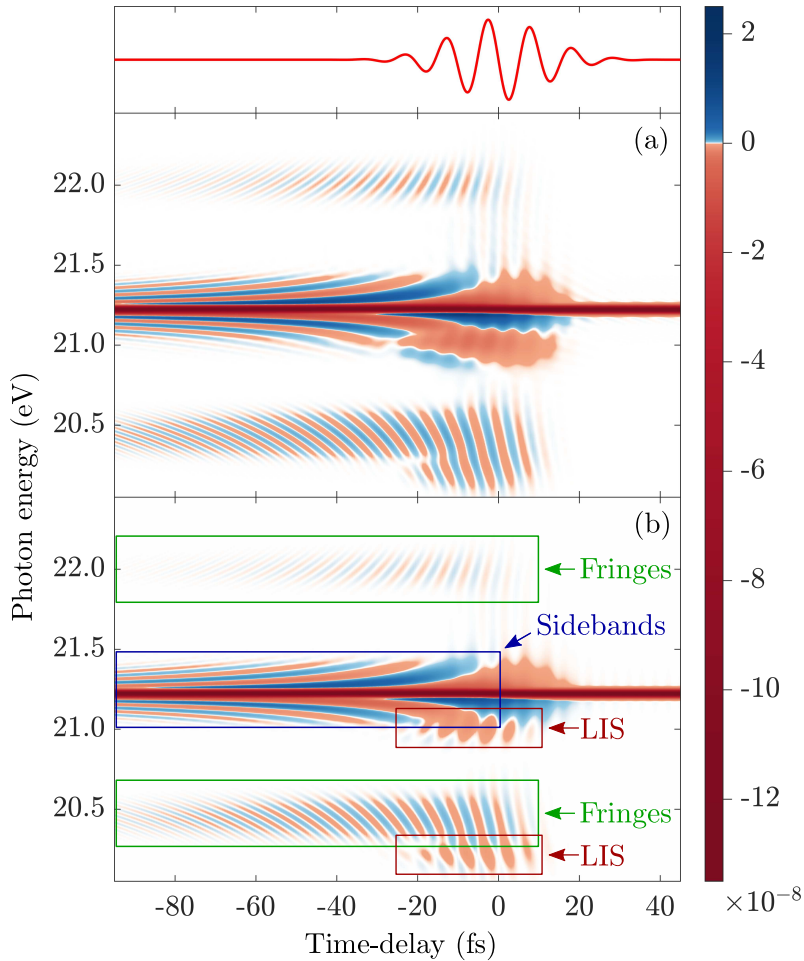
Figure 3.3: Attosecond transient absorption spectrum $\tilde{S}(\omega, \tau)$ of He [Eq. (2.7)], in panel (a) the dipole moment is calculated using the numerical theory presented in Chapter 2, with a basis of $N = 3$ states, as in Fig. 3.2 (b). In panel (b) the dipole moment is calculated using the full adiabatic model [see Eq. (3.12)], and the features of interest are highlighted: Oscillating fringes centered around $E(1s2p) \pm 2\omega_{\mathrm{IR}}$, i.e., at 22.00 and 20.45 eV; hyperbolic sidebands centered around $E(1s2p) = 21.22$ eV; and light-induced structures centered around $E(1s2s) \pm \omega_{\mathrm{IR}}$, i.e., at 21.01 and 20.23 eV. Relevant parameters are given in Section 3.1.1. An illustration of the infrared pulse, centered at $\tau = 0$ fs, is shown in the top panel. The color scale to the right displays the signal strength in arbitrary units. Reproduced with permissions from Phys. Rev. A **96**, 013430 (2017) [1]. Copyright 2017 American Physical Society.
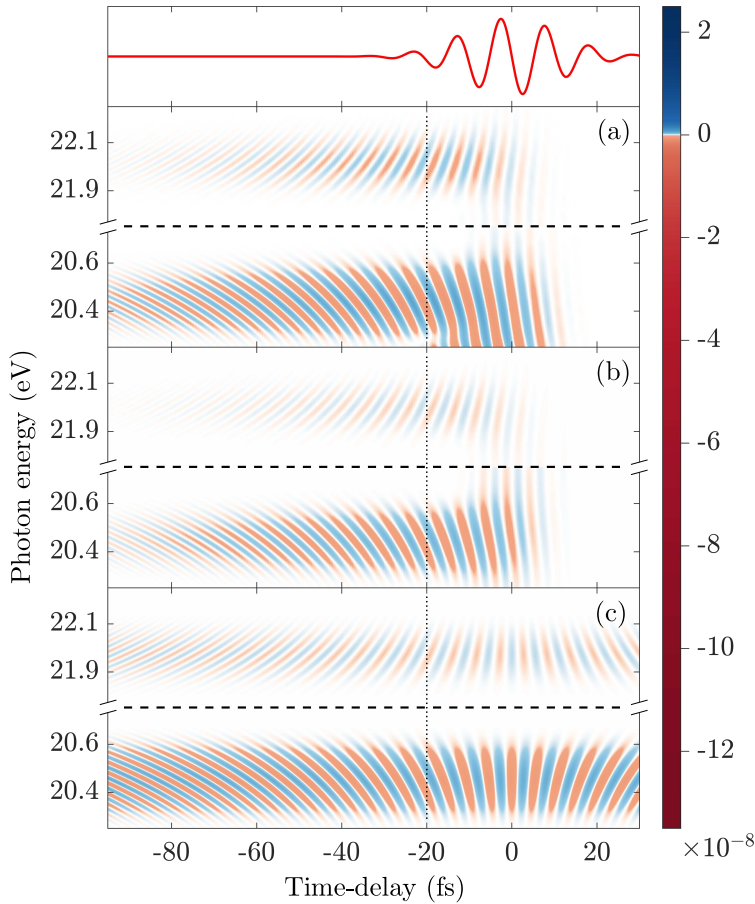
Figure 3.4:   Attosecond transient absorption spectrum $\tilde{S}(\omega, \tau)$ of He [Eq. (2.7)], focused on the oscillating fringes at energies $E_{\text{F}+} = 22.01$ eV (above dashed lines) and $E_{\text{F}-} = 20.45$ eV (below dashed lines). Panel (a) exhibits calculations from the numerical method described in Chapter 2, using $N = 3$ field free basis states. In panel (b) the spectrum as calculated by the full adiabatic model of Section 3.3 is shown. Panel (c) is calculated from the analytical expressions of Eq. (3.25). LISs centered at $E_{\text{LIS}-} = 20.23$ eV and between delays -25 fs $< \tau < 15$ fs cannot be filtered out from the numerical calculations, but are removed from the adiabatic model and analytical expressions, in order to give an unobstructed view of the fringes (see text for details). The vertical dotted line is meant to serve as a guide for the eye. An illustration of the infrared pulse, centered at $\tau = 0$ fs, is shown in the top panel. The color scale to the right displays the signal strength in arbitrary units. Reproduced with permissions from Phys. Rev. A **96**, 013430 (2017) [1]. Copyright 2017 American Physical Society.

spectrum from the analytical expression in Eq. (3.25) is shown. A visual comparison goes a long way towards confirming the validity of the analytical expressions, as they reproduce nearly all relevant characteristics of the complete calculations in panels (a) and (b). A conspicuous difference is that the analytical fringes do not vanish at delays $\tau \gtrsim 10$ fs, and they do not exhibit the gradual dimming at increasingly large negative delays. This is, however, an expected consequence of the omission of the window function and the substitution of the Heaviside function, which is thoroughly described in the text following Eq. (3.22).

3.5.3 Sidebands

The sidebands, again as calculated by each of the three methods, are shown in Fig. 3.5—located around the main absorption line corresponding to the $|1s2p\rangle$ level. The SBs have a width of slightly less than 0.5 eV, and extend from large negative delays to $\tau \approx 10$ fs. They have a hyperbolic profile, which is more pronounced than for the fringes, due to the degree of hyperbolic curvature being dependent on the proximity to the energy $E(1s2p) = 21.23$ eV.

In Fig. 3.5 (a) the results from the numerical calculations are presented. A LIS is again visible in the spectrum, centered at $E_{\mathrm{LIS-}} = 20.23$ eV and between delays -25 fs $< \tau < 15$ fs; as explained in Section 3.5.2, these LISs cannot be removed from the numerically calculated spectrum. The spectrum as calculated by the full adiabatic model are shown in Fig. 3.5 (b), where the SBs are found to be in excellent agreement with the numerical calculations in panel (a). The SBs as described by the analytical expression of Eq. (3.25)—specifically the $-2\exp\left[-T_{\mathrm{IR}}^2(\omega - E_2)^2/32\right]$ term—are given in Fig. 3.5 (c). The analytical form is in agreement with the two other methods, in panels (a) and (b), again accounting for the discrepancy due to the neglecting of the Heaviside- and window function. Note also the absence of main absorption line for the analytical expressions, which was removed with the neglecting of terms with time-dependence only in factors $\exp(iE_2 t)$ [see text following Eq. (3.22)].

3.5.4 Light-induced Structures

In Fig. 3.6, the LISs as calculated by each of the three methods, are shown. The LISs, unlike the two features described prior, are only present for the range of delays τ in which the XUV- and IR-pulses overlap. More specifically, the intensity of the LISs follow the IR-field, oscillating with
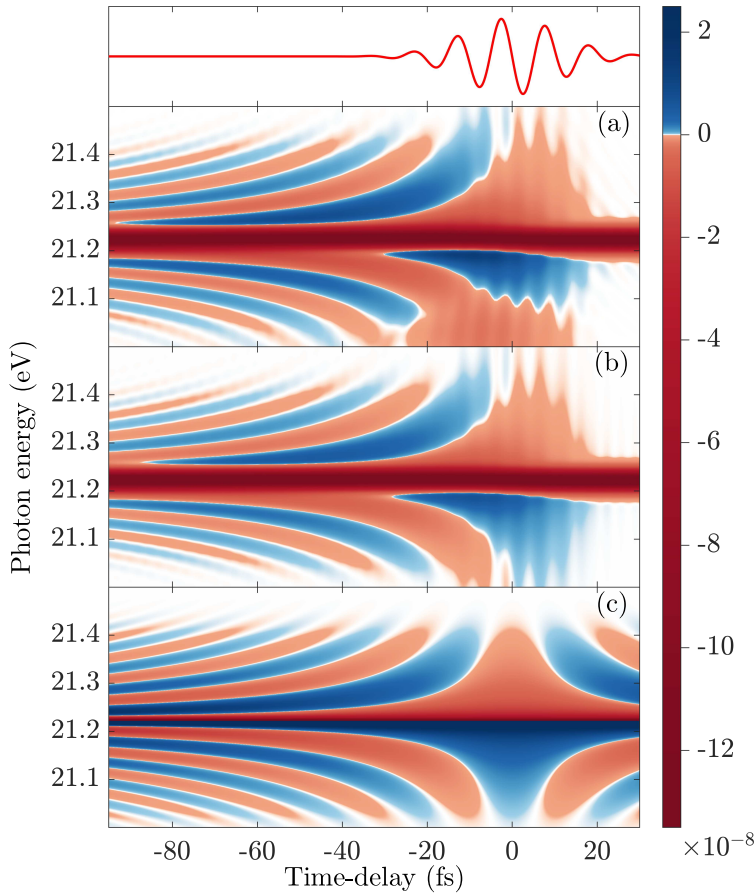
Figure 3.5: Attosecond transient absorption spectrum $\tilde{S}(\omega, \tau)$ of He [Eq. (2.7)], focused on the SBs surrounding absorption line corresponding to single-photon absorption to the $|1s2p\rangle$ state. Panel (a) exhibits calculations from the numerical method described in Chapter 2, using $N = 3$ field free basis states. In panel (b) the spectrum as calculated by the full adiabatic model of Section 3.3 is shown. Panel (c) is calculated from the analytical expressions of Eq. (3.25). LISs centered at $E_{\text{LIS+}} = 21.01$ eV and between delays -25 fs $< \tau < 15$ fs cannot be filtered out from the numerical calculations, but are removed from the adiabatic model and analytical expressions, in order to give an unobstructed view of the SBs (see text for details). An illustration of the infrared pulse, centered at $\tau = 0$ fs, is shown in the top panel. The color scale to the right displays the signal strength in arbitrary units. Reproduced with permissions from Phys. Rev. A **96**, 013430 (2017) [1]. Copyright 2017 American Physical Society.

τ at the frequency ω_{IR}, and dropping to zero for those delays where the instantaneous amplitude of the IR field is zero. A hyperbolic line shape is still present, but less pronounced and obvious than for the other features.

Figure 3.6 (a) exhibits the LISs—along with the other features—from the response function calculated by the numerical method of Chapter 2. As explained previously, a given spectroscopic feature cannot be isolated in the numerical calculations; for the LISs this can be particularly problematic when seeking to glean their characteristics, as they overlap significantly with other features. Here, the upper LIS overlaps with—and is largely obscured by—the SBs, and the lower LIS overlaps with the lower fringes. In Fig. 3.6 (b) the LISs calculated by the full adiabatic model of Section 3.3 are shown, where we again have isolated the relevant feature, this time by keeping only the second term of Eq. (3.13). These isolated LISs differ from their equivalents in the numerical calculations [panel (a)], with the oscillations hard to recognize in the upper LIS, and the lower LIS exhibiting both positive and negative values—unlike the LISs in panel (b). The degree to which these differences are attributable to the removal of interfering features is unclear, but the important characteristics of the location of the LISs, and how they oscillate with τ, agree between the two methods. Lastly, the LISs as described by the analytical expression in Eq. (3.28), are shown in Fig. 3.5 (c). These LISs are in good agreement with the LISs in panel (b), with the best agreement at the largest negative τ, and gradually worse with increasing τ, and no agreement at $\tau \gtrsim 10$ fs, which again can be explained by the neglecting of the Heaviside- and window function [see text after Eq. (3.22)].

3.6   Other Features

In this section we briefly mention two features that are also common to ATAS spectra, which did not appear in the other calculations in the present chapter.

3.6.1   Autler-Townes Splitting

Autler-Townes splitting [78–80] typically occurs when a bright and a dark state are strongly coupled, for example when an incoming field is in one-photon resonance with the two states. It is characterized by a splitting of the absorption line corresponding to the bright state, as seen in Figure 3.7, where resonance was achieved by changing the energy of the $|1s2p\rangle$ state to $E(1s2p) = 21.01$ eV, and where the IR intensity was increased to

Figure 3.6: Attosecond transient absorption spectrum $\tilde{S}(\omega, \tau)$ of He [Eq. (2.7)], focused on the LISs at energies $E_{\mathrm{LIS+}} = 21.01$ eV (above dashed lines) and $E_{\mathrm{LIS-}} = 20.23$ eV (below dashed lines), corresponding to a two-photon transition to the $|1s22\rangle$ state. Panel (a) exhibits calculations from the numerical method described in Chapter 2, using $N = 3$ field free basis states. In panel (b) the spectrum as calculated by the full adiabatic model of Section 3.3 is shown. Panel (c) is calculated from the analytical expressions of Eq. (3.25). The vertical dotted line is meant to serve as a guide for the eye. An illustration of the infrared pulse, centered at $\tau = 0$ fs, is shown in the top panel. The color scale to the right displays the signal strength in arbitrary units. Reproduced with permissions from Phys. Rev. A **96**, 013430 (2017) [1]. Copyright 2017 American Physical Society.
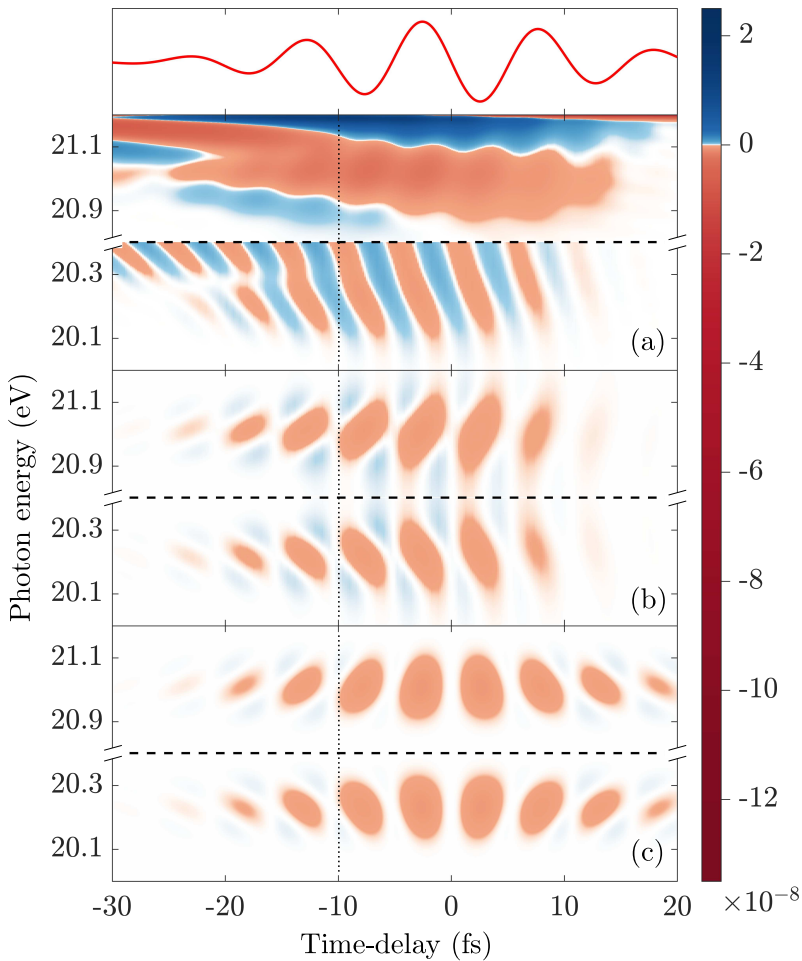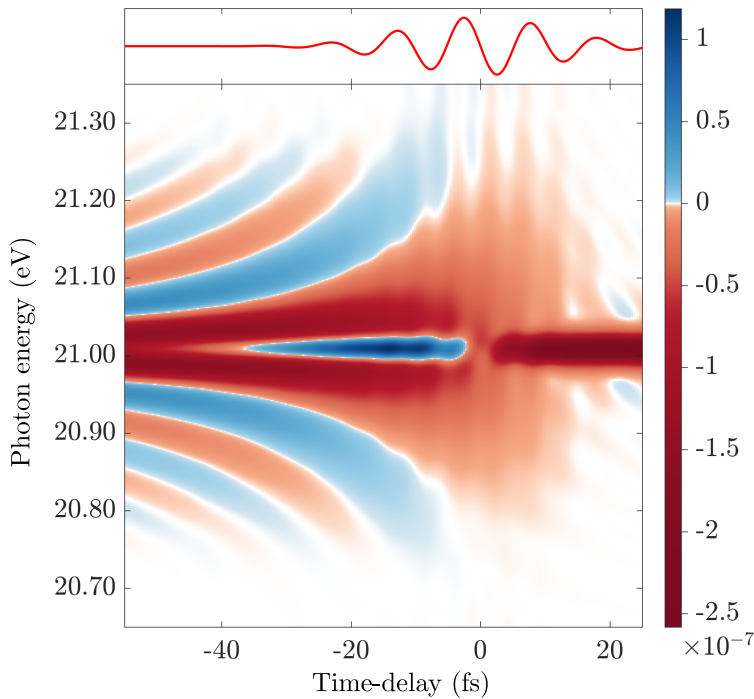
Figure 3.7: Attosecond transient absorption spectrum $\tilde{S}(\omega, \tau)$ of He [Eq. (2.7)], focused on the Autler-Townes splitting of the main absorption line at energy 21.01 eV. The system- and pulse properties are identical to the ones given in Section 3.1.1, with the following exceptions: $E(1s2p) = 21.01$ eV, $I_{\mathrm{IR}} = 3 \times 10^{12}$ W/cm^2, $d_{12} = 1$, $d_{23} = -1$. An illustration of the infrared pulse, centered at $\tau = 0$ fs, is shown in the top panel. The color scale to the right displays the signal strength in arbitrary units.

$I_{\mathrm{IR}} = 3 \times 10^{12}$ W/cm^2. Given that Autler-Townes splitting ordinarily is an indicator of a resonant process, we could not accommodate it in the adiabatic model of Section 3.3.1 without violating the adiabatic condition.

3.6.2 Which-way Interference

Which-way interference [64, 108] can arise in ATAS spectra due to the coherent interaction between processes in the system that involve population transfer to a final state via several distinct pathways. In Chapter 4, we observe which-way interference when exploring the LiF system, and so

we reserve further description and discussion of this phenomenon for that chapter.

Molecules

In this chapter we explore the features of the molecular ATAS spectrum, and specifically how they are affected by the presence of a nonzero permanent dipole. The contents of this chapter overlap with that of Ref. [2], of which I am the first author. My contributions to the study were major in all respects, i.e, derivations of expressions, numerical calculations and interpretation of data, construction of figures, and preparation of the manuscript. Note that several of the figures in this chapter are reproduced directly or adapted—with permissions—from Ref. [2].

The chapter starts out with a primer on molecular ATAS, by way of comparison with atomic ATAS, in Section 4.1. Here we point out the most important effects of nuclear motion in the system under consideration, discuss the impact of the orientation of the molecule with respect to the field, and the presence of nonzero permanent dipoles—all matters which do not appear in the context of atomic ATAS. In Section 4.2 we introduce the specific system we will use to exemplify our theory, LiF, and provide details on the properties of the fields, and window function. In Section 4.3 we present the results from the numerical calculations described in Chapter 2; we look at the difference between nonpolar and polar systems, and discuss the features of the ATAS spectrum corresponding to the LiF molecule. We present, in Section 4.4, the fixed-nuclei adiabatic model, through which we can reproduce the spectra of the fully numerical calculations. In Section 4.5 we analyze the features, specifically the LISs and ladder, in more detail, as enabled by the adiabatic model, and we also derive a fully analytical expressions which describes the adiabatic part of the ladder feature. Finally, in Section 4.6, we investigate how the ATAS spectrum depends on the arrangement of the molecules in the target, in particular

considering molecules that are either oriented or aligned with respect to the incoming fields.

4.1 Molecular Versus Atomic ATAS

In Chapter 3 we gave a broad description of atomic ATAS. Building on this, we can introduce molecular ATAS by considering similarities and differences between the two systems, with an emphasis on the implications for the features of the ATAS spectrum. As mentioned previously, we specifically consider diatomic molecules.

4.1.1 Nuclear Motion

Perhaps the most obvious complicating factor in the treatment of a molecular system, relative to an atomic one, is the inclusion of nuclear motion. Unlike an atom, a molecule is subject to rotations, and internal vibrations about the equilibrium positions of the nuclei. The nuclear masses are large relative to the electron mass, which translates into significantly slower dynamics. Of the two classes of nuclear motion, rotation is the slowest, and on the time scales of the interactions and dynamics we consider here the rotational motion can be neglected—as mentioned in Section 2.25. The consequences of the relative motion of the nuclei, on the other hand, can manifest themselves quite clearly in the ATAS spectrum, which we will show with an example.

In the formalism of Chapter 2 (see Section 2.25), the quantum state of the molecule, $|\Phi\rangle$, is expressed as a linear combination of R-dependent electronic wave functions $|\phi_k\rangle$ ($k = 1, 2, \ldots, N$), with nuclear wave functions $\chi_k(t, R)$ as expansion coefficients. Consider now a system consisting of two PECs ($N = 2$), between which we have some nonzero and constant TDM, D_{12}, but no diagonal couplings. If we induce a population in the excited state, for example with an XUV pulse, then the shape of the excited PEC will determine the motion of the excited nuclear wave packet $\chi_2(t, R)$. In a dissociative state the curvature of the PEC causes the wave packet to move towards greater R, which corresponds to dissociation, i.e., molecular breakup.

The situation is illustrated Fig. 4.1, where the ground state nuclear wave function is shown in blue at all times, the XUV pulse is shown in purple and is visible at times $t = t_0$ and $t = t_1$, and with the excited nuclear wave function shown in red at times $t = t_1$ and $t = t_2$. The PECs were designed for the purpose of demonstration, but closely resemble the two
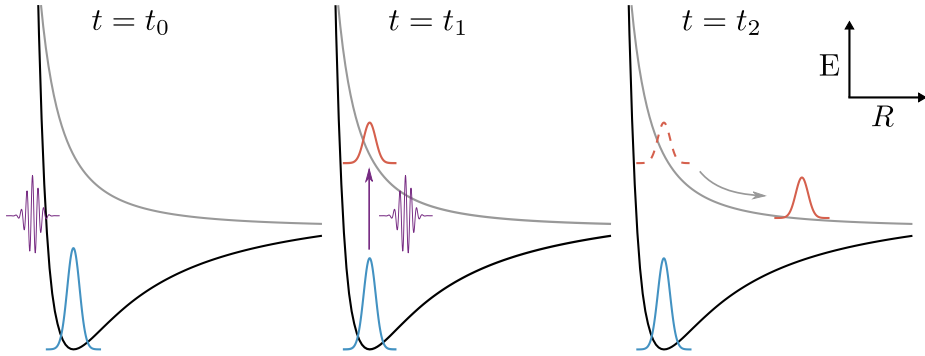
Figure 4.1: Pictorial representation of a dissociative process following excitation by an XUV pulse, in a model system. Energy along vertical axis, internuclear separation R along horizontal axis. Times follow $t_0 < t_1 < t_2$. At time $t = t_0$ the ground state nuclear wave function $\chi_1(t, R)$ is shown in blue, along with the incoming XUV pulse in violet. At time $t = t_1$ a wave packet $\chi_2(t, R)$, shown in red, is induced by the XUV pulse. At subsequent time $t = t_2$ the excited wave packet has propagated towards greater R due to the slope of the PEC.

PECs of LiF that we will use as our example system later. To understand how this process appears in an ATAS spectrum, we must first consider how the dipole moment in a molecular system changes with time, which is expressed by Eq. (2.25); in this specific system, it reduces to

$$\langle D \rangle_{\mathbf{r}, R} = 2D_{12} \int_0^\infty dR \, \text{Re} \left[\chi_1^*(t, R) \chi_2(t, R) \right]. \tag{4.1}$$

From Eq. (4.1) we can deduce the following: At time $t = t_0$, before the incidence of the XUV pulse, there is no population in the excited PEC, i.e., $\chi_2(t_0, R) = 0 \implies \langle D(t_0) \rangle_{\mathbf{r}, R} = 0$. After population of the excited PEC by the XUV pulse, at time $t = t_1$, we have two nuclear wave functions $\chi_1(t_1, R)$ and $\chi_2(t_1, R)$ that are nonzero for the same values of R, and hence a nonzero time-dependent dipole moment has been established. At the time $t = t_3$ the excited wave packet has propagated to larger R, which means that $\chi_1(t_3, R)$ and $\chi_2(t_3, R)$ are not simultaneously nonzero for any R, and the dipole has effectively been cut off. The important factor here is *how long* it takes for the excited wave packet to propagate to a region where it is no longer overlapping in R with the ground state wave

packet. The longer the nuclear wave functions are overlapping, the longer we will have an oscillating time-dependent dipole, which determines how well defined the absorption line is. Furthermore, some features—like the oscillating fringes described in Chapter 3—require a persisting population in an excited state; either because they require time to build up, or because the IR pulse arrives much later than the XUV pulse. If the excited nuclear wave function departs relatively quickly, these features will not appear.

The time it takes for the wave functions $\chi_1(t, R)$ and $\chi_2(t, R)$ to no longer overlap in R after excitation depends on the slope of the excited PEC. For the first excited curves of LiF—given in Section 4.2, Fig. 4.3—the slope is less steep than in Fig. 4.1, and the time it takes for the excited wave packet to propagate out of the overlap region is on the order of a few femtoseconds. We can compare this with the time it takes for the window function to dephase the excited state in the He atom in Chapter 3, which is on the order of a few hundred femtoseconds. Given a difference of two orders of magnitude, we expect the molecular absorption line to be significantly broader. This effect was directly investigated in Ref. [52], where the authors compared the spectra from calculations using normal nuclear motion, with spectra where the nuclear coordinate was fixed. With free nuclear motion the spectra did indeed exhibit relatively broad absorption features—a sign of less well-defined frequencies—due to the relatively short lifetime of the oscillating dipole.

4.1.2   Orientation

Due to the spherical symmetry of the atomic ground states in Chapter 3, it is meaningless to consider the orientation of the atom with respect to the incoming fields. When dealing with molecules, however, it is crucial to consider this orientation. For the majority of this chapter, we will assume that all target molecules have a set orientation with respect to the incoming fields; the exception being in Section 4.6, where we consider a target of aligned molecules, where two opposite orientations are assumed—in equal measure. Note that the latter only is relevant for heteronuclear molecules, as two oppositely oriented homonuclear molecules would be indistinguishable in terms of their ATAS signal.

As in the previous chapter, we assume that the fields are linearly polarized in the z-direction. The molecule is oriented in such a way that its axis of symmetry is aligned with the polarization direction of the fields. In the following we will use the lithium fluoride (LiF) molecule to exemplify our theory (see Section 4.2), and in Fig. 4.2 the molecule is shown relative
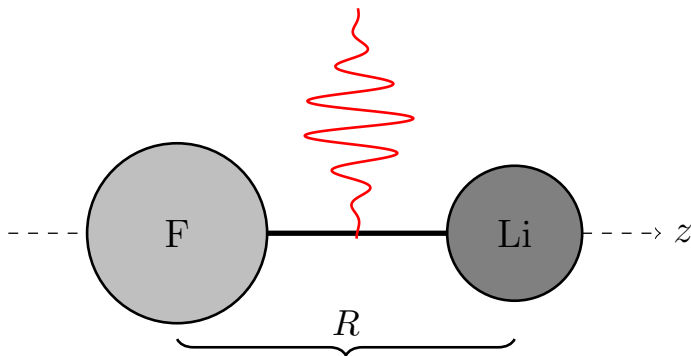
Figure 4.2: Illustration of the LiF molecule and the incoming IR field. The molecular axis lies in parallel with the polarization direction of the field, along the z-direction, and perpendicular to the propagation direction of the field. R is the internuclear separation. Reproduced with permissions from Phys. Rev. A **98**, 053401 (2018) [2]. Copyright 2018 American Physical Society.

to the incoming IR field. Other orientations than the ones we consider in this thesis have been explored previously. In Ref. [109], the authors considered several angles between the polarization direction of the fields and the internuclear axis of a diatomic molecule, and found that the coupling strengths of specific transitions were affected by this orientation.

4.1.3 Permanent Dipoles

Another distinguishing characteristics of certain molecules compared to atoms is that they can have a nonzero permanent dipole, so that diagonal elements D_{kk} are nonzero [see Eqs (2.21) and (2.26)]. This property is not inherent in all molecules, and the majority of molecular ATAS research so far has been focused on nonpolar homonuclear atoms [48–52, 71, 109], with a recent exception where CO molecules were considered [110]. How the presence of a nonzero permanent dipole affects the ATAS spectrum then, is relatively uncharted territory, and is the main focus of this chapter.

4.2 System Properties and Field Parameters

Before delving into the numerical and adiabatic calculations, we introduce here the system we have chosen to exemplify our theory with—LiF—and the

parameters of the fields applied in this chapter. The system is chosen with the purpose of producing the features of interest in ATAS, while keeping the setup as simple as possible. In Section 3.2.1, we showed how including only a subset of bound states in a basis set is a valid approximation, given that the subset is properly isolated from the other states, which depends both on the system and on the fields—the parameters are chosen with this in mind.

The two lowest BO-curves of LiF, $E_1(R)$ and $E_2(R)$, and the corresponding dipole moments, $D_{11}(R)$, $D_{12}(R)$, and $D_{22}(R)$, are shown in Fig. 4.3. We start by noting the shaded area of the figure, which covers the region where the curves exhibit an avoided crossing. In this region the non-adiabatic terms appearing in Eq. (2.36) grow large, but due to their location, at relatively large R, they would not have played any significant role in our calculations—see Section 4.1.1. How the non-adiabatic terms can affect the ATAS spectrum in other situations is an interesting research topic, and will be discussed briefly in Chapter 5.

A pertinent comparison can be made between the LiF system, and the He system used in Chapter 3; here we use only two curves of LiF, whereas for He we used three levels. The important difference lies in the distance between the LiF ground state with the first excited curve, which is small enough to allow for a mixing of the two states—a necessary condition for certain processes to take place. In the He atom, the excited states are relatively far removed from the ground state, and so it was necessary to included two excited states to allow for state mixing.

Given the relatively small distance between the ground state- and excited curves in LiF, a single-photon absorption between the curves requires a lower photon energy than for He, in Chapter 3. This brings the ultraviolet photon energy out of the XUV regime, and henceforth we refer to the pulse simply as the UV pulse. We note that in Chapter 3 the bandwidth of the XUV pulse was broad enough that it could be considered constant over the relevant range of interest. The magnitude of the UV pulse used here varies significantly over the range of energies of interest, and will directly influence the signal strength of the features of the spectrum. As for the IR pulse, we use a lower wavelength, which brings it into the NIR regime. The field parameters are (see Section 2.3.1): $\lambda_{\text{NIR}} = 800$ nm (corresponding to $\omega_{\text{NIR}} = 1.55$ eV), $\lambda_{\text{UV}} = 160$ nm (corresponding to $\omega_{\text{XUV}} = 7.75$ eV), $I_{\text{NIR}} = 10^{12}$ W/cm^2, $I_{\text{XUV}} = 5 \times 10^7$ W/cm^2, $T_{\text{NIR}} = 40.01$ fs ($N_{c,\text{IR}} = 15$), and $T_{\text{XUV}} = 1.07$ fs ($N_{c,\text{XUV}} = 2$). The CEP φ is set to zero for both fields, except in Section 4.6. The target density is arbitrarily set to $\rho = 1$ [see Eq. (2.7)]. As in Chapter 3 the FWHM of the Gaussian corresponding to
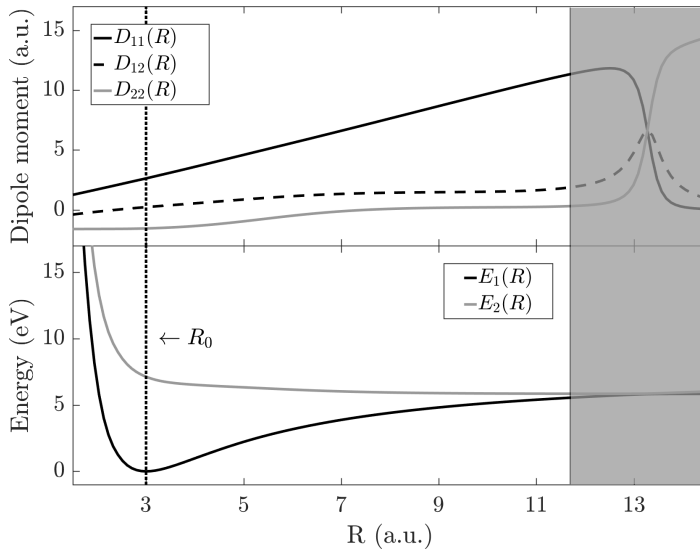
Figure 4.3: Dipole moments (top panel) and Born-Oppenheimer curves (bottom panel) of LiF, as functions of the internuclear spacing R. The gray shaded area covers the region where the curves intersect; the shading is meant to signify that this intersection is inconsequential in our calculations. The dotted line indicates the center of the ground state nuclear wave function, at $R_0 = 3$, where we have $D_{11}(R_0) = 2.62$, $D_{12}(R_0) = 0.22$, $D_{22}(R_0) = -1.55$, $E_1(R_0) \equiv 0$, $E_2(R_0) = 7.07$ eV. Curves from interpolated data given in Ref. [111]. Adapted with permissions from Phys. Rev. A **98**, 053401 (2018) [2]. Copyright 2018 American Physical Society.

our window function (see Section 2.5) is chosen to be large enough that the features of interest are unaffected, which amounts to $T_{\text{FWHM}}/2 = 100$ fs.

When applying the window function to the He system in Chapter 3, the time at which the XUV pulse arrived, $t = \tau$, served as a natural starting point for the window function because no dynamics could take place before that point in time, and so we set $t_w = \tau$. For the LiF system, however, the proximity of the ground state PEC to the excited PEC enables the NIR pulse to induce dynamics in the system even before the UV pulse arrives. To ensure that we do not disrupt the dipole moment prematurely, we now set the window function to start at the end of the last pulse. This choice is in general less consequential than in Chapter 3, in part due to the relatively rapid suppression of the dipole moment due to the diverging

wave packets, as outlined in Section 4.1.1.

4.3 Numerical Calculations

We start the ATAS investigation of the polar LiF molecule by employing the numerical methods for molecular dynamics that were described in Chapter 2. First, we consider the new features of the spectrum, before exploring the role that the nonzero permanent dipole plays in their conception. The numerical calculations of this section are supplemented in the following section by an adiabatic model based on similar assumptions as the one derived in Chapter 3, which sheds further light on the nature of the features.

Specifically, the numerical routine starts with the calculation of the ground state nuclear wave function through imaginary time propagation, as described in Section 2.4.4. The propagation of the wave packets under the influence of the incoming fields is expressed by the coupled Equations (2.36), which are solving using the split operator method (see Section 2.4.2), with time step $\Delta t = 0.05$, box size $R_{\max} = 25$, and grid resolution $\Delta R = R_{\max}/N_R$, with $N_R = 1024$ grid points. A complex absorbing potential is active close to the box limit (see Section 2.4.3). The nuclear wave functions $\chi_k(t)$ are then inserted into Eq. (2.25), and the integrals solved numerically. Finally, we take the Fourier transform and insert into Eq. (2.7) to obtain the ATAS spectra.

4.3.1 Nonpolar Equivalent

With the properties of the system and the field as given in Section 4.2, and if we disregard the permanent dipoles for the moment, then—in the language used previously—we would classify the excited curve as a bright state, which can be accessed via a dipole allowed transition from the ground state. Such a system, where we have $D_{11}(R) = D_{22}(R) = 0$, is equivalent to LiF, with the exception of the neglected effect of the polarity of the system on the dynamics of the interaction. The corresponding numerically calculated ATAS spectrogram is shown in Fig. 4.4, where we see only a broad delay-independent absorption line in the spectrum. The broadening can be understood from the discussion of a system with a single dissociative excited PEC in Section 4.1.1, as the LiF system we use closely resembles the illustrative example of that section. The absence of any delay-dependent features in the figure can be understood by comparison with the atomic case in Chapter 3, where all delay-dependent features required the presence of an additional dark state.

Figure 4.4: Numerically calculated attosecond transient absorption spectrum $\tilde{S}(\omega, \tau)$ [Eq. (2.7)], using properties of the LiF system, with permanent dipoles set to zero, i.e., $D_{11}(R) = D_{22}(R) = 0$. Only the main absorption line at $E_2(R_0) = 7.07$ eV is visible, exhibiting no τ-dependent features. Relevant parameters are given in Section 4.2. An illustration of the infrared pulse, centered at $\tau = 0$ fs, is shown in the top panel. Towards the left of the figure, the frequency bandwidth of the UV pulse is shown in gray. The color scale to the right displays the signal strength in arbitrary units. Adapted with permissions from Phys. Rev. A **98**, 053401 (2018) [2]. Copyright 2018 American Physical Society.

4.3.2   The LiF ATAS Spectrogram

The numerically calculated LiF spectrogram, now with nonzero permanent dipoles $D_{11}(R)$ and $D_{22}(R)$ as given in Fig. 4.3, is shown in Fig. 4.5. The contrast with Fig. 4.4 is remarkable, and it is immediately apparent that the polarity of the molecule directly influences the dynamics of the interaction—in turn impacting the ATAS spectrum. The features appearing can be divided into three categories, and similarly to in Chapter 3 we start by briefly discussing them, after which we interpret them in the context of an adiabatic model.

Light-induced Structures

Three LISs appear in Fig. 4.5, highlighted by red ellipses. They are located at energies $E_{\text{LIS}-} = E_2(R_0) - \omega_{\text{NIR}} = 5.51$ eV, $E_{\text{LIS}+} = E_2(R_0) + \omega_{\text{NIR}} = 8.61$ eV, and $E_{\text{LIS}+2} = E_2(R_0) + 2\omega_{\text{NIR}} = 10.16$ eV. The LIS at $E_{\text{LIS}+2}$ has the weakest signal, which can be expected as it likely involves three photons—one UV photon and two NIR photons. The difference in signal strength between the LISs at $E_{\text{LIS}-}$ and $E_{\text{LIS}+}$ is presumably attributable to the relative magnitude of the UV pulse bandwidth at the energies—this bandwidth is illustrated in gray in the figure. The $E_{\text{LIS}\pm}$ LISs oscillate in τ at frequency ω_{NIR}, and the $E_{\text{LIS}+2}$ LIS oscillates at frequency $2\omega_{\text{NIR}}$.

In the chapter on atomic ATAS, and in other previous work, e.g., [52, 70], the LISs have been observed surrounding dark states, but never around a bright state. In fact, the concepts of bright and dark states are not necessarily useful in a system with a nonzero permanent dipole; the presence of the LISs in Fig. 4.5, for example, cannot be understood in terms of transitions via states of opposite parity. In a system with a central symmetry transitions between states of identical parity would be forbidden, as encapsulated by the Laporte rule [112]; the LiF system, however, does not possess such symmetry.

Which-way interference

Which-way interference, mentioned briefly in Chapter 3, is a type of interference arising as a result of several distinct processes involving population transfer sharing a final destination [64, 108]. In the present situation, which-way interference is observed, and marked with a blue ellipse, along the middle of the absorption line at $E_2(R_0) = 7.07$ eV in Fig. 4.5. Given the presence of the LISs, we can identify four unique pathways from the ground state PEC to the excited state PEC: Directly, via absorption of one
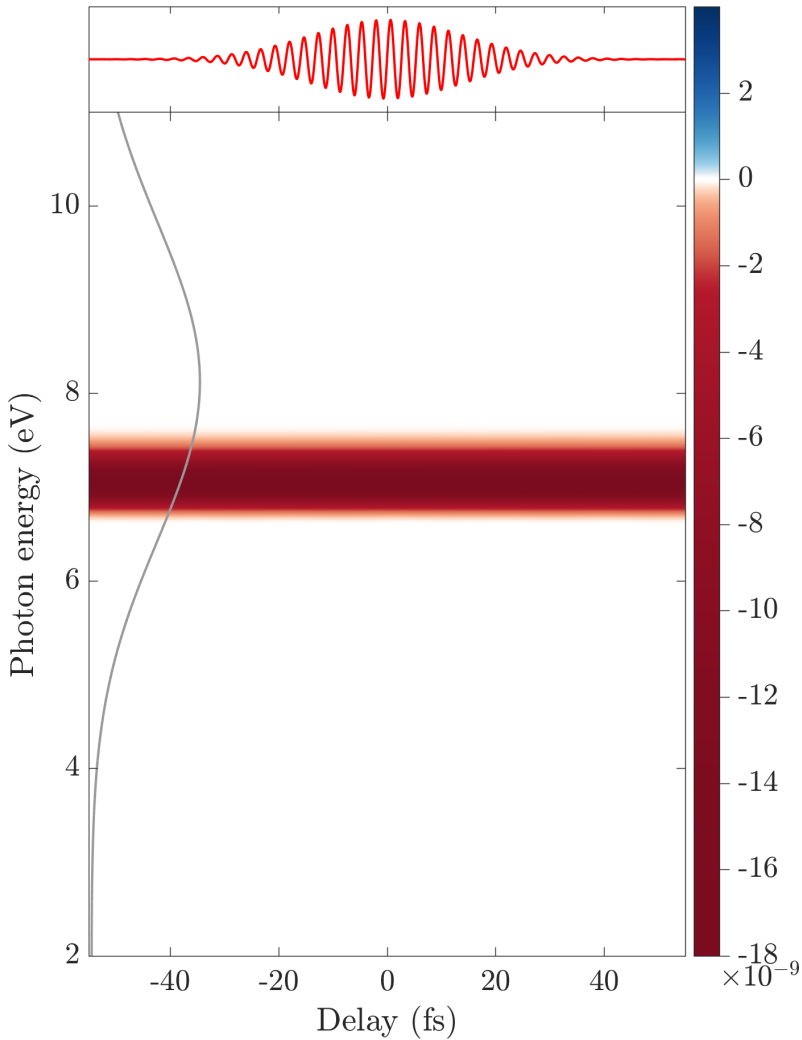
Figure 4.5:   Numerically calculated attosecond transient absorption spectrum $\tilde{S}(\omega, \tau)$ [Eq. (2.7)], of LiF. Relevant features are highlighted: which-way interference pattern (blue) in the main absorption line at $E_2(R_0) = 7.07$ eV; light-induced structures (red) centered at energies $E_2(R_0) \pm \omega_{\mathrm{NIR}}$ and $E_2(R_0) + 2\omega_{\mathrm{NIR}}$, i.e., at 5.51 eV, 8.61 eV, and 10.16 eV; and a ladder structure (green arrows) with rungs centered at energies $E_1(R_0) + n\omega_{\mathrm{NIR}}$, i.e., at n times 1.55 eV, with $n = \{2, 3, 4, 5, 6\}$. Relevant parameters are given in Section 4.2. An illustration of the infrared pulse, centered at $\tau = 0$ fs, is shown in the top panel. Towards the left of the figure, the frequency bandwidth of the UV pulse is shown in gray. The color scale to the right displays the signal strength in arbitrary units. Adapted with permissions from Phys. Rev. A **98**, 053401 (2018) [2]. Copyright 2018 American Physical Society.

UV photon; via absorption of one UV photon and simultaneous absorption or emission of one NIR photon; or via absorption of one UV photon and emission of two NIR photons.

Ladder

The last salient features in Fig. 4.5 are a number of equally spaced bands that oscillate at various frequencies with the delay τ—the positions are indicated by green arrows. On account of their appearance, we will refer to these features collectively as a ladder, with specific lines referred to as rungs. This ladder feature has not been observed or described previously in ATAS; this is likely connected with the fact that polar molecules have not been explored in ATAS, since the ladder appears to be a consequence of the presence of a permanent dipole. Given the rapid oscillations with respect to the delay, especially for the higher rungs, we will now consider a spectrogram exhibiting a smaller range of delays, in Fig. 4.6.

The spectrogram in Fig. 4.6 (a) is identical to the one in Fig. 4.5, and its purpose is to indicate the area of the spectrogram which is shown in panel (b), marked by the gray box. By comparing the oscillations of each rung with the NIR pulse shown in the top panel, we see that the rungs oscillate as $n\omega_{\mathrm{NIR}}$, where $n \in \{2, 3, 4, 5, 6\}$, starting at the lowest rung with $n = 2$. Since we have set $E_1(R_0) = 0$, it means that these rungs are located at n times the NIR photon energy relative to the ground state energy, suggesting that they represent a dressing of the ground state reminiscent of how the oscillating fringes dressed the He bright state in Chapter 3.

Extending the lower range of energies shown in Fig. 4.6 would reveal the first rung of the ladder, at energy $E_1(R_0) + \omega_{\mathrm{NIR}} = 1.55$ eV; however, we have avoided the lower end of the energy range, as it is not practically possible to obtain a signal at these low energies in the experimental ATAS setup. In ATAS we focus on the frequencies that lie within the bandwidth of the UV pulse, whereas the frequencies of the relatively intense NIR pulse are filtered out after the interaction with the target. These low frequencies are typically well separated from the frequencies in the frequency resolved UV pulse, but due to the specific properties of the LiF system we have chosen a UV pulse with lower frequencies than what is normally used in ATAS.
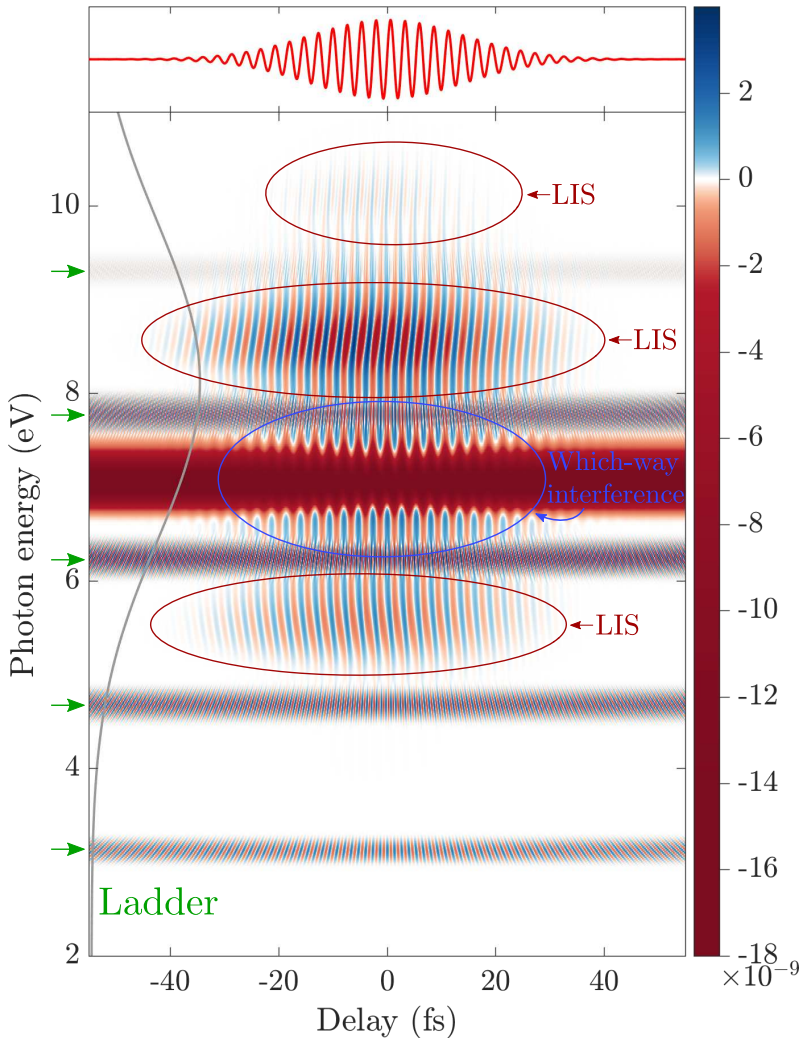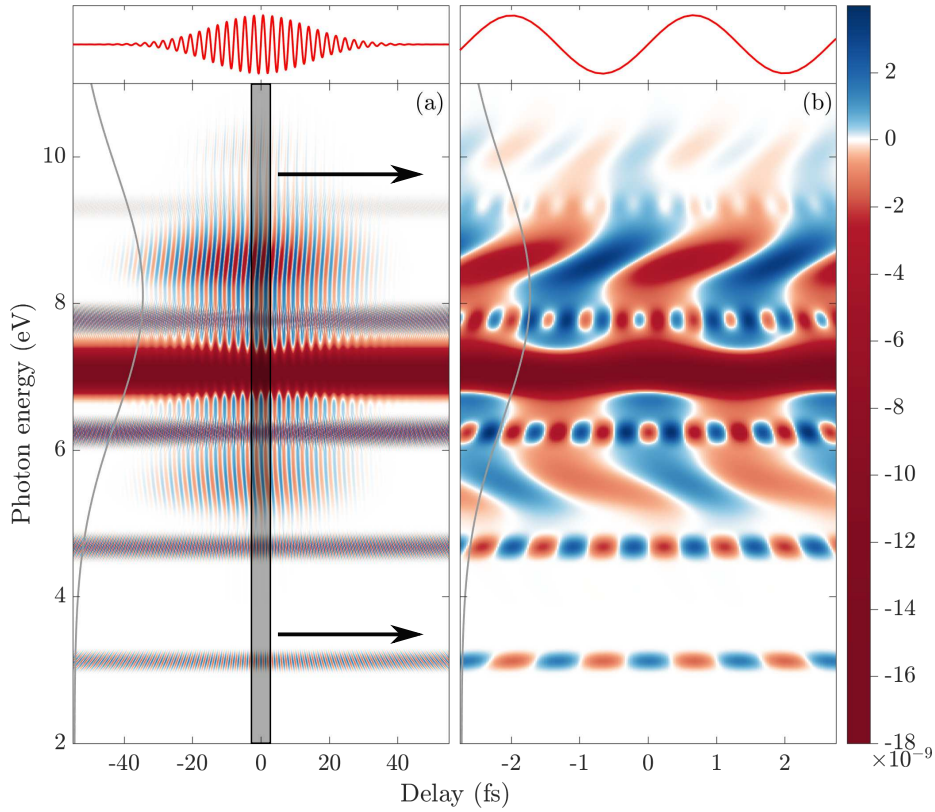
Figure 4.6: Numerically calculated attosecond transient absorption spectrum $\tilde{S}(\omega, \tau)$ [Eq. (2.7)], of LiF. See caption of Fig. 4.5 for description of features in panel (a), which is the same spectrogram. Shaded area in panel (a) indicates the contents of panel (b), which exhibits a small range of the delays of panel (a). Illustrations of the infrared pulse, centered at $\tau = 0$ fs, are shown in the top panels. Towards the left of each panel, the frequency bandwidth of the UV pulse is shown in gray. The color scale to the right displays the signal strength in arbitrary units. Adapted with permissions from Phys. Rev. A **98**, 053401 (2018) [2]. Copyright 2018 American Physical Society.

Absent Features

Compared with the features in atomic ATAS, two features are notably absent from the molecular ATAS spectrum in Fig. 4.5: the sidebands around the main absorption line, and the oscillating fringes. Their absence are both related to the swift departure of the excited wave packet, which cuts off the dipole (see Section 4.1.1); both the SBs and fringes require an enduring overlap between the nuclear wave functions in the two PECs. The fringes in particular, occur due to a dressing of the population in the excited curve by the NIR, and for negative delays of moderate magnitude the NIR arrives after this population—in the form of the nuclear wave function—is gone from the relevant region of internuclear separation. For delays close to zero, the fringes could conceivably be present, but will be obscured by the LISs at the same location. We have confirmed this by neglecting the nuclear kinetic energy term T_{nuc} [see Eq. (2.35)] in the numerical calculations, and thus effectively freezing the motion of the nuclear wave packet; in this artificial situation SBs appear at their usual location, in addition to fringes at $E_2(R_0) \pm \omega_{\mathrm{NIR}}$ and $E_2(R_0) \pm 2\omega_{\mathrm{NIR}}$.

4.4   Fixed-nuclei Adiabatic Model

In this section we use an adiabatic model to derive an alternative representation of the LISs and ladder discussed in Section 4.3. The ansatz of the model is similar to the one in Section 3.3, but with several notable differences due to the specifics of the molecular system. The adiabatic model enables deeper analytical examinations of the features, as compared to its numerical counterpart. Unlike for the atomic case, obtaining closed analytical forms corresponding to each of the features does not constitute a tractable problem, with the exception of the part of the ladder feature which can be attributed adiabatic dynamics. Nonetheless, the semi-analytical expressions we can obtain, yield clear insights into the nature of the full LISs and ladder in the ATAS of polar molecules.

To make any progress in this analytical derivation, it is necessary that the internuclear distance is frozen, at the distance corresponding to the center of the of the ground state nuclear wave function, $R_0 = 3$, which is marked by the dotted line in Fig. 4.3; thus, in the following, all quantities with R-dependence are evaluated at $R_0 = 3$. This amounts to neglecting the nuclear kinetic energy term T_N, as expressed in Eq. (2.35). Judging from the discussion in Section 4.1.1, and the results mentioned in the end

of Section 4.3.2, this will have significant consequences for the dynamics of the system, which must be mitigated.

In the specific system we are considering, the main effect on the dipole moment due to nuclear motion is its suppression within a few femtoseconds of excitation, due to dissociation. By applying the window function factor defined in Eq. (2.49), this time multiplied by the complex coefficient for the excited state, we effectively reproduce this effect, as will be shown in the upcoming results. The period of this window function, $W_N(t - t_w)$, is set to $T_w = T_N = 3.6$ fs, and it is initiated at the instant of excitation by the UV pulse, i.e., $t_w = \tau$.

In Section 4.2 we explained that in the current system the NIR pulse can induce dynamics in the system independently of the UV pulse (which was not the case in Chapter 3); the choice of $t_w = \tau$ for W_N could therefore be problematic for large negative delays, as subsequent dynamics induced solely by the NIR pulse could be erroneously neglected. In what follows, we circumvent this problem by treating features that depend exclusively on the NIR pulse separately. In this case it is not necessary to multiply the coefficient for the excited state by the window function W_N, as the NIR pulse on its own only induces a temporary population in the excited curve, as opposed to the UV pulse, which creates a wave packet in the excited curve that remains even after the pulse.

4.4.1 Molecular Adiabatic System

The derivation of the adiabatic model in this chapter, is similar to its atomic analogue in Chapter 3, but with important differences due to the molecular structure and the polarity of the system. The molecular adiabatic states $|\phi_{ka}(t)\rangle$ are defined by

$$[H_e - F_{\mathrm{NIR}}(t)\hat{D}] |\phi_{ka}(t)\rangle = E_{ka}(t) |\phi_{ka}(t)\rangle, \qquad (4.2)$$

where $H_e - F_{\mathrm{NIR}}(t)\hat{D}$ is the full Hamiltonian, excluding the interaction due to the UV pulse. The full state of the system $|\Phi_a(t)\rangle$ is expressed as

$$|\Phi_a(t)\rangle = b_1(t) |\phi_{1a}(t)\rangle \, e^{-i \int_{t_0}^{t} dt' E_{1a}(t')} + b_2(t) |\phi_{2a}(t)\rangle \, e^{-i \int_{t_0}^{t} dt' E_{2a}(t')}, \qquad (4.3)$$

where we have replaced the nuclear wave functions $\chi_k(t, R)$ from Section 2.3.3 by the coefficients $b_k(t)$ to reflect that we are working within a fixed-nuclei approximation. The exponential factors $\exp\left(-i \int_{t_0}^{t} dt' E_{ka}\right)$ are the phase-factors for the time-dependent adiabatic energies, equivalent to the phase factors used in Section 3.3.1.

Our objective is to obtain $\langle D \rangle_a = \langle \Phi_a(t) | \hat{D} | \Phi_a(t) \rangle$, and the first step is to determine the coefficients, states, and phases, of Eq. (4.3). Note that calculating $\langle D \rangle_a$ does not involve integration over R, as $R = R_0$ is now a fixed parameter of the calculations.

4.4.2 Adiabatic States and -Energies

The adiabatic states $|\phi_{ka}(t)\rangle$, and corresponding energies $E_{ka}(t)$, can be obtained as the eigenstates and -energies of the matrix representation of the Hamiltonian,

$$\underline{\underline{H}} = \begin{bmatrix} E_1(R_0) - F_{\mathrm{NIR}}(t) D_{11}(R_0) & -F_{\mathrm{NIR}}(t) D_{12}(R_0) \\ -F_{\mathrm{NIR}}(t) D_{12}(R_0) & E_2(R_0) - F_{\mathrm{NIR}}(t) D_{22}(R_0) \end{bmatrix}, \quad (4.4)$$

which is expressed in a basis of the field free states $|\phi_1\rangle$ and $|\phi_2\rangle$. In Eq. (4.4) we have used that $H_e |\phi_k\rangle = E_k(R_0) |\phi_k\rangle$. The energies are

$$E_{1a}(t) \approx E_1(R_0) - D_{11}(R_0) F_{\mathrm{NIR}}(t) - \frac{D_{12}^2(R_0) F_{\mathrm{NIR}}^2(t)}{E_1(R_0) - E_2(R_0)}, \quad (4.5)$$

$$E_{2a}(t) \approx E_2(R_0) - D_{22}(R_0) F_{\mathrm{NIR}}(t) + \frac{D_{12}^2(R_0) F_{\mathrm{NIR}}^2(t)}{E_1(R_0) - E_2(R_0)}, \quad (4.6)$$

where the energies have been expanded about $F_{\mathrm{NIR}}(t) = 0$, and only terms up to second order, $\mathcal{O}(F_{\mathrm{NIR}}^2)$, have been kept. The normalized eigenstates of the matrix in Eq. (4.4) are

$$\begin{aligned} |\phi_{1a}(t)\rangle = & -\frac{E_{1a} - E_2 - D_{22} F_{\mathrm{NIR}}}{\sqrt{D_{12}^2 F_{\mathrm{NIR}}^2 + (E_{1a} - E_2 - F_{\mathrm{NIR}} D_{22})^2}} |\phi_1\rangle \\ & -\frac{D_{12} F_{\mathrm{NIR}}}{\sqrt{D_{12}^2 F_{\mathrm{NIR}}^2 + (E_{1a} - E_2 - F_{\mathrm{NIR}} D_{22})^2}} |\phi_2\rangle, \end{aligned} \quad (4.7)$$

and

$$\begin{aligned} |\phi_{2a}(t)\rangle = & -\frac{D_{12} F_{\mathrm{NIR}}}{\sqrt{D_{12}^2 F_{\mathrm{NIR}}^2 + (E_{2a} - E_1 - D_{11} F_{\mathrm{NIR}})}} |\phi_1\rangle \\ & -\frac{E_{2a} - E_1 - D_{11} F_{\mathrm{NIR}}}{\sqrt{D_{12}^2 F_{\mathrm{NIR}}^2 + (E_{2a} - E_1 - D_{11} F_{\mathrm{NIR}})}} |\phi_2\rangle. \end{aligned} \quad (4.8)$$

4.4.3 Complex Adiabatic Amplitudes

In order to obtain the coefficients $b_1(t)$ and $b_2(t)$, we insert $|\Phi_a(t)\rangle$ from Eq. (4.3) into the TDSE, with the Hamiltonian

$$H = H_e - F_{\mathrm{NIR}}(t)\hat{D} - F_{\mathrm{UV}}(t, \tau)\hat{D}. \tag{4.9}$$

Employing Eq. (4.2), we can obtain equations for the time derivatives, $\dot{b}_1(t)$ and $\dot{b}_2(t)$, by projecting the TDSE onto the adiabatic states, $|\phi_{1a}\rangle$ and $|\phi_{2a}\rangle$, respectively. The two coupled equations are

$$\begin{aligned} \dot{b}_1 = {}&ib_1 F_{\mathrm{UV}} \langle\phi_{1a}|\hat{D}|\phi_{1a}\rangle - b_2 \langle\phi_{1a}|\dot{\phi}_{2a}\rangle \, e^{-i \int_{t_0}^{t} dt'(E_{2a}-E_{1a})} \\ &+ ib_2 F_{\mathrm{UV}} \langle\phi_{1a}|\hat{D}|\phi_{2a}\rangle \, e^{-i \int_{t_0}^{t} dt'(E_{2a}-E_{1a})} \end{aligned} \tag{4.10}$$

and

$$\begin{aligned} \dot{b}_2 = {}&ib_2 F_{\mathrm{UV}} \langle\phi_{2a}|\hat{D}|\phi_{2a}\rangle - b_1 \langle\phi_{2a}|\dot{\phi}_{1a}\rangle \, e^{-i \int_{t_0}^{t} dt'(E_{1a}-E_{2a})} \\ &+ ib_1 F_{\mathrm{UV}} \langle\phi_{2a}|\hat{D}|\phi_{1a}\rangle \, e^{-i \int_{t_0}^{t} dt'(E_{1a}-E_{2a})}, \end{aligned} \tag{4.11}$$

which can be solved numerically with initial values $b_1(t_0) = 1$ and $b_2(t_0) = 0$, to obtain $b_1(t)$ and $b_2(t)$.

In Eqs. (4.10) and (4.11) terms containing factors on the form $\langle\phi_{ka}|\dot{\phi}_{ka}\rangle$ have been neglected, which requires justification. One way to justify this is to first note that the normalized eigenstates from Eqs. (4.7) and (4.8) can be written as $|\phi_{ka}(t)\rangle = \alpha_{k1}(t) |\phi_1\rangle + \alpha_{k2}(t) |\phi_2\rangle$, with normalization implying $\alpha_{k1}^2 + \alpha_{k2}^2 = 1$. With this in mind, we see that

$$\langle\phi_{ka}|\dot{\phi}_{ka}\rangle = \alpha_{k1}\dot{\alpha}_{k1} + \alpha_{k2}\dot{\alpha}_{k2} = \frac{1}{2}\frac{d}{dt}\left(\alpha_{k1}^2 + \alpha_{k2}^2\right) = 0. \tag{4.12}$$

4.4.4 Dipole Moment

To calculate $\langle\Phi_a|\hat{D}|\Phi_a\rangle$, we start by noting that as a consequence of the weak- and moderately intense fields, and given that we start out in the ground state, $b_2(t)$ can be considered to be relatively small throughout the interaction, so that we can neglect $|b_2(t)|^2$ in the expression for the dipole moment; in this case the dipole moment can be written as

$$\langle D\rangle_a = |b_1|^2 \langle\phi_{1a}|\hat{D}|\phi_{1a}\rangle + 2\mathrm{Re}\left[b_1^* b_2 \langle\phi_{1a}|\hat{D}|\phi_{2a}\rangle \, e^{-i \int_{t_0}^{t} dt'(E_{2a}-E_{1a})}\right]. \tag{4.13}$$

With the expression in Eq. (4.13), the adiabatic model can be realized by numerically solving Eqs. (4.10) and (4.11), inserting the resolved quantities into Eq. (4.13), taking the Fourier transform to get the frequency resolved dipole moment, and inserting it into Eq. (2.7) along with the frequency resolved UV pulse.

The two features we seek to describe here are the LISs, which—as seen in Fig. 4.5—are appearing in atypical settings in the spectra corresponding to a polar molecule (as compared to the nonpolar case), and the ladder, a feature that was first described in the context of ATAS in Ref. [2]. Similarly to the case of the three features we described in Chapter 3, the LISs and ladder here stem from distinct parts of Eq. (4.13), and thus it is convenient to consider them independently.

4.5 Further Analysis of Features

In this section we analyze the LISs and ladder in detail, building on the fixed-nuclei adiabatic model of the previous section. This allows us to understand the features in greater detail, and even to derive a fully analytical expression corresponding to parts of the ladder feature that arise from adiabatic dynamics.

4.5.1 Light-induced Structures

The presence of LISs in the spectrum typically indicates—in systems with no permanent dipole—that a process involving two photons, in a transition from the ground state to a dark state, has taken place [52, 70]—something we have seen in Chapter 3. In these cases there is no signal in the spectrum at the location of the dark state, since—per definition—there exists no dipole coupling between the dark state and ground state. What was shown in Fig. 4.5 is that this is not the case when a nonzero permanent dipole is inherent in the system, as LISs surrounds the bright state at $E_2(R_0) = 7.07$ eV.

To improve our understanding of these unusual LISs, we start with the term responsible for the LISs in Eq. (4.13), and apply a number of approximation, with the goal of simplifying the expression corresponding to the LISs to the point where only essential components remain. We can then expect that an examination of these components will yield a more direct understanding of how the LISs arise.

As will become clear, the second term of Eq. (4.13) corresponds to the LISs, so that

$$\langle D \rangle_{a,\text{LIS}} = 2\text{Re}\left[b_1^* b_2 \langle \phi_{1a}|\hat{D}|\phi_{2a}\rangle\, e^{-i\int_{t_0}^{t} dt'(E_{2a}-E_{1a})}\right], \qquad (4.14)$$

and we start by considering the coefficients $b_1(t)$ and $b_2(t)$. The first assumption we make is that relative to its initial value $b_1(t_0) = 1$, any subsequent alteration of $b_1(t)$ will be small, so that we can set $b_1(t) \approx 1$.

Next, we consider the non-adiabatic term, $\langle \phi_{2a}|\dot{\phi}_{1a}\rangle$, from Eq. (4.11). For the omission of this term to be a valid approximation, the adiabatic condition must hold—the NIR field must evolve slowly in time relative to the dynamics of system. From the previous chapter we learned that Fourier transforms involving the field to the n'th order shifts the location of a feature in the spectrogram by $n\omega_{\text{NIR}}$, typically relative to an existing energy level. This suggests that the terms responsible for the LISs here involve the NIR field to first and second order. Increasing orders of the field involve increasingly rapid oscillations, which in turn makes the adiabatic condition less likely to hold. Since we here consider the NIR field up to second order only, we assume that the adiabatic condition holds, allowing us to neglect the $\langle \phi_{2a}|\dot{\phi}_{1a}\rangle$ term. The validity of this assumption will be confirmed in the ensuing analysis of the spectrogram calculated with the assumption in place.

The coefficients are not yet sufficiently simplified; to make further progress we posit that the NIR field dependent parts of Eq. (4.14) that are directly responsible for the LISs are present in the phase factor $\exp\left[-i\int_{t_0}^{t} dt'(E_{2a} - E_{1a})\right]$, and so we neglect F_{NIR}-dependent parts in the other factors. This amounts to setting

$$\langle \phi_{2a}|\hat{D}|\phi_{1a}\rangle \approx D_{12}, \qquad (4.15)$$

$$e^{-\int_{t_0}^{t} dt'(E_{1a}-E_{2a})} \approx e^{-i(t-t_0)(E_1 - E_2)}, \qquad (4.16)$$

in Eqs. (4.11) and (4.14).

The UV pulse intensity is weak, allowing us to treat the interaction between the system and the pulse perturbatively. We have already set $b_1(t) = 1$; in the zeroth order approximation we have no perturbation, and we have $b_2^{(0)}(t) = 0$, with the superscript indicating the order of approximation. To obtain the first order approximation, $b_2^{(1)}$, we insert $b_1(t) = 1$ and $b_2^{(0)} = 0$ into the remaining terms of Eq. (4.11), and integrate

from t_0, which yields

$$b_2^{(1)}(t) = iD_{12}W_N(t - \tau) \int_{t_0}^{t} dt' F_{\mathrm{UV}} e^{-i(t'-t_0)(E_1-E_2)}. \qquad (4.17)$$

In Eq. (4.17) we have multiplied by the window function $W_N(t - \tau)$, reproducing the cutoff of the dipole moment due to the dissociating wave packet, which is automatically included in the numerical model that contains the nuclear kinetic term, T_N, in the Hamiltonian. The dipole moment corresponding to the LISs has then been reduced to

$$\langle D \rangle_{a,\mathrm{LIS}} = 2D_{12}^2 W_N \, \mathrm{Re} \left[ie^{-i \int_{t_0}^{t} dt'(E_{2a}-E_{1a})} \int_{t_0}^{t} dt' F_{\mathrm{UV}} e^{-i(t'-t_0)(E_1-E_2)} \right]. \qquad (4.18)$$

The eigenvalues $E_{1a}(t)$ and $E_{2a}(t)$ are given in Eqs. (4.5) and (4.6). The next step of our derivation consists of factoring out the constant part of the integrand $(E_{2a} - E_{1a})$ in the exponent of the phase factor, and keeping only terms up to second order, $\mathcal{O}(F_{\mathrm{NIR}}^2)$, in the remainder:

$$e^{-i \int_{t_0}^{t} dt'(E_{2a}-E_{1a})} \approx e^{-i(t-t_0)(E_2-E_1)} e^{-i \int_{t_0}^{t} dt'(D_{11}-D_{22})F_{\mathrm{NIR}} + \frac{D_{12}^2}{E_2-E_1}F_{\mathrm{NIR}}^2}. \qquad (4.19)$$

The Taylor series of the second exponential factor is approximately

$$e^{-i \int_{t_0}^{t} dt'(D_{11}-D_{22})F_{\mathrm{NIR}} + \frac{D_{12}^2}{E_2-E_1}F_{\mathrm{NIR}}^2} \approx 1 - i(D_{11} - D_{22}) \int_{t_0}^{t} dt' F_{\mathrm{NIR}}$$

$$- \frac{1}{2}(D_{11} - D_{22})^2 \left(\int_{t_0}^{t} dt' F_{\mathrm{NIR}} \right)^2, \qquad (4.20)$$

where we have neglected all terms of third order of higher in the NIR field, in addition to a second order term, $-i\frac{D_{12}^2}{E_2-E_1} \int_{t_0}^{t} dt' F_{\mathrm{NIR}}^2$, as it is sufficiently small relative to the other second order term.

Finally then, the simplified model for the LISs is obtained by inserting Eq. (4.20) into Eq. (4.18), numerically obtaining the Fourier transform, $\tilde{D}_{a,\mathrm{LIS}}(\omega, \tau)$, and inserting into Eq. (2.7). The resulting spectrogram is shown in Fig. 4.7, and specifically in panel (b); the numerical results as described in Section 4.3 are shown in panel (a), for comparison. From this figure we can clearly see that the simplified model provides an accurate reproduction of the LISs and the main absorption line, including the which-way interference pattern. The ladder feature is not present in Fig. 4.7 (b)—as expected—since the term corresponding to the ladder is omitted from the present model.
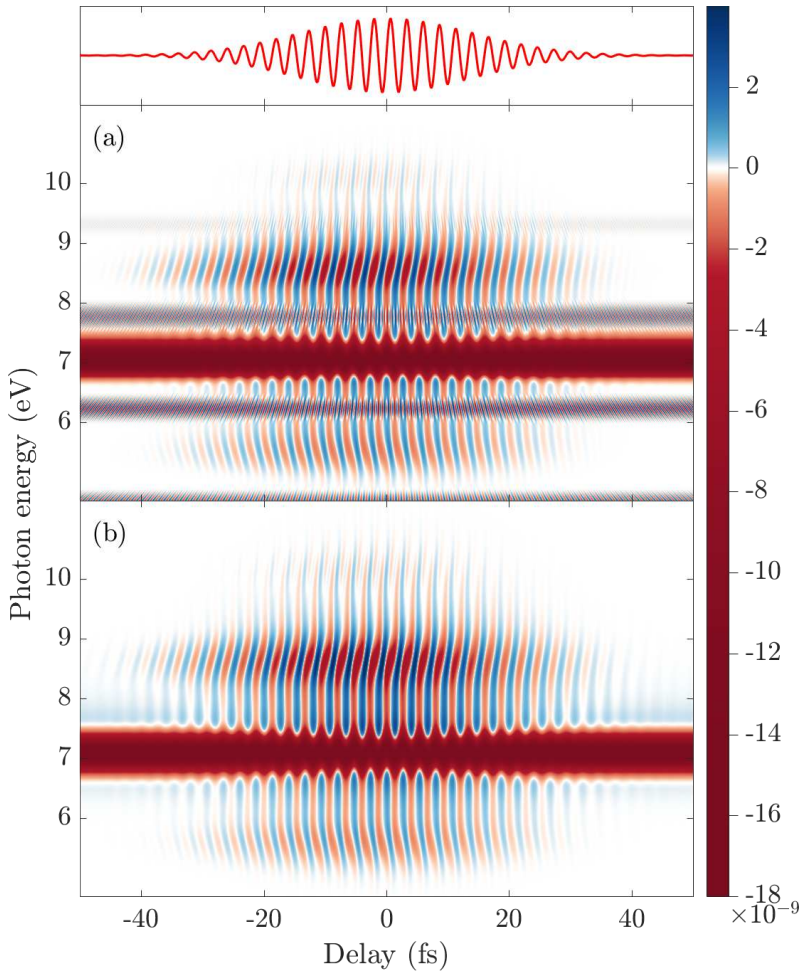
Figure 4.7: Numerically calculated attosecond transient absorption spectrum $\tilde{S}(\omega, \tau)$ [Eq. (2.7)], of LiF. Panel (a) exhibits the LISs as calculated by the full numerical method, described in Section 4.3. Panel (b) exhibits the LISs corresponding to the time-dependent dipole moment of Eq. (4.18), with phases from Eq. (4.20). Relevant parameters are given in Section 4.2. An illustration of the infrared pulse, centered at $\tau = 0$ fs, is shown in the top panel. The color scale to the right displays the signal strength in arbitrary units. Reproduced with permissions from Phys. Rev. A **98**, 053401 (2018) [2]. Copyright 2018 American Physical Society.

To better understand the properties and origin of the LISs here, we consider Eqs. (4.18) and (4.20), from which they arise. The first thing we note is that the simultaneous presence of a nonzero diagonal dipole matrix element, D_{12}, and nonzero off-diagonal dipole matrix elements, D_{11} and D_{22}, is required for the existence of the LISs. More specifically, $D_{12} \neq 0$ is required for the presence of any feature in the spectrogram at all, with the overall signal strength depending on the magnitude D_{12}^2. The main absorption line at $E_2(R_0) = 7.07$ eV will still be present in the absence of nonzero permanent dipoles, but the LISs will vanish; this corroborates what we learned from comparing Figures 4.4 and 4.5. The overall signal strength of the LISs is proportional to $D_{11} - D_{22}$ and $(D_{11} - D_{22})^2$ for the LISs located at energies $E_2 \pm \omega_{\mathrm{NIR}}$ and $E_2 + 2\omega_{\mathrm{NIR}}$, respectively.

The LISs here are mainly dependent on both the adiabatic phases, $\exp\left[-i \int_{t_0}^t dt'(E_{2a} - E_{1a})\right]$, and the adiabatic coefficient from Eq. (4.17). In the atomic system of Chapter 3, on the other hand, the LISs were found to originate in the term related to mixing of states, $\langle \psi_1 | \hat{d} | \psi_{a3} \rangle$, and an adiabatic coefficient, $a_3(t)$ (see Section 3.4.2). An important takeaway then, is that this difference in the origin of the LISs implies that it is incorrect to invariably attribute the LISs to the same factors across different systems.

4.5.2   Ladder

We now turn to the ladder feature seen in Fig. 4.5. The individual rungs of the ladder can be seen at energies $E_1(R_0) + n\omega_{\mathrm{NIR}}$ ($n \in \{1, 2, 3, 4, 5, 6\}$), as indicated by the green arrows, with the n'th rung of the ladder oscillating with the delay, τ, as $n\omega_{\mathrm{NIR}}$.

As we shall see in the following, we can derive a fully analytical expression that describes part of the ladder, and a simplified model corresponding to the remainder. In Fig. 4.8 several isolated views of the ladder feature are shown, with the results from the full adiabatic model defined in Section 4.4 in panel (a), results equivalent to the analytical expression in panel (b), and the simplified model results exhibited in panel (c). These will be discussed further later in this section.

The process of isolating the ladder feature from the other features in the spectrum requires some clarification. In ATAS, the UV pulse enters the calculations in two distinct ways. One, it is a constituent of the Hamiltonian, which determines the evolution of the coefficients (field-free or adiabatic) through the TDSE. And two, the frequency resolved pulse enters the expression for the response function directly [Eq. (2.7)]. The latter is indispensable, but the former can be neglected under certain circumstances,
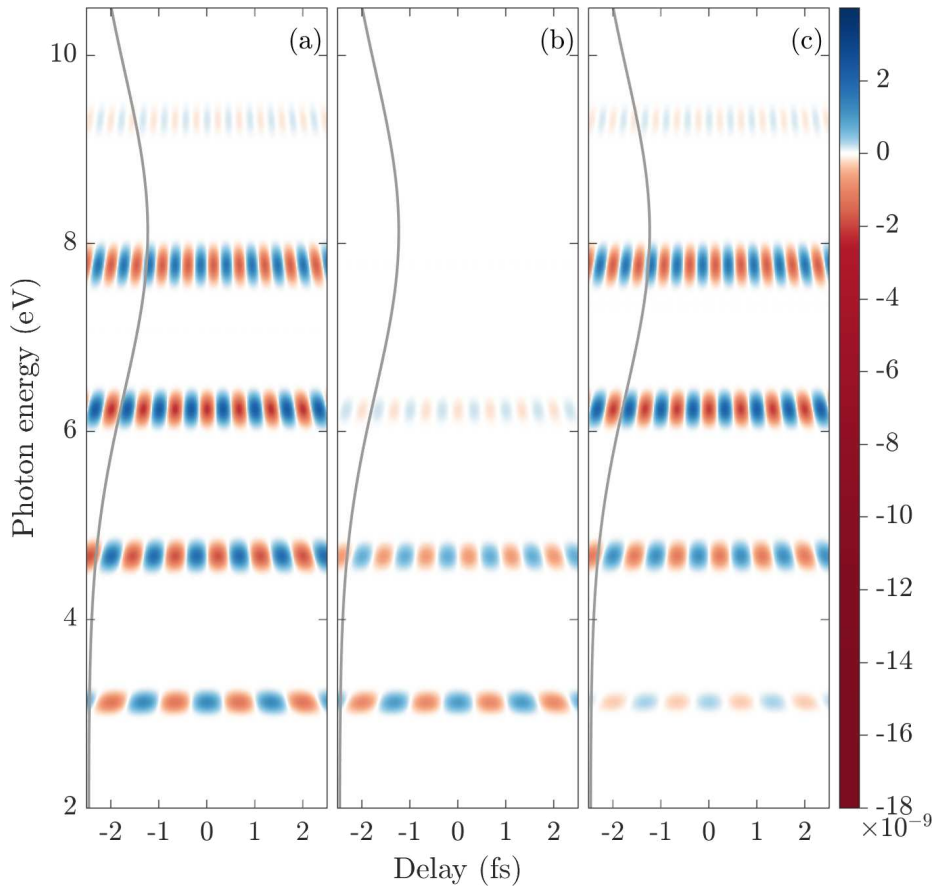
Figure 4.8: Numerically calculated attosecond transient absorption spectrum $\tilde{S}(\omega, \tau)$ of LiF, with an isolated view of the ladder feature realized by setting $F_{\mathrm{UV}} = 0$ everywhere except in the response function, Eq (2.7). In panel (a) the results of the full adiabatic model of Section 4.4 are shown. In panel (b) the results corresponding to the first term in Eq. (4.13) are shown, which is identical to the spectrum corresponding to the analytical expression in Eq. (4.24). In panel (c) the non-adiatic contribution to the ladder, stemming from the second term in Eq. (4.13) is shown. Relevant parameters are given in Section 4.2. Towards the left of each panel, the frequency bandwidth of the UV pulse is shown in gray. The color scale to the right displays the signal strength in arbitrary units. Adapted with permissions from Phys. Rev. A **98**, 053401 (2018) [2]. Copyright 2018 American Physical Society.

one of which is that the ground state curve must be sufficiently close to the first excited curve. We note that in a practical setting, it is of course problematic to omit the interaction between the UV pulse and the system, as it would require an experimental setup where the NIR pulse could interact with the system, and the subsequent radiation could interfere with an UV pulse which had *not* directly interacted with the system; in a theoretical setting, however, this is easily realized, and can be useful in order to get an unobstructed view of a certain feature of interest.

An indicator that the UV pulse is needed for the response function, but is not involved in the dynamics that create the ladder, is that even for very large negative or positive delays the ladder is present. The implication is that the ladder is not dependent on a persistent population induced by the UV pulse, as for these large delays the wave packets dissociate either long before, or is not *yet* present when the NIR pulse arrives. By leaving the UV pulse out of the TDSE, and obtaining the results of Fig. 4.8 (a)—in which the ladder appears to be an excellent reproduction of the numerically calculated results of Fig. 4.6 (b)—we confirm that this approach is valid.

The next step in the analysis of the ladder feature starts with a return to Eq. (4.13), where each of the two terms are partially responsible for the ladder. As before, we set $b_1(t) = 1$, and since we now have $F_{\mathrm{UV}} = 0$, we can write

$$\langle D \rangle_{a,\mathrm{lad}} = \langle \phi_{1a} | \hat{D} | \phi_{1a} \rangle + 2\mathrm{Re} \left[b_2 \langle \phi_{1a} | \hat{D} | \phi_{2a} \rangle \, e^{-i \int_{t_0}^{t} dt' (E_{2a} - E_{1a})} \right], \quad (4.21)$$

with

$$b_2(t) = - \int_{t_0}^{t} dt' \, \langle \phi_{2a} | \dot{\phi}_{1a} \rangle \, e^{-i \int_{t_0}^{t'} dt'' (E_{1a} - E_{2a})} \quad (4.22)$$

In the derivation of the LISs (see Section 4.5.1), we argued for the neglecting of a term containing the non-adiabatic factor $\langle \phi_{2a} | \dot{\phi}_{1a} \rangle$, on the grounds that the LISs only involved the NIR field up to second order, and so any time-dependent dynamics would be sufficiently slow to justify the discounting of non-adiabatic effects. The uppermost visible rung of the ladder is located at energy $E_1(R_0) + 6\omega_{\mathrm{NIR}}$, and thus we would expect factors of the NIR field up to sixth order to be involved; this in turn suggests that it would be unreasonable to disregard all non-adiabatic dynamics in their generation.

Of the two terms in Eq. (4.21) then, the first represents the adiabatic dynamics involved in the generation of the ladder, and its corresponding spectrogram is shown in Fig. 4.8 (b); the second term represents the non-adiabatic dynamics, and is shown in Fig. 4.8 (c). The figure clearly shows

that the non-adiabatic contribution to the full feature [Fig. 4.8 (a)], is greater than the adiabatic contribution.

In Section 4.5.1 we employed the strategy of isolating the most impactful factors in the expressions, in order to try to gain a better understanding of the LISs. In the generation of the parts of the ladder feature resulting from non-adiabatic dynamics, on the other hand, all the factors in Eq. (4.22) and in the second term of Eq. (4.21) play a role, and so none can be neglected. The implication is that the non-adiabatic parts of the ladder arise from a complicated interplay between the adiabatic coefficient $b_2(t)$, the adiabatic dipole coupling term $\langle \phi_{1a} | \hat{D} | \phi_{2a} \rangle$, and the field-induced phases $\exp\left[-i \int_{t_0}^t dt' (E_{2a} - E_{1a}) \right]$—under these circumstances, discerning the contribution from each individual factor is unrealistic.

We turn then, to the first term of Eq. (4.21), which represents the contribution to the ladder due to adiabatic dynamics, and specifically to the rungs at energies $E_1(R_0) + n\omega_{\text{NIR}}$ ($n \in \{2, 3, 4\}$), as we see in Fig. 4.8 (b). From this term, $\langle \phi_{1a} | \hat{D} | \phi_{1a} \rangle$, we can derive a fully analytical response function. The first step in the derivation is the Taylor expansion of $\langle \phi_{1a} | \hat{D} | \phi_{1a} \rangle$ about F_{NIR}, where we keep terms up to fourth order, $\mathcal{O}(F_{\text{NIR}}^4)$, in the NIR field—prompted by the location of the rungs in the spectrum, as they go up to energy $E_1(R_0) + 4\omega_{\text{NIR}}$. The coefficients in the Taylor expansion of $\langle \phi_{1a} | \hat{D} | \phi_{1a} \rangle$ consist in general of several terms, where the magnitude of one term dominates in each coefficient. By keeping only the dominant terms, the expansion can be shown to be

$$\langle \phi_{1a} | \hat{D} | \phi_{1a} \rangle \approx D_{12}^2 \sum_{n=2}^{4} (n+1) \frac{(D_{22} - D_{11})^{n-1}}{(E_2 - E_1)^n} F_{\text{NIR}}^n. \qquad (4.23)$$

To obtain the closed analytical form for the response function, we must now obtain the analytical expressions for the frequency resolved UV pulse, the derivation of which is relegated to Appendix B.1, and the expression for the Fourier transform of the time-dependent part of Eq. (4.23), i.e., the Fourier transform of $F_{\text{NIR}}^n(t)$ up to $n = 4$, which is derived in Appendix B.2. By inserting Eqs. (B.6) and (B.9) into the response function in Eq. (2.7),

we obtain the analytical expression

$$\tilde{S}_{\text{lad}}(\omega, \tau) = \frac{\pi \rho D_{12}^2 T_{\text{NIR}} T_{\text{UV}} F_{0,\text{UV}}}{4c} \frac{\omega^2}{\omega_{\text{UV}}} \exp\left[-\frac{T_{\text{UV}}^2}{16}(\omega - \omega_{\text{UV}})^2\right]$$

$$\times \sum_{n=2}^{4} (n+1) \frac{(D_{22} - D_{11})^{n-1}}{(E_2 - E_1)^n} \frac{F_{0,\text{NIR}}^n}{\sqrt{n}} \exp\left[-\frac{T_{\text{NIR}}^2}{16n}(\omega - n\omega_{\text{NIR}})^2\right]$$

$$\times \left(-\frac{1}{2}\right)^n \text{Im}\left\{i^{n+1} \exp(i\tau\omega) \exp[i(n-1)\varphi]\right\}. \tag{4.24}$$

The spectrum expressed in Eq. (4.24) exactly reproduces the spectrum seen in Fig. 4.8 (b), with $\varphi = 0$ [see Eq. (2.27)].

Having a fully analytical expression for the response function gives us direct access to the various dependencies of the relevant feature, and allows us to deduce the origin of all its characteristic properties—as was shown in Chapter 3. Encapsulated in Eq. (4.24) is the part of the spectrum which due to the adiabatic dynamics of the system. Under the present circumstances, the adiabatic dynamics contribute less to the ATAS spectrum than the non-adiabatic part, which can be seen by comparing Fig. 4.8 (b) with Fig. 4.8 (c). Certain characteristics of the ladder, such as the oscillation frequency with τ and the equidistant spacing of the rungs, seem to be preserved in the transition between the adiabatic and non-adiabatic contributions, which suggests that the analytical response function in Eq. (4.24) expresses some general facts about the ladder feature—not just the adiabatic parts. We also note that in a different system the balance between the contributions of the adiabatic and non-adiabatic dynamics could be shifted, e.g., if the NIR pulse has a lower frequency, giving the system more time to adapt to its influence.

The time-dependent dipole function from which $S_{\text{lad}}(\omega, \tau)$ is derived, is entirely determined by the $\langle \phi_{1a} | \hat{D} | \phi_{1a} \rangle$ term in Eq. (4.13), which corresponds to an NIR-field induced mixing of the field free states $|\phi_1\rangle$ and $|\phi_2\rangle$. All n-dependent terms—referring to the n'th rung of the ladder—in Eq. (4.24) stem from this mixing term; here we accentuate the most relevant ones. The $(E_2 - E_1)^{-n}$ factor in Eq. (4.24) exhibits the dependence of the n'th rung signal strength on the energy difference between the ground state and excited curves at $R = R_0$, specifically showing that a smaller energy difference translates into a stronger signal, an effect that is amplified with increasing n; one way to interpret this is that adjacency of the states controls the degree of mixing. A similar effect is caused by the $(D_{22} - D_{11})^{n-1}$ factor, where an increase in n or in the difference between

the two permanent dipoles yields an increase in the signal strength. The fact that the signal is dependent on the permanent dipoles is perhaps not surprising, as the ladder feature itself only arises in the presence of nonzero permanent dipoles in the first place. Furthermore, the $F_{0,\mathrm{NIR}}^n$ reflects the interpretation where the n'th rung is a signature of the dressing of the ground state by n NIR photons; for weak and moderate fields—which is a requirement for the validity of the present model—this factor strongly moderates the intensity of the signal with increasing n. The exponentials $\exp\left[-(T_{\mathrm{NIR}}^2/16n)(\omega - n\omega_{\mathrm{NIR}})^2\right]$ controls the location of the rungs in the spectrum, modulating the intensity of the signal as Gaussians centered at frequencies $\omega = n\omega_{\mathrm{NIR}}$.

The factor $\mathrm{Im}\left\{i^{n+1}\exp\left(i\tau\omega\right)\exp\left[i(n-1)\varphi\right]\right\}$ in Eq. (4.24) determines oscillation as a function of τ, and comes directly from the $\tilde{F}_{\mathrm{UV}}(\omega, \tau)$ factor in the definition of the response function, since the delay does not enter directly into the dipole moment in this calculation; the factor also contains the effects due to the phase φ of the incoming fields. The phase is set to zero here, but in the following section we will use it to investigate how the orientation or alignment of the target molecules affects the ATAS spectrum. We note that the exponential term $\exp\left[-T_{\mathrm{UV}}^2(\omega - \omega_{\mathrm{UV}})^2/16\right]$ picks out the frequencies that lie in the bandwidth of the UV pulse, which of course is a reflection of one of the defining properties of ATAS.

Finally, it should be noted, that the ladder feature observed in our spectra, and described by Eq. (4.24), is not equivalent to a type of ladder *climbing* described in several other studies [113–115]. In a molecular system, it is possible to express the nuclear wave functions as linear combinations of the vibrational states of the PECs. In ladder climbing, the idea is to 'climb' up the vibrational state manifold by populating consecutive states by applying a field with a frequency which is comparable to the spacing between the energies of the vibrational states, i.e., resonant transitions. In our case the distance between each rung of the ladder is equivalent to a number of vibrational state energies, and by resolving the nuclear wave packets in vibrational states we could not see signs of ladder climbing in the populations of the states. We do not explicitly describe the method of expanding the wave function in vibrational states here, as it serves a minor role in the work—for such a description we suggest Ref. [82].

Polar Versus Non-polar Molecules

The response function in Eq. (4.24) (corresponding to the ladder) and the phases in Eq. (4.20) (corresponding to the LISs) reveal that the difference

between the diagonal dipole elements corresponding to the two curves, D_{11} and D_{22}, is the essential component of the features that is related to the polarity of the molecule. In a heteronuclear molecule, the nuclear mass asymmetry results in a nonzero total permanent dipole. However, some heteronuclear systems, e.g., HD^+ and HD, have electronic states that are parity eigenstates, so that we would have $D_{11} = D_{22}$, and in this case the present analysis suggests that the features would not be present in the spectrum. Having a heteronuclear molecule is therefore not a sufficient condition for the ladder or LISs to arise; it is necessary to specifically consider polar molecules.

4.6   Orientation and Alignment

In the calculations up until this point, we have assumed that the molecular targets have a specific orientation with respect to the incoming field, as shown in the illustration in Fig. 4.2. Another common target setup is one in which the molecules are *aligned* with respect to the incoming field; in this case each molecule in the target has one out of two opposite orientations. For our system, this would imply that half the molecules are in the orientation shown in Fig. 4.2, and the other half with interchanged nuclei. Orientation and alignment both constitute experimentally feasible setups of the target, with alignment [116] typically being more simple to attain than orientation [117–120]. In this section we investigate how the setup of the target affects the ATAS spectrum.

Having already considered spectra corresponding to oriented molecular targets, we now consider alignment. We start by recognizing that if we impose a phase $\varphi = \pi$ on the incoming fields, it will be equivalent to flipping the orientation of the system. By simply adding the contributions from two calculations, one with $\varphi = 0$ and one with $\varphi = \pi$, i.e.,

$$S_{\text{aligned}}(\omega, \tau) = \frac{1}{2} \left[S(\omega, \tau; \varphi = 0) + S(\omega, \tau; \varphi = \pi) \right], \qquad (4.25)$$

we get the ATAS spectrum we would expect from a target consisting of aligned molecules. This coherent addition is justified by the fact that the dipole moment represents the response of the system, and it appears as a linear factor in Eq. (2.7).

The comparison of spectra corresponding to oriented and aligned targets is shown in Fig. 4.9, in panels (a) and (b), respectively. The spectra were calculated using the numerical approach described in Chapter 2. All the major features of the spectrum, highlighted in Fig. 4.5, exhibit changes

when going from an oriented to an aligned target. Specifically, the LISs are notably suppressed, the which-way interference on the absorption line vanishes, and all rungs in the ladder feature whose location in the spectrum correspond to an even number of photon energies relative to the ground state energy disappear.

That which-way interference—arising due to several pathways sharing a final destination—disappears with the LISs, is at first glance unsurprising, as the LISs are signatures of processes where several photons are absorbed/emitted in order to reach the excited curve. When these channels close, only the absorption of a single UV photon remains as a path to the excited curve, and interference between distinct paths is no longer possible. This implied causality is, however, misleading. There is no conspicuous argument here for why the processes taking place in each individual molecule in the target would change as a function of the collective arrangement of the molecules, especially considering that the single-system assumption means that macroscopic propagation effects are disregarded (see Section 2.1). Instead, the LISs and which-way interference are likely extinguished due to contributions carrying opposite signs in the two terms in Eq. (4.25), i.e., destructive interference.

The analytical expression in Eq. (4.24) allows us to make the preceding argument explicit for the ladder feature—under the presumption that our reasoning can be extended to the non-adiabatic part. Considering the exponential factor in Eq. (4.24) that contains the CEP, we see that for $\varphi = 0$ we have $\exp\left[i(n-1)\varphi\right] = 1$, whereas for $\varphi = \pi$ we have $\exp\left[i(n-1)\varphi\right] = (-1)^{n-1}$, which means that for even n, the two terms in Eq. (4.25) will have opposite signs, and cancel each other out.

The way the molecules in the target are arranged then, have a significant impact on the ATAS response signal. The results here suggests that an arrangement of oriented molecules is favorable, as alignment leads to the obscuring of certain features in the spectrum, and not due to a change in the processes taking place in the individual molecules. With oriented molecules, all relevant processes taking place leave signatures in the spectrum.
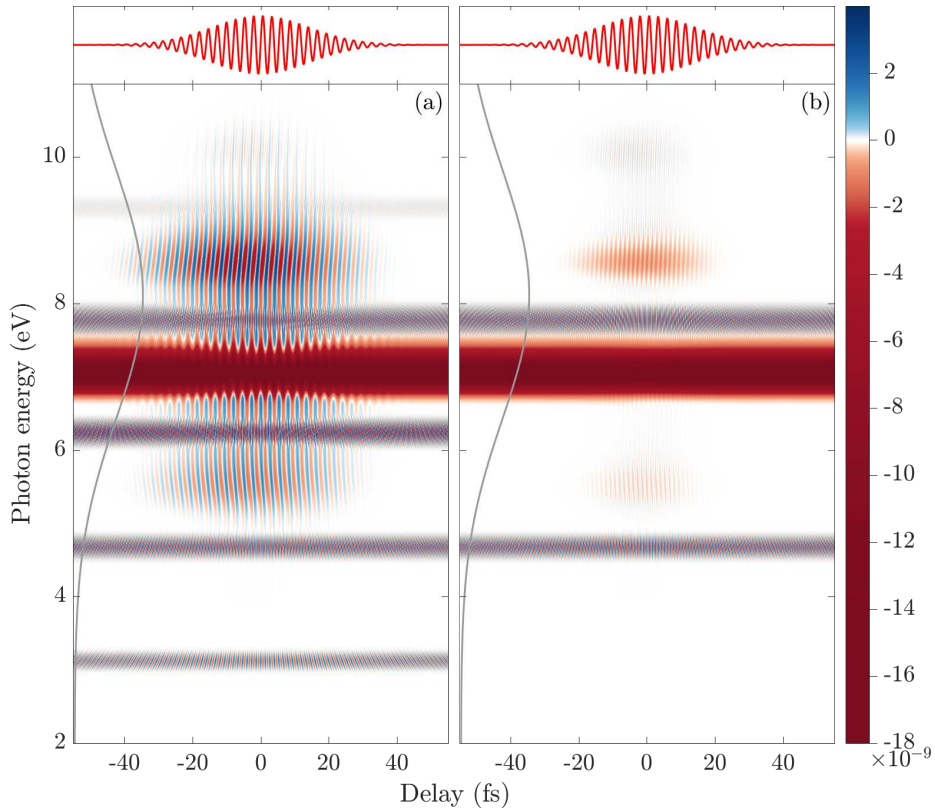
Figure 4.9: Numerically calculated attosecond transient absorption spectrum $\tilde{S}(\omega, \tau)$ [Eq. (2.7)], of LiF. In the calculation of the results in panel (a), the carrier-envelope phase φ of the incoming fields was set to zero, corresponding to a target of molecules oriented with respect to the field. In panel (b) the spectrum from Eq. (4.25) is shown, corresponding to a target of molecules aligned with respesct to the field. Towards the left of each panel, the frequency bandwidth of the UV pulse is shown in gray. The color scale to the right displays the signal strength in arbitrary units. Reproduced with permissions from Phys. Rev. A **98**, 053401 (2018) [2]. Copyright 2018 American Physical Society.

Chapter 5

Summary and Outlook

The main goal of this thesis has been to provide a comprehensive description of the spectroscopic features that appear in atomic and molecular ATAS spectra. In the method of ATAS, any information must come directly from the spectrogram, and it is precisely the collection of these features that constitute the spectrogram. Therefore, the features have been the subject of several studies, both directly and indirectly, and various interpretations exist for each of them—see Chapter 1 for an overview. In this thesis we have tried to take the analysis of the features further, starting with relatively simple systems (based on He and LiF) that contain the necessary ingredients to produce the relevant spectroscopic signatures. Under assumptions of adiabatic behavior in the system with respect to the incoming infrared pulse, we have been able to obtain analytic expressions that give direct access to characteristics of certain features, and an understanding of their origin within the context of the models we used. Furthermore, as we were exploring the uncharted territory of dynamics in polar molecules with ATAS, we found familiar features showing up in unfamiliar settings, and a new, unexplored feature which—in light of its appearance—was dubbed a 'ladder'.

After a general introduction to the field of light-matter interaction, and specifically to ATAS, in Chapter 1, we started in Chapter 2 with a description of the theoretical underpinning of our investigations. Excellent and elaborate sources exist on many of the topics covered in the chapter, and we sought to avoid unnecessary repetition. After the general derivation of the most important equations in ATAS, we covered the components that must be calculated to obtain the ATAS spectrogram for a given system. This included the description of dynamics and dipole moments in atomic

and molecular systems. Finally, we looked at implementation of numerical methods, such as propagation schemes and absorption potentials.

Chapter 3 was dedicated to the description of the most common features in the ATAS of atomic systems, many of which extend to molecular systems. After starting off with briefly introducing some of these features, we started laying the groundwork for our model, by using fully numerical methods to ensure the validity of including only three atomic levels in a model. This was achieved by comparing a range of energies in the spectrogram calculated using either the three or twenty lowest levels of He, and verifying that including more levels beyond three would not affect the spectrum in a meaningful way. Having confirmed this, we went on to establish an adiabatic model, from which we could derive fully analytical expressions corresponding to three features that are ubiquitous in ATAS: light-induced structures, hyperbolic sidebands, and oscillating fringes. Not only did these expressions allow us to understand exactly how the properties of the system and fields affect the characteristics of the features, but we were also able to show that in the context of our model, the sidebands and fringes shared common origins—a unification not pointed out previously, as the features were understood to stem from distinct processes. Finally, we considered some of the important features in ATAS that could not be accommodated in our model, due to the condition of adiabaticity.

In Chapter 4 we turned our attention to molecules, and in particular to a certain class of molecules that so far has received little attention—polar molecules. We considered what to expect in molecular ATAS as compared to atomic ATAS, as nuclear dynamics comes into play, and orientation with respect to the field and permanent dipoles must be considered. As we investigated the polar LiF molecule, specifically considering the two lowest energy curves, the numerically obtained ATAS spectra exhibited several interesting features; in particular LISs appearing around a bright state and a number of equally spaced features reminiscent of a ladder—both of which were unanticipated and intriguing. In similar fashion to what we did in Chapter 3, we then pursued a model based on field-mixed adiabatic states, to complement the numerical results. From this model we were able to extract expressions that elucidated exactly the role of the permanent dipoles in the creation of the LISs and ladder, and allowed us derive a fully analytical expression corresponding to the part of the ladder arising due to adiabatic dynamics. In the end of Chapter 4, we also looked at how the arrangement of the molecules in the target would affect the spectroscopic outcome, and found that a setup where each molecule is oriented in a specific direction with respect to the field yields the most comprehensive

spectra.

There exists several promising and compelling directions for further ATAS research, and the contents of this thesis are not exhaustive in terms of ideas that I think would have been interesting to consider in greater detail. In the shaded area of Fig. 4.3 the two PECs nearly intersect; this is known as an avoided crossing, and here the non-adiabatic terms of Eq. (2.36) cannot be neglected. In the specific LiF system we considered the location of this avoided crossing meant that it could not influence the ATAS results. In other systems, however, it can be important, in which case ATAS is a great candidate for a tool with which we explore the non-adiabatic dynamics. This is an area of active research of my colleague, PhD student Nikolaj S. W. Ravn, who is considering model systems involving avoided crossing. Non-adiabatic couplings can pose a problem to the numerical algorithms, due to their sharply varying shape; one promising way to tackle this challenge is to change the basis of the wave packets to the so-called diabatic basis, where the problematic terms are more amenable.

Another promising avenue of ATAS research is the study of more complicated system, such as molecules with more than two nuclei or solid state systems. As mentioned in Chapter 1, certain studies have been conducted using ATAS on molecules with more than two nuclei [55], on dielectrics [60, 61], and on semiconductors [56–59]; however, given the complexity of these systems, there are many situations that are open to exploration, and the dynamics due to, e.g., more complicated nuclear motion could make these systems interesting subjects for ATAS.

Fourier Transforms − Atoms

In this Appendix, we show how to derive certain Fourier transforms that are required to obtain the analytical expressions in Chapter 3. This Appendix is adapted from Ref. [1].

A.1 Sidebands and Fringes

In this section, we carry out the Fourier transform of the time-dependent parts of the dipole moment Eq. (3.23), which correspond to the SBs and fringes in the ATAS spectrum. We split the mentioned time-dependents parts into two new function $g(t)$ and $h(t)$, and keep only the time-dependent parts of each of these functions:

$$g(t) = F_{\mathrm{IR}}^2(t), \tag{A.1}$$

$$h(t) = \int_\tau^t dt' F_{\mathrm{IR}}^2(t') \tag{A.2}$$

Our task then, is to obtain the Fourier transform of each of the functions in Eqs. (A.1) and (A.2), under the following convention for the Fourier transform

$$\mathcal{F}[f(t)](\omega) = \frac{1}{\sqrt{2\pi}} \int_{-\infty}^{\infty} dt\, f(t) e^{-i\omega t}. \tag{A.3}$$

A factor $e^{iE_2 t}$ has been omitted in both functions $g(t)$ and $h(t)$. This factor implies a shift in frequency when taking the Fourier transform, as expressed by the relation

$$\mathcal{F}[e^{ibt} f(t)](\omega) = \tilde{f}(\omega - b), \tag{A.4}$$

which can be taken into consideration later.

The expression for the field $F_{IR}(t)$ is obtained via the vector potential in Eq (2.27), according to $F_{IR} = \frac{\partial}{\partial t} A_{IR}(t)$, so that

$$F_{IR}(t) = \frac{A_{0,IR} 8t}{T_{IR}^2} \exp\left(-\frac{4t^2}{T_{IR}^2}\right) \cos\left(\omega_{IR} t\right) + F_{0,IR} \exp\left(-\frac{4t^2}{T_{IR}^2}\right) \sin\left(\omega_{IR} t\right),$$

(A.5)

where we have used $t_c = 0$, as the IR field center is always fixed at time zero. Given the relatively long period T_{IR}, the term in Eq. (A.5) containing the factor T_{IR}^{-2} can be neglected, so that

$$F_{IR}(t) \approx F_{0,IR} \exp\left(-\frac{4t^2}{T_{IR}^2}\right) \sin\left(\omega_{IR} t\right), \qquad (A.6)$$

where the exponential is the envelope factor and the sine the carrier factor of the pulse.

Starting with Eq. (A.1), we have

$$\mathcal{F}[F_{IR}^2(t)](\omega) = \tilde{g}(\omega) = \frac{F_{0,IR}^2}{\sqrt{2\pi}} \int_{-\infty}^{\infty} dt \, \exp\left(-\frac{8t^2}{T_{IR}^2}\right) \sin^2\left(\omega_{IR} t\right) e^{-i\omega t},$$

(A.7)

where the sine can be expressed as exponentials, so that

$$\tilde{g}(\omega) = -\frac{F_{0,IR}}{4\sqrt{2\pi}} \Bigg[\int_{-\infty}^{\infty} dt \, e^{-8T_{IR}^{-2} t^2 + i\omega t + 2i\omega_{IR} t} \qquad (A.8)$$

$$+ \int_{-\infty}^{\infty} dt \, e^{-8T_{IR}^{-2} t^2 + i\omega t - 2i\omega_{IR} t} - 2 \int_{-\infty}^{\infty} dt \, e^{-8T_{IR}^{-2} t^2 + i\omega t} \Bigg].$$

The integrals in Eq. (A.8) can be solved by completing the square in the exponents, substituting variables, and taking the Gaussian integral

$$\int_{-\infty}^{\infty} dy \, e^{-y^2} = \sqrt{\pi}. \qquad (A.9)$$

By incorporating the frequency shift due to the factor $e^{iE_2 t}$ [see Eq. (A.4)], we finally obtain

$$\mathcal{F}[e^{iE_2 t} g(t)](\omega) = -\frac{F_{0,IR}^2 T_{IR}}{16} \Bigg[\exp\left(-\frac{T_{IR}^2 (\omega - E_2 - 2\omega_{IR})^2}{32}\right)$$

$$+ \exp\left(-\frac{T_{IR}^2 (\omega - E_2 + 2\omega_{IR})^2}{32}\right) \qquad (A.10)$$

$$- 2 \exp\left(-\frac{T_{IR}^2 (\omega - E_2)^2}{32}\right) \Bigg].$$

Turning to Eq. (A.2), the integral can be split up as

$$\int_\tau^t dt'\, F_{\mathrm{IR}}^2(t') = \int_0^t dt'\, F_{\mathrm{IR}}^2(t') + \int_\tau^0 dt'\, F_{\mathrm{IR}}^2(t'), \qquad (A.11)$$

where the second integral on the right-hand side will be constant in t when evaluated. In the text following Eq. (3.19) we noted that such terms would only be relevant for a the standard absorption line feature, which we are not considering here, and thus we drop this term. We note that this splitting of the integral could in principle have been carried out before the expansion in Eq. (3.21), but that would impede the analytical derivation, as we would be retaining an untractable integral.

With an even integrand in the remaining integral (first term) of Eq. (A.11), we can further alter the expression as

$$\begin{aligned}
\int_0^t dt'\, F_{\mathrm{IR}}^2(t') &= \frac{1}{2}\int_{-t}^t dt'\, F_{\mathrm{IR}}^2(t') \\
&= \frac{1}{2}\left[\int_{-\infty}^{-t} dt'\, F_{\mathrm{IR}}^2(t') + \int_{-t}^t dt'\, F_{\mathrm{IR}}^2(t') - \int_t^\infty dt'\, F_{\mathrm{IR}}^2(t')\right] \\
&= \frac{1}{2}\int_{-\infty}^\infty dt'\, \mathrm{sgn}(t-t')F_{\mathrm{IR}}^2(t'),
\end{aligned}$$

$$(A.12)$$

with $\mathrm{sgn}(t)$ the sign function. A convolution of two functions $u(t)$ and $v(t)$ is defined as

$$(u * v)(t) \equiv \int_{-\infty}^\infty dt'\, u(t-t')v(t'). \qquad (A.13)$$

The last term on the right-hand side of Eq. (A.12) satisfies the definition of a convolution, with $u(t) = \mathrm{sgn}(t)$ and $v(t) = F_{\mathrm{IR}}^2(t)$. The convolution theorem [121] states that

$$\mathcal{F}[(u * v)(t)](\omega) = \sqrt{2\pi}\mathcal{F}[u(t)](\omega)\mathcal{F}[v(t)](\omega), \qquad (A.14)$$

which reduces the problem to obtaining the individual Fourier transforms of $\mathrm{sgn}(t)$ and $F_{\mathrm{IR}}^2(t)$. The latter was obtained previously, and is given in Eq. (A.10), with the phase factor $e^{iE_2 t}$ incorporated. The former is given by [122]

$$\mathcal{F}[\mathrm{sgn}(t)](\omega) = -\sqrt{\frac{2}{\pi}}\frac{i}{\omega}, \qquad (A.15)$$

and we can obtain

$$
\begin{aligned}
\mathcal{F}[e^{iE_2 t} h(t)](\omega) = {} & i \frac{F_{0,\mathrm{IR}}^2 T_{\mathrm{IR}}}{16(\omega - E_2)} \left[\exp\left(-\frac{T_{\mathrm{IR}}^2 (\omega - E_2 - 2\omega_{\mathrm{IR}})^2}{32} \right) \right. \\
& + \exp\left(-\frac{T_{\mathrm{IR}}^2 (\omega - E_2 + 2\omega_{\mathrm{IR}})^2}{32} \right) \\
& \left. - 2\exp\left(-\frac{T_{\mathrm{IR}}^2 (\omega - E_2)^2}{32} \right) \right].
\end{aligned}
\tag{A.16}
$$

A.2   Light-induced Structures

In this section we perform the Fourier transform [see Eq. (A.3) for convention] of the time-dependent parts of Eq. (3.27), corresponding to the LISs in the ATAS spectrum. We have then

$$
\begin{aligned}
p(t) &= e^{iE_3 t} F_{\mathrm{IR}}(t) \\
&\approx e^{iE_3 t} F_{0,\mathrm{IR}} \exp\left(-\frac{4t^2}{T_{\mathrm{IR}}^2} \right) \sin\left(\omega_{\mathrm{IR}} t \right),
\end{aligned}
\tag{A.17}
$$

where the approximation is identical to the one made in Eq. (A.6). The frequency shift due to the factor $\exp\left(iE_3 t \right)$ [see Eq. (A.4)] can be taken into account in the end. As in the prior section, we express the sine in Eq. (A.17) in terms of exponentials, complete the square in the exponents, and evaluate the integrals, yielding

$$
\begin{aligned}
\mathcal{F}[p(t)](\omega) = {} & -i \frac{F_{0,\mathrm{IR}} T_{\mathrm{IR}}}{4\sqrt{2\pi}} \left\{ \exp\left[-\frac{T_{\mathrm{IR}}^2 (\omega - E_3 - \omega_{\mathrm{IR}})^2}{16} \right] \right. \\
& \left. + \exp\left[-\frac{T_{\mathrm{IR}}^2 (\omega - E_3 + \omega_{\mathrm{IR}})^2}{16} \right] \right\}.
\end{aligned}
\tag{A.18}
$$

Fourier Transforms – Molecules

In this Appendix, we show how to derive certain Fourier transforms that are required to obtain the analytical expressions for the adiabatic part of the ladder feature in Chapter 4. This Appendix is adapted from Ref. [2].

B.1   UV Pulse

In this section, we derive the Fourier transform of the time-dependent UV pulse, $F_{\mathrm{UV}}(t, \tau)$, in order to obtain the frequency resolved UV pulse, $\tilde{F}_{\mathrm{UV}}(\omega, \tau)$. This is a necessary component in the derivation of the fully analytical form describing the ladder feature in Section 4.5.2—see Eq. (4.24).

Starting with the vector potential in Eq. (2.27), we define $t' = t - t_c$, and obtain

$$
\begin{aligned}
F_{\mathrm{UV}}(t') &= \frac{8F_{0,\mathrm{UV}}}{\omega_{\mathrm{UV}} T_{\mathrm{UV}}^2} t' e^{-\frac{4t'^2}{T_{\mathrm{UV}}^2}} \cos\left(\omega_{\mathrm{UV}} t' + \varphi\right) + F_{0,\mathrm{UV}} e^{-\frac{4t'^2}{T_{\mathrm{UV}}^2}} \sin\left(\omega_{\mathrm{UV}} t' + \varphi\right) \\
&= \frac{4F_{0,\mathrm{UV}}}{\omega_{\mathrm{UV}} T_{\mathrm{UV}}^2} t' e^{-\frac{4t'^2}{T_{\mathrm{UV}}^2}} e^{i\omega_{\mathrm{UV}} t'} e^{i\varphi} + \frac{F_{0,\mathrm{UV}}}{2i} e^{-\frac{4t'^2}{T_{\mathrm{UV}}^2}} e^{i\omega_{\mathrm{UV}} t'} e^{i\varphi},
\end{aligned} \qquad \text{(B.1)}
$$

where terms containing factors $\exp\left(-i\omega_{\mathrm{UV}} t'\right)$ have been neglected, as they correspond to shifts to negative frequencies, and we consider only positive frequencies.

In order to proceed with the Fourier transform of Eq. (B.1), we first list a number of pertinent relations [122]. Adhering to the convention in

Eq. (A.3), we have

$$\mathcal{F}[e^{-\beta t^2}] = \frac{1}{\sqrt{2\beta}}e^{-\frac{\omega^2}{4\beta}} \tag{B.2}$$

$$\mathcal{F}[tf(t)] = i\frac{d\tilde{f}(\omega)}{d\omega} \tag{B.3}$$

$$\mathcal{F}[e^{ibt}f(t)] = \tilde{f}(\omega - b) \tag{B.4}$$

$$\mathcal{F}[f(t - \tau)] = e^{-i\tau\omega}\hat{f}(\omega). \tag{B.5}$$

Each of the relations of Eqs. (B.2)–(B.5) are then applied in the Fourier transform of Eq. (B.1), yielding the final expression for the frequency resolved UV pulse:

$$\tilde{F}_{\mathrm{UV}}(\omega, \tau) = -i\frac{F_{0,\mathrm{UV}}T_{\mathrm{UV}}}{4\sqrt{2}}\frac{\omega}{\omega_{\mathrm{UV}}}e^{-i\tau\omega}e^{i\varphi}e^{-\frac{T_{\mathrm{UV}}^2}{16}(\omega - \omega_{\mathrm{UV}})^2}. \tag{B.6}$$

B.2   NIR Pulse – *n*'th Order

In this section, we derive analytical expressions for the Fourier transform of the NIR field to the *n*'th power, with $n \in \{2, 3, 4\}$, which is used in the derivation of the analytical response function in Eq. (4.24). Note that Appendix A.1 contains a special case of this derivation, where $n = 2$. We overlook this redundancy, however, as we find the current structure to be better in terms of the readability of the thesis.

Starting from the vector potential in Eq. (2.27), and pointing out that the NIR pulse is centered at $t_c = 0$, we note that the NIR pulse period, T_{NIR}, is relatively long, and so we neglect the term containing the factor T_{NIR}^{-2}. The *n*'th power of the NIR field can then be expressed as

$$F_{\mathrm{NIR}}^n = F_{0,\mathrm{NIR}}^n e^{-\frac{4nt^2}{T_{\mathrm{NIR}}^2}}\sin^n(\omega_{\mathrm{NIR}}t + \varphi) \tag{B.7}$$

$$= F_{0,\mathrm{NIR}}^n e^{-\frac{4nt^2}{T_{\mathrm{NIR}}^2}}\frac{1}{(2i)^n}\left(e^{i\omega_{\mathrm{NIR}}t}e^{i\varphi} - e^{-i\omega_{\mathrm{NIR}}t}e^{-i\varphi}\right)^n.$$

Relying on the relations given in Eqs. (B.2)-(B.5), we can obtain the Fourier transform of the exponential term corresponding to the envelope of the pulse, $\exp\left(-4nt^2/T_{\mathrm{NIR}}^2\right)$. When calculating the expansion of the factor $[\exp\left(i\omega_{\mathrm{NIR}}t\right) - \exp\left(-i\omega_{\mathrm{NIR}}t\right)]^n$, we keep in mind that factors on the form $\exp\left(ibt\right)$ cause shifts in frequency [see Eq. (B.4)], with $b > 0$ implying shifts to positive frequencies; since only positive frequencies are relevant,

we neglect terms where $b < 0$. In light of this, and given the constraint that $n \in \{2, 3, 4\}$, the following general expression holds

$$F_{\mathrm{NIR}}^n = F_{0,\mathrm{NIR}}^n e^{-\frac{4nt^2}{T_{\mathrm{NIR}}^2}} \frac{1}{(2i)^n} e^{in\omega_{\mathrm{NIR}}t} e^{in\varphi}, \tag{B.8}$$

where, when $n = 4$, the expression omits a term of second order in the field, on the grounds that its coefficient is relatively small compared to the second order term from Eq. (B.8) with $n = 2$, which will dominate in the sum from Eq. (4.23).

Finally then, Fourier transforming Eq. (B.8) yields

$$\mathcal{F}\left[F_{\mathrm{NIR}}^n\right] = \left(-\frac{i}{2}\right)^n F_{0,\mathrm{NIR}}^n \frac{T_{\mathrm{NIR}}}{2\sqrt{2n}} e^{in\varphi} e^{-\frac{T_{\mathrm{NIR}}^2}{16n}(\omega - n\omega_{\mathrm{NIR}})^2}. \tag{B.9}$$

Bibliography

[1] J. J. Rørstad, J. E. Bækhøj, and L. B. Madsen, Analytic modeling of structures in attosecond transient-absorption spectra, Physical Review A **96**, 013430 (2017).

[2] J. J. Rørstad, N. S. W. Ravn, L. Yue, and L. B. Madsen, Attosecond transient-absorption spectroscopy of polar molecules, Phys. Rev. A **98**, 053401 (2018).

[3] M. Chovancova, H. Agueny, J. J. Rørstad, and J. P. Hansen, Classical and quantum-mechanical scaling of ionization from excited hydrogen atoms in single-cycle THz pulses, Phys. Rev. A **96**, 023423 (2017).

[4] A. L. Schawlow and C. H. Townes, Infrared and optical masers, Phys. Rev. **112**, 1940 (1958).

[5] T. H. Maiman, Stimulated optical radiation in ruby, Nature **187**, 493 (1960).

[6] P. B. Corkum and F. Krausz, Attosecond science, Nature Physics **3**, 381 (2007).

[7] F. Krausz and M. Ivanov, Attosecond physics, Rev. Mod. Phys. **81**, 163 (2009).

[8] F. Calegari, G. Sansone, S. Stagira, C. Vozzi, and M. Nisoli, Advances in attosecond science, J. Phys. B **49**, 062001 (2016).

[9] S. Bengtsson, E. W. Larsen, D. Kroon, S. Camp, M. Miranda, C. L. Arnold, A. L'Huillier, K. J. Schafer, M. B. Gaarde, L. Rippe, et al., Space–time control of free induction decay in the extreme ultraviolet, Nature Photonics **11**, 252 (2017).

[10]   M. Hentschel, R. Kienberger, C. Spielmann, G. A. Reider, N. Milo-
       sevic, T. Brabec, P. Corkum, U. Heinzmann, M. Drescher, and
       F. Krausz, Attosecond metrology, Nature **414**, 509 (2001).

[11]   A. McPherson, G. Gibson, H. Jara, U. Johann, T. S. Luk, I. A.
       McIntyre, K. Boyer, and C. K. Rhodes, Studies of multiphoton
       production of vacuum-ultraviolet radiation in the rare gases, J. Opt.
       Soc. Am. B **4**, 595 (1987).

[12]   M. Ferray, A. L'Huillier, X. F. Li, L. A. Lompre, G. Mainfray, and
       C. Manus, Multiple-harmonic conversion of 1064 nm radiation in
       rare gases, J. Phys. B **21**, L31 (1988).

[13]   J. J. Macklin, J. D. Kmetec, and C. L. Gordon, High-order harmonic
       generation using intense femtosecond pulses, Phys. Rev. Lett. **70**,
       766 (1993).

[14]   A. L'Huillier and P. Balcou, High-order harmonic generation in rare
       gases with a 1-ps 1053-nm laser, Phys. Rev. Lett. **70**, 774 (1993).

[15]   P. M. Kraus, M. Zürch, S. K. Cushing, D. M. Neumark, and S. R.
       Leone, The ultrafast X-ray spectroscopic revolution in chemical
       dynamics, Nature Reviews Chemistry **2**, 82 (2018).

[16]   M. Drescher, M. Hentschel, R. Kienberger, G. Tempea, C. Spielmann,
       G. A. Reider, P. B. Corkum, and F. Krausz, X-ray pulses approaching
       the attosecond frontier, Science **291**, 1923 (2001).

[17]   J. Itatani, F. Quéré, G. L. Yudin, M. Y. Ivanov, F. Krausz, and P. B.
       Corkum, Attosecond streak camera, Phys. Rev. Lett. **88**, 173903
       (2002).

[18]   A. Baltuška, T. Udem, M. Uiberacker, M. Hentschel, E. Goulielmakis,
       C. Gohle, R. Holzwarth, V. S. Yakovlev, A. Scrinzi, T. W. Hänsch,
       et al., Attosecond control of electronic processes by intense light
       fields, Nature **421**, 611 (2003).

[19]   E. Goulielmakis, V. S. Yakovlev, A. L. Cavalieri, M. Uiberacker,
       V. Pervak, A. Apolonski, R. Kienberger, U. Kleineberg, and
       F. Krausz, Attosecond control and measurement: lightwave elec-
       tronics, Science **317**, 769 (2007).

[20] A. L. Cavalieri, N. Müller, T. Uphues, V. S. Yakovlev, A. Baltuška, B. Horvath, B. Schmidt, L. Blümel, R. Holzwarth, S. Hendel, et al., Attosecond spectroscopy in condensed matter, Nature **449**, 1029 (2007).

[21] I. Znakovskaya, P. von den Hoff, S. Zherebtsov, A. Wirth, O. Herrwerth, M. J. J. Vrakking, R. de Vivie-Riedle, and M. F. Kling, Attosecond control of electron dynamics in carbon monoxide, Phys. Rev. Lett. **103**, 103002 (2009).

[22] M. Schultze, M. Fieß, N. Karpowicz, J. Gagnon, M. Korbman, M. Hofstetter, S. Neppl, A. L. Cavalieri, Y. Komninos, T. Mercouris, et al., Delay in photoemission, Science **328**, 1658 (2010).

[23] K. Klünder, J. M. Dahlström, M. Gisselbrecht, T. Fordell, M. Swoboda, D. Guénot, P. Johnsson, J. Caillat, J. Mauritsson, A. Maquet, et al., Probing single-photon ionization on the attosecond time scale, Phys. Rev. Lett. **106**, 143002 (2011).

[24] M. Sabbar, S. Heuser, R. Boge, M. Lucchini, T. Carette, E. Lindroth, L. Gallmann, C. Cirelli, and U. Keller, Resonance effects in photoemission time delays, Phys. Rev. Lett. **115**, 133001 (2015).

[25] M. Huppert, I. Jordan, D. Baykusheva, A. von Conta, and H. J. Wörner, Attosecond delays in molecular photoionization, Phys. Rev. Lett. **117**, 093001 (2016).

[26] M. Ossiander, J. Riemensberger, S. Neppl, M. Mittermair, M. Schäffer, A. Duensing, M. S. Wagner, R. Heider, M. Wurzer, M. Gerl, et al., Absolute timing of the photoelectric effect, Nature **561**, 374 (2018).

[27] A. Kaldun, A. Blättermann, V. Stooß, S. Donsa, H. Wei, R. Pazourek, S. Nagele, C. Ott, C. D. Lin, J. Burgdörfer, et al., Observing the ultrafast buildup of a Fano resonance in the time domain, Science **354**, 738 (2016).

[28] Z.-H. Loh, M. Khalil, R. E. Correa, R. Santra, C. Buth, and S. R. Leone, Quantum state-resolved probing of strong-field-ionized xenon atoms using femtosecond high-order harmonic transient absorption spectroscopy, Phys. Rev. Lett. **98**, 143601 (2007).

[29] Z.-H. Loh, C. H. Greene, and L. S. R., Femtosecond induced trans-
      parency and absorption in the extreme ultraviolet by coherent cou-
      pling of the He 2s2p (^{1}P^o) and 2p^2 (^{1}S^e) double excitation states
      with 800 nm light, Chem. Phys. **350**, 7 (2008).

[30] E. Goulielmakis, Z.-H. Loh, A. Wirth, R. Santra, N. Rohringer, V. S.
      Yakovlev, S. Zherebtsov, T. Pfeifer, A. M. Azzeer, M. F. Kling, et al.,
      Real-time observation of valence electron motion, Nature **466**, 739
      (2010).

[31] A. R. Beck, D. M. Neumark, and S. R. Leone, Probing ultrafast
      dynamics with attosecond transient absorption, Chem. Phys. Lett.
      624, 119 (2015).

[32] M. Wu, S. Chen, S. Camp, K. J. Schafer, and M. B. Gaarde, Theory
      of strong-field attosecond transient absorption, J. Phys. B **49**, 062003
      (2016).

[33] H. Wang, M. Chini, S. Chen, C.-H. Zhang, F. He, Y. Cheng, Y. Wu,
      U. Thumm, and Z. Chang, Attosecond time-resolved autoionization
      of argon, Phys. Rev. Lett. **105**, 143002 (2010).

[34] W. Cao, E. R. Warrick, D. M. Neumark, and S. R. Leone, Attosecond
      transient absorption of argon atoms in the vacuum ultraviolet region:
      line energy shifts versus coherent population transfer, New Journal
      of Physics **18**, 013041 (2016).

[35] A. Kaldun, C. Ott, A. Blättermann, M. Laux, K. Meyer, T. Ding,
      A. Fischer, and T. Pfeifer, Extracting phase and amplitude modifica-
      tions of laser-coupled Fano resonances, Phys. Rev. Lett. **112**, 103001
      (2014).

[36] C. L. M. Petersson, L. Argenti, and F. Martín, Attosecond tran-
      sient absorption spectroscopy of helium above the $n = 2$ ionization
      threshold, Phys. Rev. A **96**, 013403 (2017).

[37] V. Stooß, S. M. Cavaletto, S. Donsa, A. Blättermann, P. Birk, C. H.
      Keitel, I. Březinová, J. Burgdörfer, C. Ott, and T. Pfeifer, Real-time
      reconstruction of the strong-field-driven dipole response, Phys. Rev.
      Lett. **121**, 173005 (2018).

[38] M. Holler, F. Schapper, L. Gallmann, and U. Keller, Attosecond
      electron wave-packet interference observed by transient absorption,
      Phys. Rev. Lett. **106**, 123601 (2011).

[39] C. Ott, A. Kaldun, L. Argenti, P. Raith, K. Meyer, M. Laux, Y. Zhang, A. Blättermann, S. Hagstotz, T. Ding, et al., Reconstruction and control of a time-dependent two-electron wave packet, Nature **516**, 374 (2014).

[40] S. Pabst, A. Sytcheva, A. Moulet, A. Wirth, E. Goulielmakis, and R. Santra, Theory of attosecond transient-absorption spectroscopy of krypton for overlapping pump and probe pulses, Phys. Rev. A **86**, 063411 (2012).

[41] Y. Kobayashi, H. Timmers, M. Sabbar, S. R. Leone, and D. M. Neumark, Attosecond transient-absorption dynamics of xenon core-excited states in a strong driving field, Phys. Rev. A **95**, 031401 (2017).

[42] M. Sabbar, H. Timmers, Y.-J. Chen, A. K. Pymer, Z.-H. Loh, S. Sayres, S. Pabst, R. Santra, and S. R. Leone, State-resolved attosecond reversible and irreversible dynamics in strong optical fields, Nature Physics **13**, 472 (2017).

[43] A. Chew, N. Douguet, C. Cariker, J. Li, E. Lindroth, X. Ren, Y. Yin, L. Argenti, W. T. Hill, and Z. Chang, Attosecond transient absorption spectrum of argon at the $L_{2,3}$ edge, Phys. Rev. A **97**, 031407 (2018).

[44] K. Hütten, M. Mittermair, S. O. Stock, R. Beerwerth, V. Shirvanyan, J. Riemensberger, A. Duensing, R. Heider, M. S. Wagner, A. Guggenmos, et al., Ultrafast quantum control of ionization dynamics in krypton, Nature Communications **9**, 719 (2018).

[45] Z. Liu, S. M. Cavaletto, C. Ott, K. Meyer, Y. Mi, Z. Harman, C. H. Keitel, and T. Pfeifer, Phase reconstruction of strong-field excited systems by transient-absorption spectroscopy, Phys. Rev. Lett. **115**, 033003 (2015).

[46] Z. Liu, Q. Wang, J. Ding, S. M. Cavaletto, T. Pfeifer, and B. Hu, Observation and quantification of the quantum dynamics of a strong-field excited multi-level system, Scientific Reports **7**, 39993 (2017).

[47] V. Becquet and S. M. Cavaletto, Transient-absorption phases with strong probe and pump pulses, J. Phys. B **51**, 035501 (2018).

[48] Y. Cheng, M. Chini, X. Wang, A. González-Castrillo, A. Palacios, L. Argenti, F. Martín, and Z. Chang, Reconstruction of an excited-state molecular wave packet with attosecond transient absorption spectroscopy, Phys. Rev. A **94**, 023403 (2016).

[49] E. R. Warrick, W. Cao, D. M. Neumark, and S. R. Leone, Probing the dynamics of Rydberg and valence states of molecular nitrogen with attosecond transient absorption spectroscopy, J. Phys. Chem. A **120**, 3165 (2016).

[50] E. R. Warrick, J. E. Bækhøj, W. Cao, A. P. Fidler, F. Jensen, L. B. Madsen, S. R. Leone, and D. M. Neumark, Attosecond transient absorption spectroscopy of molecular nitrogen: Vibrational coherences in the $b'\ ^1\Sigma_u^+$ state, Chem. Phys. Lett. **683**, 408 (2017).

[51] C.-T. Liao, X. Li, D. J. Haxton, T. N. Rescigno, R. R. Lucchese, C. W. McCurdy, and A. Sandhu, Probing autoionizing states of molecular oxygen with XUV transient absorption: Electronic-symmetry-dependent line shapes and laser-induced modifications, Phys. Rev. A **95**, 043427 (2017).

[52] J. E. Bækhøj, L. Yue, and L. B. Madsen, Nuclear-motion effects in attosecond transient-absorption spectroscopy of molecules, Phys. Rev. A **91**, 043408 (2015).

[53] M. Reduzzi, W.-C. Chu, C. Feng, A. Dubrouil, J. Hummert, F. Calegari, F. Frassetto, L. Poletto, O. Kornilov, M. Nisoli, et al., Observation of autoionization dynamics and sub-cycle quantum beating in electronic molecular wave packets, J. Phys. B **49**, 065102 (2016).

[54] J. E. Bækhøj, C. Lévêque, and L. B. Madsen, Signatures of a conical intersection in attosecond transient absorption spectroscopy, Phys. Rev. Lett. **121**, 023203 (2018).

[55] M. Hollstein, R. Santra, and D. Pfannkuche, Correlation-driven charge migration following double ionization and attosecond transient absorption spectroscopy, Phys. Rev. A **95**, 053411 (2017).

[56] M. Schultze, K. Ramasesha, C. D. Pemmaraju, S. A. Sato, D. Whitmore, A. Gandman, J. S. Prell, L. J. Borja, D. Prendergast, K. Yabana, et al., Attosecond band-gap dynamics in silicon, Science **346**, 1348 (2014).

[57] L. J. Borja, M. Zürch, C. D. Pemmaraju, M. Schultze, K. Ramasesha, A. Gandman, J. S. Prell, D. Prendergast, D. M. Neumark, and S. R. Leone, Extreme ultraviolet transient absorption of solids from femtosecond to attosecond timescales, J. Opt. Soc. Am. B **33**, C57 (2016).

[58] A. Moulet, J. B. Bertrand, T. Klostermann, A. Guggenmos, N. Karpowicz, and E. Goulielmakis, Soft X-ray excitonics, Science **357**, 1134 (2017).

[59] F. Schlaepfer, M. Lucchini, S. A. Sato, M. Volkov, L. Kasmi, N. Hartmann, A. Rubio, L. Gallmann, and U. Keller, Attosecond optical-field-enhanced carrier injection into the GaAs conduction band, Nature Physics **14**, 560 (2018).

[60] M. Schultze, E. M. Bothschafter, A. Sommer, S. Holzner, W. Schweinberger, M. Fiess, M. Hofstetter, R. Kienberger, V. Apalkov, V. S. Yakovlev, et al., Controlling dielectrics with the electric field of light, Nature **493**, 75 (2013).

[61] M. Lucchini, S. A. Sato, A. Ludwig, J. Herrmann, M. Volkov, L. Kasmi, Y. Shinohara, K. Yabana, L. Gallmann, and U. Keller, Attosecond dynamical Franz-Keldysh effect in polycrystalline diamond, Science **353**, 916 (2016).

[62] C.-T. Liao, A. Sandhu, S. Camp, K. J. Schafer, and M. B. Gaarde, Beyond the single-atom response in absorption line shapes: Probing a dense, laser-dressed helium gas with attosecond pulse trains, Phys. Rev. Lett. **114**, 143002 (2015).

[63] C.-T. Liao, A. Sandhu, S. Camp, K. J. Schafer, and M. B. Gaarde, Attosecond transient absorption in dense gases: Exploring the interplay between resonant pulse propagation and laser-induced line-shape control, Phys. Rev. A **93**, 033405 (2016).

[64] S. Chen, M. Wu, M. B. Gaarde, and K. J. Schafer, Quantum interference in attosecond transient absorption of laser-dressed helium atoms, Phys. Rev. A **87**, 033408 (2013).

[65] M. Chini, X. Wang, Y. Cheng, and Z. Chang, Resonance effects and quantum beats in attosecond transient absorption of helium, J. Phys. B **47**, 124009 (2014).

[66] W. Dong, Y. Li, X. Wang, J. Yuan, and Z. Zhao, Analysis of interference in attosecond transient absorption in adiabatic condition, Phys. Rev. A **92**, 033412 (2015).

[67] M. Lindberg and S. W. Koch, Transient oscillations and dynamic Stark effect in semiconductors, Phys. Rev. B **38**, 7607 (1988).

[68] C. H. Brito-Cruz, J. P. Gordon, P. C. Becker, R. L. Fork, and C. V. Shank, Dynamics of spectral hole burning, IEEE Journal of Quantum Electronics **24**, 261 (1988).

[69] A. R. Beck, B. Bernhardt, E. R. Warrick, M. Wu, S. Chen, M. B. Gaarde, K. J. Schafer, D. M. Neumark, and S. R. Leone, Attosecond transient absorption probing of electronic superpositions of bound states in neon: detection of quantum beats, New Journal of Physics **16**, 113016 (2014).

[70] S. Chen, M. J. Bell, A. R. Beck, H. Mashiko, M. Wu, A. N. Pfeiffer, M. B. Gaarde, D. M. Neumark, S. R. Leone, and K. J. Schafer, Light-induced states in attosecond transient absorption spectra of laser-dressed helium, Phys. Rev. A **86**, 063408 (2012).

[71] J. E. Bækhøj and L. B. Madsen, Light-induced structures in attosecond transient-absorption spectroscopy of molecules, Phys. Rev. A **92**, 023407 (2015).

[72] R. Santra, V. S. Yakovlev, T. Pfeifer, and Z.-H. Loh, Theory of attosecond transient absorption spectroscopy of strong-field-generated ions, Physical Review A **83**, 033405 (2011).

[73] A. N. Pfeiffer and S. R. Leone, Transmission of an isolated attosecond pulse in a strong-field dressed atom, Phys. Rev. A **85**, 053422 (2012).

[74] S. Chen, M. Wu, M. B. Gaarde, and K. J. Schafer, Laser-imposed phase in resonant absorption of an isolated attosecond pulse, Phys. Rev. A **88**, 033409 (2013).

[75] C. Ott, A. Kaldun, P. Raith, K. Meyer, M. Laux, J. Evers, C. H. Keitel, C. H. Greene, and T. Pfeifer, Lorentz meets Fano in spectral line shapes: a universal phase and its laser control, Science **340**, 716 (2013).

[76] A. Wirth, M. T. Hassan, I. Grguraš, J. Gagnon, A. Moulet, T. T. Luu, S. Pabst, R. Santra, Z. A. Alahmed, A. M. Azzeer, et al., Synthesized light transients, Science **334**, 195 (2011).

[77] M. Chini, B. Zhao, H. Wang, Y. Cheng, S. X. Hu, and Z. Chang, Subcycle AC Stark shift of helium excited states probed with isolated attosecond pulses, Phys. Rev. Lett. **109**, 073601 (2012).

[78] S. H. Autler and C. H. Townes, Stark effect in rapidly varying fields, Phys. Rev. **100**, 703 (1955).

[79] M. Wu, S. Chen, M. B. Gaarde, and K. J. Schafer, Time-domain perspective on Autler-Townes splitting in attosecond transient absorption of laser-dressed helium atoms, Phys. Rev. A **88**, 043416 (2013).

[80] N. Harkema, J. E. Bækhøj, C.-T. Liao, M. B. Gaarde, K. J. Schafer, and A. Sandhu, Controlling attosecond transient absorption with tunable, non-commensurate light fields, Opt. Lett. **43**, 3357 (2018).

[81] J. C. Baggesen, E. Lindroth, and L. B. Madsen, Theory of attosecond absorption spectroscopy in krypton, Phys. Rev. A **85**, 013415 (2012).

[82] J. E. Bækhøj, Attosecond transient absorption spectroscopy of atoms and diatomic molecules, Ph.D. thesis, Aarhus University (2016).

[83] J. C. Baggesen and L. B. Madsen, On the dipole, velocity and acceleration forms in high-order harmonic generation from a single atom or molecule, J. Phys. B **44**, 115601 (2011).

[84] M. B. Gaarde, C. Buth, J. L. Tate, and K. J. Schafer, Transient absorption and reshaping of ultrafast XUV light by laser-dressed helium, Phys. Rev. A **83**, 013419 (2011).

[85] B. H. Bransden and C. J. Joachain, *Physics of Atoms and Molecules* (Pearson, 2003).

[86] K. Aidas, C. Angeli, K. L. Bak, V. Bakken, R. Bast, L. Boman, O. Christiansen, R. Cimiraglia, S. Coriani, P. Dahle, et al., The Dalton quantum chemistry program system, WIREs Comput. Mol. Sci. **4**, 269 (2014).

[87] M. J. Frisch, G. W. Trucks, H. B. Schlegel, G. E. Scuseria, M. A. Robb, J. R. Cheeseman, G. Scalmani, V. Barone, B. Mennucci, G. A. Petersson, et al., Gaussian 09, Revision A.02, (2016).

[88] L. B. Madsen, Gauge invariance in the interaction between atoms and few-cycle laser pulses, Phys. Rev. A **65**, 053417 (2002).

[89] L. Y. Peng, Dynamics of diatomic molecules in intense fields, Ph.D. thesis, The Queen's University Belfast (2005).

[90] M. Førre and A. S. Simonsen, Generalized velocity-gauge form of the light-matter interaction Hamiltonian beyond the dipole approximation, Phys. Rev. A **93**, 013423 (2016).

[91] L. Yue, Strong-field-induced breakup of diatomic molecules, Ph.D. thesis, Aarhus University (2016).

[92] T. Kjellsson, M. Førre, A. S. Simonsen, S. Selstø, and E. Lindroth, Alternative gauge for the description of the light-matter interaction in a relativistic framework, Phys. Rev. A **96**, 023426 (2017).

[93] J. J. Sakurai, *Modern Quantum Mechanics* (Addison-Wesley, 1994).

[94] M. D. Feit, J. A. Fleck Jr, and A. Steiger, Solution of the Schrödinger equation by a spectral method, Journal of Computational Physics **47**, 412 (1982).

[95] P. Schwendner, F. Seyl, and R. Schinke, Photodissociation of Ar2+ in strong laser fields, Chemical Physics **217**, 233 (1997).

[96] D. J. Tannor, *Introduction to Quantum Mechanics* (University Science Books, 2007).

[97] W. T. Cochran, J. W. Cooley, D. L. Favin, H. D. Helms, R. A. Kaenel, W. W. Lang, G. C. Maling, D. E. Nelson, C. M. Rader, and P. D. Welch, What is the fast fourier transform?, Proceedings of the IEEE **55**, 1664 (1967).

[98] W. T. Vetterling, S. A. Teukolsky, and W. H. Press, *Numerical recipes in FORTRAN* (Cambridge University Press, New York, NY, USA, 1992), 2nd ed.

[99] J. Muga, J. Palao, B. Navarro, and I. L. Egusquiza, Complex absorbing potentials, Phys. Rep. **395**, 357 (2004).

[100] W.-C. Chu, S.-F. Zhao, and C. D. Lin, Laser-assisted-autoionization dynamics of helium resonances with single attosecond pulses, Phys. Rev. A **84**, 033426 (2011).

[101] M. Fleischhauer, A. Imamoglu, and J. P. Marangos, Electromagnetically induced transparency: Optics in coherent media, Rev. Mod. Phys. **77**, 633 (2005).

[102] M.-F. Lin, A. N. Pfeiffer, D. M. Neumark, S. R. Leone, and O. Gessner, Strong-field induced XUV transmission and multiplet splitting in 4d-16p core-excited Xe studied by femtosecond XUV transient absorption spectroscopy, J. Chem. Phys. **137**, 244305 (2012).

[103] M. Chini, X. Wang, Y. Cheng, Y. Wu, D. Zhao, D. A. Telnov, S.-I. Chu, and Z. Chang, Sub-cycle oscillations in virtual states brought to light, Scientific Reports **3**, 1105 (2013).

[104] Y. Suxia, T. S. Marco, and T. Howe-Siang, Perturbed free induction decay in ultrafast mid-IR pump–probe spectroscopy, Chem. Phys. Lett. **517**, 36 (2011).

[105] G. W. F. Drake, *Springer handbook of Atomic, Molecular, and Optical Physics* (Springer, New York, NY, USA, 2006).

[106] D. J. Griffiths, *Introduction to Quantum Mechanics* (Prentice Hall, Upper Saddle River, NJ, 2005).

[107] W.-C. Chu and C. D. Lin, Absorption and emission of single attosecond light pulses in an autoionizing gaseous medium dressed by a time-delayed control field, Phys. Rev. A **87**, 013415 (2013).

[108] H. Paul, Interference and 'which way' information, Optical and Quantum Electronics **28**, 1111 (1996).

[109] J. E. Bækhøj and L. B. Madsen, Attosecond transient-absorption spectroscopy on aligned molecules, Phys. Rev. A **94**, 043414 (2016).

[110] B. Zhang, J. Zhao, and Z.-X. Zhao, Multi-electron effects in attosecond transient absorption of CO molecules, Chinese Physics Letters **35**, 043201 (2018).

[111] H. J. Werner and W. Meyer, MCSCF study of the avoided curve crossing of the two lowest $^1\Sigma^+$ states of LiF, J. Chem. Phys. **74**, 5802 (1981).

[112] O. Laporte and W. F. Meggers, Some rules of spectral structure, J. Opt. Soc. Am. **11**, 459 (1925).

[113] D. J. Maas, D. I. Duncan, A. F. G. van der Meer, W. J. van der Zande, and L. D. Noordam, Vibrational ladder climbing in NO by ultrashort infrared laser pulses, Chem. Phys. Lett. **270**, 45 (1997).

[114] G. Marcus, A. Zigler, and L. Friedland, Molecular vibrational ladder climbing using a sub-nanosecond chirped laser pulse, Europhys. Lett. **74**, 43 (2006).

[115] D. S. Tchitchekova, S. Chelkowski, and A. D. Bandrauk, Adiabatic climbing of vibrational ladders using Raman transitions with chirped pump lasers: effect of higher electronic surfaces and control of the shapes of vibrational wave packets, Journal of Raman Spectroscopy **38**, 927 (2007).

[116] H. Stapelfeldt and T. Seideman, Colloquium: Aligning molecules with strong laser pulses, Rev. Mod. Phys. **75**, 543 (2003).

[117] L. Holmegaard, J. H. Nielsen, I. Nevo, H. Stapelfeldt, F. Filsinger, J. Küpper, and G. Meijer, Laser-induced alignment and orientation of quantum-state-selected large molecules, Phys. Rev. Lett. **102**, 023001 (2009).

[118] S. De, I. Znakovskaya, D. Ray, F. Anis, N. G. Johnson, I. A. Bocharova, M. Magrakvelidze, B. D. Esry, C. L. Cocke, I. V. Litvinyuk, et al., Field-free orientation of CO molecules by femtosecond two-color laser fields, Phys. Rev. Lett. **103**, 153002 (2009).

[119] K. Oda, M. Hita, S. Minemoto, and H. Sakai, All-optical molecular orientation, Phys. Rev. Lett. **104**, 213901 (2010).

[120] E. Frumker, C. T. Hebeisen, N. Kajumba, J. B. Bertrand, H. J. Wörner, M. Spanner, D. M. Villeneuve, A. Naumov, and P. B. Corkum, Oriented rotational wave-packet dynamics studies via high harmonic generation, Phys. Rev. Lett. **109**, 113901 (2012).

[121] G. Arfken, *Mathematical Methods for Physicists* (Academic Press, Orlando, FL, 1985).

[122] D. W. Kammler, *A First Course in Fourier Analysis* (Cambridge University Press, Cambridge, 2007).